

國立交通大學

機械工程學系

博士論文

應用真實流向概念重建通量法則於靜直接模擬法速解尤拉方
程式的研究

**Development of Volume-to-Volume True-Direction Flux
Reconstruction Scheme in the Quiet Direct Simulation Method for
Euler Equation**

研究生：林雅茹

指導教授：吳宗信 博士

西元 2013 年七月

應用真實流向概念重建通量法則於靜直接模擬法速解尤拉方
程式的研究

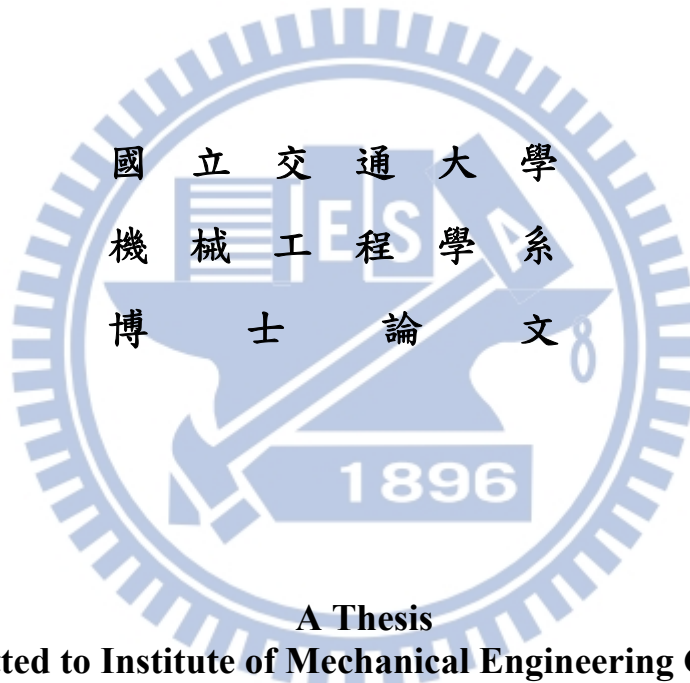
**Development of Volume-to-Volume True-Direction Flux
Reconstruction Scheme in the Quiet Direct Simulation Method for
Euler Equation**

學生：林雅茹

Student : Ya-Ju Lin

指導教授：吳宗信 博士

Advisor : Dr. Jong-Shinn Wu



**A Thesis
Submitted to Institute of Mechanical Engineering Collage of
National Chiao Tung University
In Partial Fulfillment of the Requirements
for the Degree of
Doctor of Philosophy
in
Mechanical Engineering
July 2013
Hsinchu, Taiwan**

西元 2013 年 7 月

應用真實流向概念重建通量法則於靜直接模擬法速解尤 拉方程式的研究

學生：林雅茹

指導教授：吳宗信 博士

國立交通大學
機械工程學系博士班

中文摘要

近年來一項以模擬粒子為基礎來解非黏滯尤拉方程式的數值方法稱之為靜態直接模擬法 (Quiet Direct Simulation, QDS) [Albright *et al.*, 2002]。此方法利用高司-赫麥 (Gauss-Hermite) 積分集合式來取代馬克斯威爾與波茲曼 (Maxwell-Boltzmann) 速度分佈的表示。不僅可以輕易地處理流體中急遽變化的變數分佈 (如大部分的計算流體力學一樣) 更可以準確的仿效真實流的運行方式引入真實方向的守恒場，又因為具有地域性高 (不需要大範圍考慮周遭的網格) 的特點使得平行化的計算程式得以輕易達成。由於在每個網格內都擁有相同的離散速度分佈，因此對於計算時所要求的記憶體需求可減至最低。但所謂有一利必有一弊，因而衍生出數值擴散性 (numerical diffusion) 太強等問題，驅使 Smith 等人 [Smith *et al.*, 2009] 發展出另一項以近二階 QDS 方法 (QDS-2N) 來改善相關問題以達到大幅提升數值的精確度。但是，在改善的過程中仍未真正考慮到流體真實流向的概念而有所遺憾。為解決此問題，本論文將對此數值方法提出改善方法並且用理論分析的角度進行探討。

在第一部份方面，就數值方法的觀點來說，本論文一樣是利用以近二階靜態直接模擬法來求解尤拉方程式，目的是發展一項根據流體的真實流向概念而進行的重建通量法則，我們稱之為 QDS- N^2 法。不同於傳統的有限差分法是把通量計算存取於網格間的界面，相較之下，QDS 則是根據流體的真實流向來決定該網格的通量方式，其間，實際計算通過網格的流量並有效地存取於網格內使其達到完

全遵循流體真實流向之計算法。在計算通量之前，我們會在每一個網格中引入數顆 QDS 粒子，而此粒子根據瞬間加權擁有守恒場的變數值，並包含了質量、動量與能量等計算值。甚至守恒場的變數值變化情形（可以依據多項式表示）在同一網格中皆可被允許隨空間變化。雖然在一維流場中，QDS-N² 法重建通量表示式與 QDS-2N 法重建通量表示式是一模一樣，不過在流場延伸至多維度時兩種方法卻有所不同。為了呈現兩方法的優異性，在二維流的計算中，我們經由幾項不同的算例結果來驗證此新的流量重建法的優異性，並且在第二部份理論分析方面以解析解的方式探討與 QDS-2N 方法的差異。文中我們對於二維的研究比對項目包含了震波撞擊低壓近似氣泡問題、尤拉四震波的交互作用問題、尤拉四面波交互作用問題、三馬赫波正面衝擊水平台階和水平渦流擾動問題。並且對於模擬時所耗費的計算時間與更高階計算之效果做進一步的探討。根據結果顯示，在相較於 QDS-2N 法的情況之下，本文所提出的多維度重建法則在計算的精確度上確實有很大的提升。以得到相同數值精確度的標準而言，屏除因考慮流體真實流向而增加計算量所耗費的時間外，就水平渦流擾動問題的結果來說，相較於 QDS-2N 法，QDS-N² 法在計算上所消耗的時間可以大幅減少。此外，誠如先前所提及 QDS 乃是一個高地域性的數值方法，非常有利於分散式叢集電腦上進行平行計算。因此，發展三維的 QDS 數值方法也將一併利用平行方式進行。而文中所有提及平行效率的研究與相關的平行計算，皆在台灣國家實驗研究院所屬國家高速網路與計算中心內所提供的 ALPS 叢集電腦中完成。就平行效率的研究方面，我們在計算大尺度的問題時使用高達 256 顆處理器分別完成 0.5、2、12.5 百萬的計算網格，根據 strong scaling 所得的結果顯示，得到的平行效率可達 75%、68.5%與 65.5%。另一項 weak scaling 的研究，比對理想值為 1.0 的平行效率，使用本方法所得到的效率可達 1.2，其中處理器最高達到 128 顆，而平均每一顆處理器皆包含計算 2 萬個計算網格。

在第二部份理論分析方面，我們將所有有關質量、動量與能量的通量分別對 QDS-2N 和 QDS-N² 兩種數值方法進行解析解的分析推導。比較方式是針對兩運算法在流場中因不同變數值的改變於彼此之間所產生的通量差異。結果顯示二者通量值於低密度、低溫與高速的流域範圍中較易產生較大差異，而此範圍往往也是擴散波出現的地方。除此之外，本研究觀察到當兩數值方法在處理水平和垂直軸（x 軸與 y 軸）的計算問題時彼此所產生的通量值差異甚小，反之在計算斜角

流場時會相差較大。因此，可以根據本研究結果知道在未來處理模擬流場等問題時，得以輕易地判斷合適於問題的 QDS- N^2 法或 QDS-2N 方法而有效地取得所預期的結果，高精確度以利分析或是快速地得到流場趨勢。

對於主要的研究結果與未來研究方向的建議將總結於文末。



Development of Volume-to-Volume True-Direction Flux Reconstruction Scheme in the Quiet Direct Simulation Method for Euler Equation

Student: Ya-Ju Lin

Advisor: Dr. Jong-Shinn Wu

Department of Mechanical Engineering
National Chiao Tung University

Abstract

A particle-based quiet direct simulation (QDS) method [Albright *et al.*, 2002] was invented to solve the inviscid Euler equation, in which the Maxwell-Boltzmann velocity distribution is enforced through the use of Gauss-Hermite quadrature integration without using any random number. It is a very fast Euler equation solver, which is deterministic with large dynamic range of flow properties like most conventional CFD methods, employs true-direction conservative fluxes for faithfully mimicking real flow motion, is highly localized (a small stencil) for easier parallelization and requires very low memory because the discrete velocities can be re-used in each cell. However, it is numerically very diffusive and has been extended to a nearly second-order numerical scheme by Smith *et al.* [2009] without really considering true-direction flux reconstruction. Thus, we intend to further address this problem from both numerical and theoretical viewpoints in this thesis.

In the numerical part, a true-direction flux reconstruction of the second-order quiet direct simulation (QDS) as an equivalent Euler equation solver, called QDS-N², is presented. Because of the true-directional nature of QDS, where volume-to-volume

(true direction) fluxes are computed, as opposed to fluxes at cell interfaces as employed by traditional finite volume schemes, a volumetric reconstruction is required to reach a totally true-direction scheme. The conserved quantities are permitted to vary (according to a polynomial expression) across all simulated dimensions. Prior to the flux computation, QDS particles are introduced using properties based on weighted moments taken over the polynomial reconstruction of the conserved variables such as mass, momentum and energy. The resulting flux expressions are shown to exactly reproduce the existing second-order extension for a one-dimensional flow, while providing a means for true multi-dimension reconstruction. The new reconstruction is demonstrated in several verification studies. These include several two-dimensional test cases such as shock bubble interaction problem, an Euler-four-shock interaction, Euler-four-contact interaction, Mach 3 facing over a forward step, and the advection of a vortical disturbance. These results are presented, and the increased computational time and the effect of higher-order extension are discussed. The results show that the proposed multi-dimensional reconstruction provides a significant increase in the accuracy of the solution as compared to the previously developed QDS-2N method. We show that, despite the increase in the computational expense, the computational speed of the proposed QDS- N^2 method is several times higher than that of the previously proposed QDS-2N method for a fixed degree of numerical accuracy, at least, for the test problem of the advection of vortical disturbances. As mentioned earlier, QDS method is intrinsically a highly localized numerical scheme, which makes it highly suitable for parallel computing on distributed-memory cluster machines using domain decomposition. With parallel implementation, an extension to three-dimensional QDS method is also demonstrated. The results show that the parallel efficiency, based on a strong scaling study, for a large-scale problem using 0.5, 2, and 12.5 million cells can

reach up to 75%, 68.5%, and 65.5% with 256 processors respectively. In addition, the parallel efficiency, based on a weak scaling study, for a shock bubble interaction is 1.2, which the ideal efficiency is 1.0, up to 49 processors for 20,000 cells per processor. Note all the parallel performance tests were performed at the APLS cluster of National Center for High-Performance Computing, Taiwan.

In the theoretical part, we have derived the analytical expressions of all the fluxes related to mass, momentum and energy in the two-dimensional QDS- N^2 and QDS-2N methods respectively. Comparisons are made systematically between the corresponding fluxes in the two methods by varying flow properties. Results show that a large discrepancy of fluxes between these two methods occurs in the ranges of low density, low temperature, and high velocity. It is also interesting to learn that this range of gas flow often corresponds to an expansion wave region. Moreover, the fluxes using both methods are similar horizontal and vertical directions (x and y-direction), while large discrepancy is found in the fluxes going to the diagonal direction. With this observation, we can evaluate the accuracy of QDS-2N method as compared to QDS- N^2 method in the flow field, which may be important in deciding which method to be used for different flow problems.

The major findings of the research with the recommendations for future study are summarized at the end of the thesis.

誌謝

本篇論文得以完成最要感謝的是指導教授 吳宗信老師的細心指導。感謝吳老師在論文指導時所花的時間與精力，並且感謝口試委員陳慶耀老師、林昭安老師、牛仰堯老師、黃俊誠老師與陳明志老師百忙中遠道而來並對於學生的研究成果與論文撰寫上提供許多寶貴的意見與精闢的見解，使學生獲益良多讓論文得以更加完整。在求學的過程中，感恩於老師的指導使得學生在學習上成長不少，讓學生在學術研究上更加精益求精，在研究態度上變得更加嚴謹、敏銳，並且從老師認真且專業的指導上見識到機械熱流領域是如此的深奧與廣泛。不僅如此，於生活上，在老師的啟蒙下，學生不僅對於台灣國家環境的認知更加的多元，社會脈動更加的關懷。由衷的感謝老師對於學生在研究的環境上提供國際化的思維，並且讓學生在求學的道路上有機會出國至美國、日本參加國際會議體驗國際交流所帶來的研究熱誠。

回首六年來在交大的求學歷程，特別要感謝李文樺博士、Dr. Hadley Cave 與捷燦學長在研究上耐心的指導與無私的協助使學生渡過無數學習的障礙，並感謝孟華學姐一路來的相挺與陪伴得以撐過漫長的歲月。還要感謝實驗室學長昆模、沅明、一同畢業的學弟正勤、總是默默付出的學弟古必任、瑞祥、子豪、冠榮、熱心的明忠、仁寶、芳安、聖毅、文靜的垂青、世昕、易軒、哲偉、奇融、廷浩、電漿實驗室的宜偉、至東、志華、俊平、國淳、光堯、學妹青榕，在實驗室的相處中，不論是課業、研究或生活上都得到許多扶持。

最後僅將本論文獻給我摯愛的家人及許家偉先生一直以來對我的照顧並時時刻刻的關懷、無怨尤的陪伴，因為你們殷切的期盼，讓我有上進的動力；因為你們積極的鼓勵，讓我完成困難的學業。

林雅茹

西元 2013 年七月於 Aerothermal & Plasma Physics Laboratory

Table of Contents

中文摘要	I
Abstract	IV
誌謝	VII
Table of Contents	VIII
List of Table	X
List of Figures	XI
Nomenclature	XVIII
Chapter 1 Introduction	1
1.1 Background and Motivation	1
1.1.1 Direct Simulation Monte Carlo Method	1
1.1.2 Quiet Direction Simulation Monte Carlo Method	2
1.2 Literature Survey	3
1.3 Specific Objectives of this Thesis	6
Chapter 2 Numerical Methods	8
2.1 Overview of Euler Equation Solver	8
2.1.1 Computational Fluid Dynamics	8
2.1.2 Kinetic Method	9
2.2 Quiet Direct Simulation (QDS) Method	11
2.3 QDS-2N Method	15
2.4 QDS-N ² Method	18
2.4.1 Spatial Reconstruction and Flux Calculation	18
2.4.2 One-Dimensional Flux Calculation and Implementation	21
2.4.3 Two-Dimensional Flux Calculation and Implementation	22
2.4.4 Three-Dimensional Flux Calculation and Implementation	24
2.5 Brief Summary	25
Chapter 3 Complex Gas Flow Simulations using the QDS-N² Method	27
3.1 Introduction	27
3.2 QDS Method in One-Dimension Flow	27
3.2.1 Shock Tube	27
3.2.2 Shock-blast wave interaction	28
3.2.3 Shock acoustic wave interaction	29
3.3 Shock-Bubble Interaction	30
3.3.1 Euler-Four-Shocks problem	31
3.3.2 Euler-Four-Contacts problem	32
3.3.3 Euler-Four-Contacts problem	32
3.3.4 Mach 3 Flow over a Forward Step	34

3.3.5 Shock Wave Diffraction over a 90 degree sharp corner.....	35
3.3.6 Advection of Vortical Disturbance.....	37
3.4 QDS Method in Three-Dimension Flow	39
3.4.1 Mach 2 Flow over a Pillar	40
3.5 Parallel Computing of QDS method.....	41
3.5.1 Overview of Parallel Implementation.....	41
3.5.2 Simulation Conditions	41
3.5.3 Parallel Performance.....	42
3.5.3.1 Weak Scaling.....	42
3.5.3.2 Strong Scaling.....	43
3.6 Brief Summary	44
Chapter 4 Difference Analysis of QDS-2N Method as Compared to QDS- N² Method	46
4.1 Introduction	46
4.2 Derivation of Analytical Fluxes of QDS Methods (2N vs. N ²).....	46
4.2.1 Mass Flux	46
4.2.2 Momentum Fluxes.....	48
4.2.3 Energy Flux	49
4.3 Results and Discussion	50
4.3.1 Diagrams of Relative Difference Distribution.....	50
4.3.2 Example with Large Difference	51
4.3.2.1 Shock-Bubble Interaction.....	52
4.3.2.2. Euler-Four-Shock Simulation.....	53
4.3.2.3 Mach 3 Flow over a Forward Step	54
4.3.2.4 Shock Wave Diffraction over a 90-degree Sharp Corner.....	55
4.4 Brief Summary	56
Chapter 5 Conclusion and Recommendations of Future Work	58
5.1 Summary.....	58
5.1.1 Numerical Investigation of QDS-N ² Method.....	58
5.1.2 Theoretical Analyses of Conservation Fluxes of QDS-2N Method and QDS- N ² Method.....	59
5.2 Recommendations of Future Work.....	60
References	61
Appendix A	67
List of Publications	133

List of Table

Table 2-1 The value of weight and abscissas for the Gaussian quadrature.....	69
Table 3-1 Comparison of computational expenses for QDS schemes using $2N$ and N^2 dimensional reconstruction.	70
Table 3-2 QDS scheme time cost in Euler-4-shocks interaction case.....	71
Table 3-3 pre- and post-shock fluid initial conditions.....	72
Table 3-4 Parallel Performance for a 2D shock-bubble problem with 2.4 million computational cells.	73
Table 3-5 Parallel computation times for shock-bubble problem with 500,000 cells at 2000 time steps in simulation time 0.2.....	74
Table 3-6 Parallel computation times for shock-bubble problem with 2 million cells in 2000 time steps.....	75
Table 3-7 Parallel computation times for shock-bubble problem with 12.5 million cells in 2000 time steps.	76

List of Figures

Figure 2-1. Schematic showing the way fluxes of conserved quantities between source and destination cells are calculated using the “overlap” function in QDS [Smith <i>et al.</i> , 2009].	77
Figure 2-2. Flowchart describing 2N-QDS particle computation with gradient inclusion.	78
Figure 2-3. The special reconstruction convention for current amount of conserved quantity Q in one cell.	79
Figure 2-4. QDS flux procedure within a general (arbitrary) spatial reconstruction of conserved quantity Q .	80
Figure 2-5. Flowchart describing QDS particle computation with gradient inclusion.	81
Figure 2-6. Two-dimensional motion of a single QDS particle showing “sub-particle” contributions.	82
Figure 2-7. Three-dimensional motion of a single QDS particle showing “sub-particle” contributions. The green parallelogram is presented the concept in two-dimensional.	83
Figure 3-2. The shock tube problem as computed by pre-QDS method with a uniform grid of 200 zones. The results were discussed the difference to the QDS 1 st ~3 rd method and Riemann solver using MINMOD limiter at time 0.1.	85
Figure 3-3. The interaction of two blast wave computed by the QDS method with 400 grids at $t = 0.0038$. The solid black line is WENO (fifth order) scheme with 10,000 grids.	86

Figure 3-4. Density profile of the shock-acoustic-wave case at $t = 1.8$. The solid black line is WENO-3 (fifth order) with 2000 grids compared with QDS method which without limiter form 1 st order to 3 rd order.....	87
Figure 3-5. The structure of shock bubble interaction.....	88
Figure 3-6. Zoom of shock-bubble Schlieren image with 1000×500 cells at time of 0.2. QDS 2 nd order (a) 2N method with van Leer's limiter, (b) N^2 method, and (c) 2 nd order TVD result presented in [Čada <i>et al.</i> , 2009] using the same resolution.	89
Figure 3-7. Zoom of Schlieren image of shock bubble problem at time of 0.2; (a) QDS- N^2 method with 300×100 cells; (b) QDS-2N method with 300×100 cells; (c) QDS-2N method with 450×150 cells; (d) QDS-2N scheme with 600×200 cells.....	90
Figure 3-8. The initial conditions for the first problem of Euler-4 shocks interaction...	91
Figure 3-9. Zoom of density contour line of Euler-four-shocks problem. Comparing the second-order QDS- N^2 method (a) using 100×100 grids with MC limiter and 2N method using 100×100 grids (b) and 200×200 grids (c), 300×300 grids (d) with MC limiter at time of 0.4.....	92
Figure 3-10. Zoom of the density contour lines of Euler four shocks problem. (a) the 2 nd order TVD-MUSCL method taken from Čada [Čada <i>et al.</i> , 2009] using 1000×1000 points, CFL=0.8. (b) The third-order QDS- N^2 method used 1000×1000 grids with MC limiter at time of 0.8. (c) The third-order QDS-2N method used 1000×1000 grids with MC limiter.....	93
Figure 3-11. The initial conditions for the second problem of Euler-four-shock interaction.....	94

Figure 3-12. Density profile of the four contacts problem for second-order TVD-MUSCL method taken from [Čada <i>et al.</i> , 2009].	95
Figure 3-13. Density contour obtained from QDS N^2 solver (a) and 2N solver (b) by using 1000×1000 cells, 2 nd order method with MINMOD limiter. The CFL number is 0.5. Level form 0 to 2.4 at 0.05 interval of line.	96
Figure 3-14. Density contour obtained from QDS-2N solver with 5 particles (a) and 9 particles in each direction (b); QDS- N^2 method with 5 particles (c) and 9 particles in each direction (d) by using $1,000 \times 1,000$ cells, 2 nd order method with MINMOD limiter at time of 0.8. The CFL number is 0.5. Level form 0 to 2.1 at 0.05 interval of line.	97
Figure 3-15. Density contour obtained from QDS- N^2 solver using (a) $2,000 \times 2,000$ and (b) $3,000 \times 3,000$ cells, 2 nd order method with MINMOD limiter at time of 0.8. The CFL number is 0.5. Level form 0 to 2.1 at 0.05 interval of line.	98
Figure 3-16. Geometry and boundary conditions for the Mach 3 flow over a forward facing step in a wind tunnel. All boundaries with exceptions to the inflow and outflow are secularly reflective. The outflow boundary is calculated through interpolation of states of interior cells.	99
Figure 3-17. Contour of density at 4.0s for Mach 3 flow over a foeward facing step in a wind tunnel. Compare the 2 nd order QDS-2N method (top) and QDS- N^2 method (middle) for 600×200 grids. (buttom) The result of Keats and Lien [Keats <i>et al.</i> , 2004]	100
Figure 3-18. Structure of the perturbed region behind a diffracting shock wave, defined by from Skews [1967].	101
Figure 3-19. The output for compulsory figure for shock wave diffraction (by Takayama [1991]).	102

Figure 3-20. The initial geometry of the shock wave diffraction over degree sharp corner.	103
Figure 3-21. Schematic of moving shock waves [Anderson, 1990].....	104
Figure 3-22. The density contours of the shock wave diffracting over 90 degree sharp corner with 400×400 grid, $M_s=1.5$. (a) the second-order TVD extension of Godunov method [Takayama <i>et al.</i> , 1991]. (b) the second-order QDS-2N method and (c) the second-order QDS- N^2 method with MC limiter, CFL=0.5.	105
Figure 3-23. Schlieren image of the shock wave diffracting over a 90 degree sharp corner, $M_s=1.5$. (a) the experimental result made form Ritterfeld <i>et al.</i> [Takayama <i>et al.</i> , 1991]. (b) second-order QDS-2N method and (c) QDS- N^2 method with 400×400 cells, MC limiter, CFL=0.5.....	106
Figure 3-24. Vorticity magnitude contours compared (a) exact solution and two result using 2 nd order (b) QDS 2N method and (c) QDS N^2 in 800×800 uniform cells. All results are taken the CFL number to 0.1.....	107
Figure 3-25. The vorticity profiles along the central line passing through the vortex. The comparison contained the exact solution (blue squeal-symbol line), the QDS- N^2 method using 160×160 cells (red line), 800×800 cells (black dash-dot line), and 2N method using 800×800 cells (purple long-dash line), 1600×1600 cells (green doted line). Two method s are computed in MC limiter and CFL=0.1 at time 8.0.	108
Figure 3-26. The three-dimensional geometry of the Mach 2 flow over a pillar.	109
Figure 3-27. The Density contour of the Mach 2 flow over a pillar obtained using the second-order QDS- N^2 method (a) in two-dimension with 200×200 cells; (b)	

in three-dimension with $200 \times 200 \times 100$ cells. The CFL factor is 0.5 using MINMOD limiter.	110
Figure 3-28. The three-dimensional geometry of the Mach 2 flow over a square block.	111
Figure 3-29. The Density contour of the Mach 2 flow over a square block obtained using the second-order QDS- N^2 method with $200 \times 200 \times 100$ cells (a) in x- y surface; (b) in x-z surface. The CFL factor is 0.5 using MINMOD limiter.	112
Figure 3-30. Parallel Performance of a 2D shock-bubble interaction with 2.4 million computational Cells.	113
Figure 3-31. Strong scaling performance in the QDS- N^2 method with 500,000 cells on various massively parallel systems.	114
Figure 3-32. Strong scaling performance in the QDS- N^2 method with 2 million cells on various massively parallel systems.	115
Figure 3-33. Strong scaling performance in the QDS- N^2 method with 12.5 million cells on various massively parallel systems.	116
Figure 4-1 The value of mass flux for the difference of $2N$ and N^2 method. (a) The case 1 with the gradient $1.0e^{-5}$; (b) case 2 with the gradient $1.0e^{-6}$	117
Figure 4-2. The value of momentum flux in x-direction for the difference of $2N$ and N^2 method. (a) The case 1 with the gradient $1.0e^{-5}$; (b) case 2 with the gradient $1.0e^{-6}$	118
Figure 4-3. The value of momentum flux in y-direction for the difference of $2N$ and N^2 method. (a) The case 1 with the gradient $1.0e^{-5}$; (b) case 2 with the gradient $1.0e^{-6}$	119

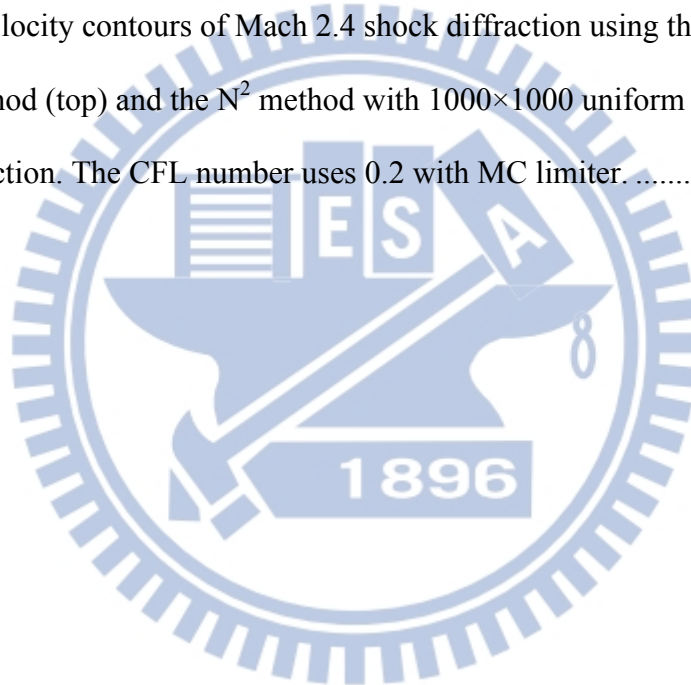
Figure 4-4. The value of energy flux for the difference of 2N and N^2 method. (a) The case 1 with the gradient $1.0e^{-5}$; (b) case 2 with the gradient $1.0e^{-6}$	120
Figure 4-5. The value of energy flux for the difference of 2N and N^2 method at the low density range. (a) The case 1 with the gradient $1.0e^{-5}$; (b) case 2 with the gradient $1.0e^{-6}$	121
Figure 4-6. Contour profile of Shock-bubble interaction. QDS- N^2 2 nd order method using 1700×500 cells with MC limiter at time of 0.2. (a) Density, (b) temperature, (c) velocity in x-direction and (d) velocity in y-direction.	122
Figure 4-7 Shock-bubble Schlieren image with 1700×500 cells at time of 0.2. QDS 2 nd order (a) 2N scheme with van Leer's limiter, (b) N^2 scheme.	123
Figure 4-8. The density contour obtained using (a) the 2N method; (b) the N^2 method with MC limiter, CFL=0.5, 1700×500 cells.	124
Figure 4-9. The temperature contour obtained using (a) the 2N method; (b) the N^2 method with MC limiter, CFL=0.5, 1700×500 cells.	125
Figure 4-10. contour profile of N^2 method. (a) Density, (b) temperature, (c) velocity in x-direction and (d) velocity in y-direction.	126
Figure 4-11. Contour of density at 4.0s for Mach 3 flow over a foeward facing step in a wind tunnel. Compare the 2 nd order QDS-2N method (top) and QDS- N^2 method (middle) for 600×200 grids. (buttom) The result of Keats and Lien [Keats <i>et al.</i> , 2004]	127
Figure 4-12. Contour of temperature obtained using second-order QDS-2N (top) and QDS- N^2 method using 4 simulation particles for Mach 3 flow over a forward facing step in a wind tunnel.	128
Figure 4-13. Schlieren image of the shock wave diffracting over a 90 degree sharp corner, $M_s=2.4$. (a) The experimental result made form Ritzerfeld <i>et al.</i>	

[Dyke, 1997]. (b) the second-order QDS-2N method, and (c) QDS-N2 method with 1000×1000 cells, MC limiter, CFL=0.2 129

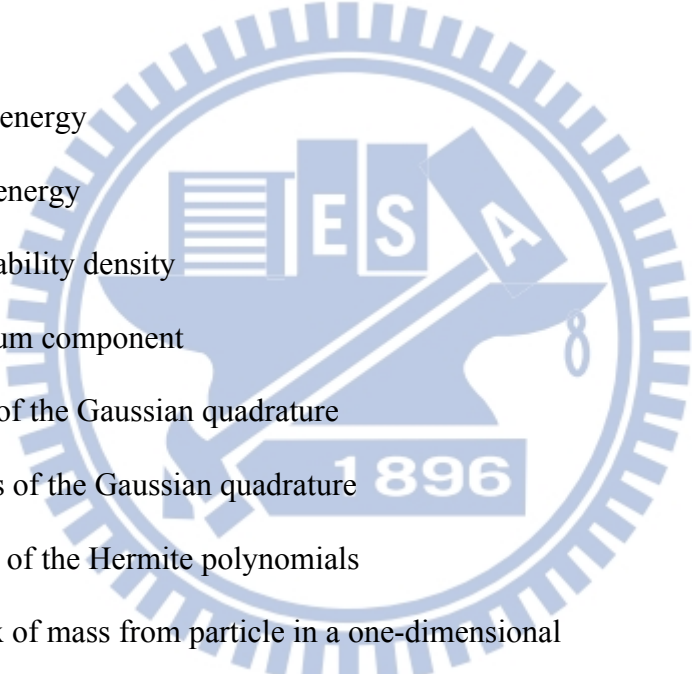
Figure 4-14. Density contours of Mach 2.4 shock diffraction using the second-order 2N method (top) and the N^2 method with 1000×1000 uniform grids. The CFL number uses 0.2 with MC limiter. 130

Figure 4-15. Temperature contours of Mach 2.4 shock diffraction using the second-order 2N method (top) and the N^2 method with 1000×1000 uniform grids. The CFL number uses 0.2 with MC limiter..... 131

Figure 4-16. Velocity contours of Mach 2.4 shock diffraction using the second-order 2N method (top) and the N^2 method with 1000×1000 uniform grids in x-direction. The CFL number uses 0.2 with MC limiter. 132



Nomenclature



N	the number of terms
V	the cell volume
ρ	the density,
u	the bulk (or mean) flow velocity
v	the velocity in y-direction
T	temperature
p	pressure
E	the total energy
e	internal energy
$p(x)$	the probability density
\dot{p}	momentum component
w	weights of the Gaussian quadrature
q	abscissas of the Gaussian quadrature
H	the roots of the Hermite polynomials
F_{MASS}	total flux of mass from particle in a one-dimensional
F_{MOM}	total flux of momentum from particle in a one-dimensional
F_{ENG}	total flux of energy from particle in a one-dimensional
Δt	the simulation time step
Δx	the cell size in x direction
Δy	the cell size in y direction
m_J	the particle mass
v_J	the particle velocity
\mathcal{E}_J	the particle internal energy

σ	$= (RT)^{1/2}$ in a given source cell.
ξ	The total number of degrees of freedom $\xi = 2(\gamma - 1)^{-1}$
Ω	the number of simulated degrees of freedom
Δx_L	the location in the cell from where the flow properties are taken
N_x	the total flux in x-direction for QDS-2N method
N_y	the total flux in y-direction for QDS-2N method
A	the overlap area
m_{flux}	mass fluxes contributed to the destination cell and subtracted from the source cell
E_{flux}	energy fluxes contributed to the destination cell and subtracted from the source cell
$p_{x,flux}$	momentum fluxes contributed to the destination cell and subtracted from the source cell in x-direction
$p_{y,flux}$	momentum fluxes contributed to the destination cell and subtracted from the source cell in y-direction
A_S	the source cell area
$q_{j(max)}$	the maximum value of the particle abscissas
Q	the value of a conserved property
X	the boundary in the x -direction
Y	the boundary in the y -direction
Z	the boundary in the y -direction
\bar{Q}	the average value of Q
ϕ	the equivalent flux limiter
F	the phase space velocity distribution function
θ	the ratio of the first order gradient

M	The net of mass fluxes for analytical equation
m'	the value of mass with 2 nd order method
P'	the value of momentum with 2 nd order method
E'	the value of energy with 2 nd order method
m	the total mass, momentum and energy at the source cell
P	the total momentum at the source cell
Δ	the difference of the value
β	the constant value $\beta = \frac{m}{2kT}$
r	position
m_o	the mass of the molecular
n_o	the number of molecular per unit configuration-space volume

Superscripts

J the index for particle

Subscripts

k the index for particle in the y -direction

J the index for particle in the x -direction

i the cell position

x the element in x -direction

y the element in y -direction

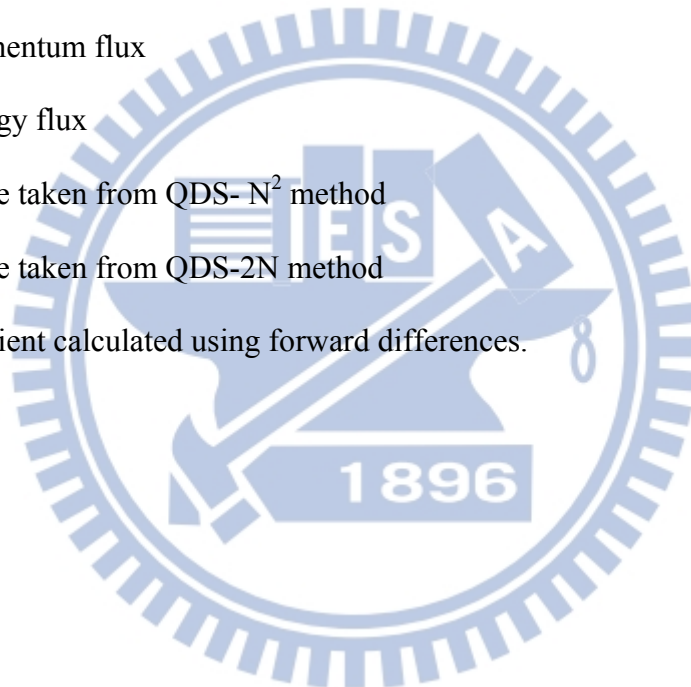
z the element in z -direction

L left hand side

R right hand side

B bottomside

T	top side
I	inlet
O	outlet
c	the value of Q at the cell centre the value of Q
s	the existing average value of the source cell
tr	The flux out value of average conserved quantity successfully moving from the source cell into the destination cell (denoted by \overline{Q}_{tr})
1	the mass flux
2	the momentum flux
3	the energy flux
N^2	the value taken from QDS- N^2 method
$2N$	the value taken from QDS-2N method
F	the gradient calculated using forward differences.



Chapter 1 Introduction

1.1 Background and Motivation

There are a number of approaches for the simulation of gas flows, depending on the nature and level of rarefaction of the flow. Computational fluid dynamics (CFD) typically uses the finite volume method to solve a set of discretized governing equations, usually the Euler or Navier-Stokes equations. Contemporary finite-volume CFD divides the computational domain into a grid of cells, and fluxes of mass, momentum, and energy are calculated through the interfaces between these cells. This technique suffers from the major disadvantage that the poor alignment of the grid with the flow field may result in large errors for some important flows (e.g., explosive blast wave), since fluxes can only occur between elements that share an interface, i.e., no reflection of the true-direction nature of the gas flow. Thus, CFD requires a careful grid design to ensure accurate results, convergence, and stability.

1.1.1 Direct Simulation Monte Carlo Method

The direct simulation Monte Carlo (DSMC) method has become the gold standard for stochastic flow field simulation. Arguably, this method has been the most successful for simulating rarefied gas flows since its development by Bird in the 1960s [Bird, 1994]. In the DSMC method the ballistic motion of the particles and their collisions are decoupled by moving the particles over a time step that is smaller than their mean collision time, indexing the particles to within a grid having dimensions that are smaller than the mean free path and then choosing collision partners from within this grid.

The DSMC algorithm requires the use of random numbers and is thus subject to statistical scatter and requires averaging over a large number of time steps to reduce the scatter in the sampled macroscopic properties. However the fluxes of properties in DSMC are “true-direction” since a particle can carry its mass, momentum, and energy between any two points in the flow field, not just between elements that share an interface. Furthermore, DSMC handles non-equilibrium effects by stochastically performing collisions between selected collision pairs, thus allowing gradual and selective transfer of momentum and energy.

In the high collision rate limit of DSMC, the particle velocity distributions approach that of the Maxwell-Boltzmann equilibrium distribution and moments of the Boltzmann equation reduce to the Euler equations [Gombosi, 1994].

1.1.2 Quiet Direction Simulation Monte Carlo Method

Albright *et al.* [2002] developed the quiet direction simulation Monte Carlo (QDSMC), a method for modeling plasmas. They subsequently applied this method to the simulation of Eulerian fluids for Sod’s one-dimensional shock tube problem and a simple two-dimensional blast wave problem. Since then little further work has been done, the only example being by Peter [Gombosi, 1994] who applied a random time step to the movement of simulation particles for simulating a typical diffusion equation. Unlike the DSMC method, there is no random number (or Monte Carlo) component to the algorithm. In the QDSMC method, the effect of sampling using random numbers is replaced by using the weights and abscissas of a Gauss–Hermite quadrature. Thus, it is valid only when thermal equilibrium can be assumed. Moreover, this method is a particle-based Euler solver that exhibits negligible statistical scatter and has a large dynamic range.

1.2 Literature Survey

Bird [Bird, 1994] showed that the DSMC method essentially provides a statistical solution to the Boltzmann equation, and Wagner [Wagner, 1992] proved mathematically that DSMC provides a solution to the Boltzmann equation as the number of simulated particles approaches the number in the actual system. This method was used to model the relaxation of a non-equilibrium gas towards the equilibrium distribution [Bird, 1963] and since that time it has been used in a wide array of applications including CVD reactor modeling [Coronell *et al.*, 1992], hypersonic flight simulations [LeBeau *et al.*, 2001], supersonic jet studies [Boyd *et al.*, 1994; Teshima *et al.*, 2001], microfluidic simulations [Karniadakis, 2002], and modeling of molecular pumps [Kwon *et al.*, 2006]. The method has grown increasingly sophisticated and powerful as improved algorithms, intermolecular collision models, gas-phase chemistry and boundary conditions have been developed and implemented.

Since the development of DSMC by Bird to solve the Boltzmann equation statistically, a large number of continuum kinetic theory based-schemes have emerged that follow a similar path. In 1980, Pullin proposed the equilibrium flux method (EFM) as an analytical equivalent to the equilibrium particle simulation method (EPSM), which is a direct simulation method where particles are forced to assume the Maxwell-Boltzmann equilibrium velocity probability distribution function instead of performing collisions [Pullin, 1980]. Later, Smith *et al.* [Smith *et al.*, 2008] proposed a general form of the EFM method known as the true direction equilibrium flux method (TDEFM), which more accurately captures the transport mechanism employed by EPSM. Fluxes calculated by TDEFM represent the true analytical solution to the molecular free flight problem, under the assumption of thermal equilibrium and uniformly distributed quantities. The calculated fluxes are valid for any size time step,

and the algorithm is unconditionally stable, although the kinetic Courant-Friedrich-Levy (CFL) number should be kept below unity to ensure physical correctness. The primary disadvantage to TDEFM is the large computational cost associated with the evaluation of the numerous exponential and error function evaluations.

As mentioned previously, Albright *et al.* [2002] developed the QDSMC method, a numerical scheme for the solution of the Euler equations. They subsequently applied QDSMC to the simulation of Eulerian fluids for problems like shock tube flow and blast wave propagation. In this method, the integrals encountered in the TDEFM formulation are replaced by approximations using Gaussian numerical integration, effectively replacing the continuous velocity distribution function with a series of discrete velocities. The method was later renamed the quiet direct simulation (QDS) method due to the lack of stochastic processes and was extended to second order spatial accuracy. The lack of complex mathematical functions results in a computationally very efficient scheme with considerably higher performance than EFM while maintaining the advantages of true directional fluxes like TDEFM.

Due to the assumption of unrestricted motion during free flight, each of the above-mentioned kinetic solvers has a large amount of (cell-size-based) numerical diffusion. To combat this dissipation, a common strategy, employed in more conventional finite volume methods, is to apply higher-order reconstruction of properties or fluxes. Macrossan [Macrossan, 1989] applied EFM using higher order spatial extensions, while Smith [Smith, 2008] attempted the analytical inclusion of gradients into true-direction volume-to-volume fluxes, only to find that the complete analytical inclusion of gradient terms in the TDEFM flux expressions is impossible. Smith *et al.* [Smith *et al.*, 2009] reduced the numerical diffusion by applying “simplified” flux reconstruction at the

interface. This method, known as QDS-2N, improves the original QDS to be almost second order in spatial accuracy.

The particle-based QDS-2N method is easily extended to multi-dimensions and multi-species. It is computationally inexpensive, easily implemented on parallel computers and, since it is a particle-based method, and does not require direction decoupling. The major disadvantage is that the scheme is inherently very diffusive. The particle-based Euler solver has two advantages. First, hybridization between the solver and a pure DSMC solver which is capable of simulating the non-continuum regions of flow is relatively simple. Several authors, including Macrossan [Macrossan, 2001], Chen [Chen, 2003], Smith [Smith, 2003] and Wu [2003], have developed such particle-based hybrid methods. The second major advantage is that particle-based methods can exchange fluxes between any two cells on the grid for any given time step. Direction decoupled CFD methods only allow fluxes to be exchanged between cells sharing a common interface. This physically unrealistic situation results in non-physical results in CFD simulations [Smith *et al.*, 2008; Cook, 1998].

The second-order QDS-2N method was applied by Cave [Lim *et al.*, 2010; Cave, *et al.*, 2010] to simulate highly unsteady low pressure flows encountered in a pulsed pressure chemical vapour deposition (PP-CVD) reactor.

1.3 Specific Objectives of this Thesis

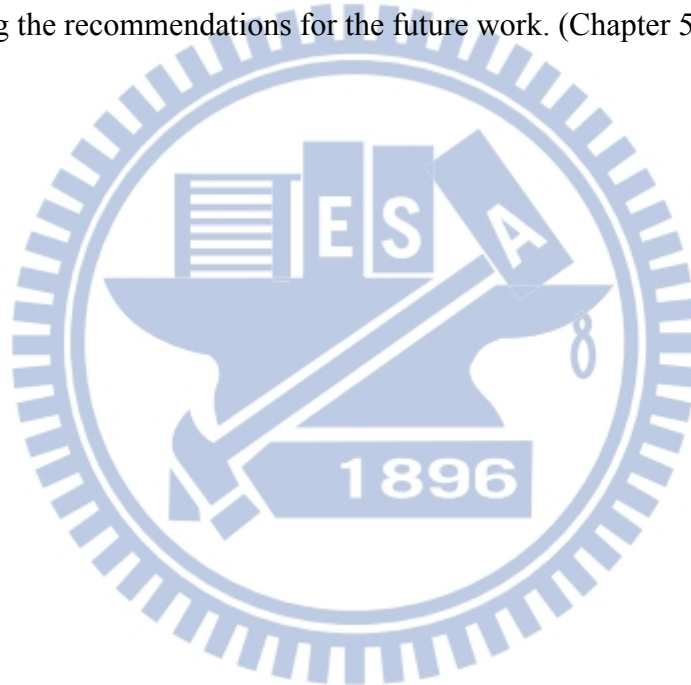
Based on the preceding discussion of studies related to the QDS-2N method, it is clear that further numerical study is needed to improve the accuracy of the QDS-2N method and, consequently, lead to more effective applications.

In this thesis, we extend the second-order QDS algorithm (QDS-2N) [Smith *et al.*, 2009] to flux reconstruction through true-direction polynomial multi-dimensional reconstruction of conserved properties across each cell width; this method is called QDS-N².

The specific objectives and organization of this thesis can be summarized as follows:

1. To improve the QDS-2N method by first studying its advantages and disadvantages. Flux reconstruction calculated using QDS-2N neglects neighbourhood cells when calculating diagonally cells. (Chapter 2)
2. To develop a QDS-N² method for solving Euler's equation for inviscid fluid flow. The fluxes of conserved properties are calculated by a sum of weighted moments over the polynomial spatial reconstruction of mass, momentum, and energy across the cell width. The particle properties are updated, considering the average value of the conserved quantity between the region bounds, which are required in translational directions and the application of splitting. (Chapter 2)
3. To develop the QDS-N² method in three-dimensions. (Chapter 2)
4. To apply the QDS-N² method to a numerical problem and an experimental case. Various numerical methods, including Riemann solvers and total variation diminishing (TVD) methods, were compared as a benchmark. (Chapter 3)
5. To apply the QDS-N² method in the three-dimensional flow. (Chapter 3)

6. To develop the parallel QDS- N^2 method for large-scale applications such that the computational time problem is reduced efficiently. The scheme includes weak scaling and strong scaling. (Chapter 3)
7. To analyze differences associated with the QDS- $2N$ method and compare QDS- $2N$ to QDS- N^2 . This involves measurements to reveal differences between the two methods and provides information to determine which problem will be considered first. (Chapter 4)
8. The concluded by summarizing the major findings found in this thesis and outlining the recommendations for the future work. (Chapter 5)



Chapter 2

Numerical Methods

2.1 Overview of Euler Equation Solver

The Euler equations describe how the density, velocity, and pressure of a moving fluid are related. The Euler equations directly represent conservation of mass, momentum, and energy, and correspond to the Navier-Stokes equations without viscosity and heat conduction terms. Eq. (1) shows a two-dimensional formulation of the Euler equations.

$$\begin{aligned} \text{Continuity: } & \frac{\partial \rho}{\partial t} + \frac{\partial(\rho u)}{\partial x} + \frac{\partial(\rho v)}{\partial y} = 0 \\ \text{X-momentum: } & \frac{\partial \rho u}{\partial t} + \frac{\partial(\rho u^2)}{\partial x} + \frac{\partial(\rho uv)}{\partial y} = -\frac{\partial P}{\partial x} \\ \text{Y-momentum: } & \frac{\partial \rho v}{\partial t} + \frac{\partial(\rho uv)}{\partial x} + \frac{\partial(\rho v^2)}{\partial y} = -\frac{\partial P}{\partial y} \end{aligned} \quad (1)$$

Although the continuity and momentum equations have been derived in the past, the energy equation has been included in the Euler equations in fluid dynamics literature [Anderson, 1995].

2.1.1 Computational Fluid Dynamics

Engineers made further approximations and simplifications to the equation set until they had a group of equations that they could solve. Recently, high speed computers have been used to solve approximations to the equations using a variety of techniques,

such as finite difference, finite volume, finite element, and spectral methods. This area of study is called CFD.

The Euler equation for the conservation of continuity, momentum and energy equation is:

$$\frac{\partial}{\partial t} \begin{pmatrix} \rho \\ \rho u \\ \rho v \\ \rho E \end{pmatrix} + \frac{\partial}{\partial x} \begin{pmatrix} \rho u \\ \rho u^2 + P \\ \rho uv \\ \rho u(E + p/\rho) \end{pmatrix} + \frac{\partial}{\partial y} \begin{pmatrix} \rho v \\ \rho uv \\ \rho v^2 + P \\ \rho v(E + p/\rho) \end{pmatrix} = 0 \quad (2)$$

where $E = e + \frac{1}{2}(u^2 + v^2)$ is the total energy and e is internal energy $e=e(T)$. For a perfect gas, internal energy is only dependent on temperature. Pressure is presented by $p = (\gamma - 1)\rho e$ with $\gamma = c_p/c_v$ the ratio of specific heats ($\gamma = 7/5$ for air).

Most numerical schemes for solving Euler equations are built around the Riemann solver. For example, Godunov technique provided two and three dimension applications in new finite volume numerical schemes and total variation diminishing (TVD) properties [Toro, 2009; LeVeque, 2004], and achieved second-order accuracy. Although, such numerical methods were generally accurate, they incurred high computational costs. However, approximate numerical schemes that reduce computational costs are not only less accurate and less robust but are also based on solutions of a Riemann problem. More extensive introductions to numerical method for the Euler equations were given by Godlewski and Raviart [1996], Kroner [1997], Laney [1998], Majda [1984], Toro [1997], Smoller [1983], and Hirsch [1990].

2.1.2 Kinetic Method

The classical kinetic theory of gas emerged from a combination of mechanics and statistics. The motions of molecules are described by probability rather than their individual orbits. This kinetic theory of gases has led to important descriptions of 1)

pressure, temperature, and a generalized equation of state for gases, and 2) transport properties (velocity, thermal conductivity, diffusion coefficients) based on first principles.

The kinetic method can be introduced by the Boltzmann equation, which is used in the study of a collection of particles in non-equilibrium statistical mechanics. The Boltzmann equation was devised by Ludwig Boltzmann in 1872 [Lerner *et al.*, 1991]. The equation is a phase space of system that contains seven variables: three coordinates for position coordinates x, y, z , where each coordinate is parameterized by time t and three for each momentum component $\dot{p}_x, \dot{p}_y, \dot{p}_z$ and each coordinate is parameterized by time t . The volume element for position r and momenta \dot{p} can be expressed as follows:

$$d^3r d^3\dot{p} = dx dy dz d\dot{p}_x d\dot{p}_y d\dot{p}_z \quad (3)$$

For one chemical species, the Boltzmann equation can be written as follows:

$$\frac{\partial F}{\partial t} + v_i \frac{\partial F}{\partial x_i} + a_i \frac{\partial F}{\partial v_i} = \left(\frac{\delta F}{\delta t} \right)_{coll} \quad (4)$$

where F is the phase space velocity distribution function which is the density of particles in the $d^3r d^3\dot{p}$ phase space volume element around the phase space point (r, \dot{p}) . $\partial F / \partial t$ is the total time derivative of the phase space distribution function, and $(\delta F / \delta t)_{coll}$ = rate of change of the phase-space distribution function due to collisions.

The Euler equation can be described using by kinetic theory. Here the conservation equation of mass, momentum and energy are derived as follows:

$$\begin{aligned} \frac{\partial (m_o n_o)}{\partial t} + \nabla \cdot (m_o n_o) &= 0 \\ m_o n_o \frac{\partial u}{\partial t} + m_o n_o (u \cdot \nabla u) + \nabla p - m_o n_o a_o &= 0 \\ \frac{3}{2} \frac{\partial p}{\partial t} + \frac{3}{2} (u \cdot \nabla) p + \frac{5}{2} p (\nabla \cdot u) &= 0 \end{aligned} \quad (5)$$

where m_o is the mass of the molecular object and n_o is the number of molecule per unit configuration-space volume. Because the Euler equations are non-linear hyperbolic equations, the shock waves are generally described by these equations. Several highly successful algorithms have been developed to solve such problems [Jameson, 1986; MacCormack *et al.*, 1975; Jameson *et al.*, 1981].

In addition to the Boltzmann equation, Maxwell-Boltzmann distribution also contributed to the kinetic theory of gasses. This distribution was first carried out in 1859 and was named after James Clerk Maxwell and Ludwig Boltzmann. The distribution function can be expressed as follows:

$$f(v_x, v_y, v_z) = \left(\frac{\beta}{\pi}\right)^{3/2} e^{-\beta(v_x^2 + v_y^2 + v_z^2)} \quad (6)$$

where the constant value $\beta = \frac{m}{2kT}$

This distribution function assumes the ideal gas is isotropic and that velocity is statistically independent. This means that there is no preferred direction and the function is independent of the orientation of the coordinate system. The gas for this distribution is close to thermodynamic equilibrium. An understanding of the Maxwell-Boltzmann distribution function is essential when studying the QDS method. The detail will be discussed in the next section (subchapter 2.2).

2.2 Quiet Direct Simulation (QDS) Method [Albright *et al.*, 2002]

The normal random variable $N(0,1)$ is defined by the probability density:

$$p(x) = \frac{e^{-x^2/2}}{\sqrt{2\pi}} \quad (7)$$

by using a Gaussian quadrature approximation, the integral of Eq.(7) over its limits can be approximated by:

$$\int_{-\infty}^{\infty} \frac{e^{-x^2/2}}{\sqrt{2\pi}} f(x) dx \approx \sum_{J=1}^N w_J f(q_J) \quad (8)$$

where w_J and q_J are the weights and abscissas of the Gaussian quadrature (also known as the Gauss-Hermite parameters) shown in Table 1, and N is the number of terms. The abscissas are the roots of the Hermite polynomials, which can be defined by the recurrence equation:

$$H_{n+1}(q) = 2qH_n - 2nH_{n-1} \quad (9)$$

where $H_{-1}=0$, and $H_0=1$. The weights can be determined from:

$$w_J = \frac{2^{n-1} n! \sqrt{\pi}}{n^2 [H_{n-1}(q_J)]^2} \quad (10)$$

The moment of the form are represented as

$$\int_{-\infty}^{\infty} \frac{e^{-v^2/2}}{\sqrt{2\pi}} v^r dv \approx \sum_{J=1}^N w_J q_J^r \quad (11)$$

where $r=0,1,\dots, 2N-1$.

The particle simulation of fluid behaviour involved random variables which governed by stochastic differential equations of motion. For example, the one-dimensional Ornstein-Uhlenbeck (OU) equations describe the random dynamics of a particle of mass relaxing at a rate γ to the local fluid velocity u and temperature $kT = m\sigma_v^2$ shown as:

$$dx = v_x dt \quad (12)$$

$$dv_x = -\gamma(v_x - u) dt + \sqrt{2\gamma\sigma_v^2} dt N(0,1) \quad (13)$$

where $N(0,1)$ is random variable. When eq.(13) in the initial condition $v_x(0) = v_{x0}$, it can be solved [Gardiner, 1985] from following equation:

$$v_x(\Delta t) = u + e^{-\gamma\Delta t} (v_{x0} - u) + \sigma_v \sqrt{1 - e^{-\gamma\Delta t}} N(0,1) \quad (14)$$

In the thermalization $\gamma\Delta t \gg 1$, eq. (13) can be described as $u + \sigma_v N(0,1)$ drawn from a local Maxwellian.

As same as DSMC calculations to split particle transport and particle thermalization into two distinct operations, we presented operations by differential OU process which denoted with subscript *tr* and *th* respectively as follows:

$$\begin{pmatrix} dx \\ dv_x \end{pmatrix} = \begin{pmatrix} v_x dt \\ 0 \end{pmatrix}_{tr} = \begin{pmatrix} 0 \\ -\gamma(v_x - u)dt + \sqrt{2\gamma\sigma_v^2 dt}N(0,1) \end{pmatrix}_{th} \quad (15)$$

The transport differential operator describes particle free streaming, while thermalization operator drives particle velocities toward $u + \sigma_v N(0,1)$ without changing their positions. In the QDS algorithm, the part of *tr* preforms particle properties i.e. masses, momenta, special internal energies in each mash; The part of *th* represents each particle which is advanced to a new position. Those parts are established local thermodynamic equilibrium throughout the fluid.

The net fluxes of mass, momentum and energy of a cell are given by the sum of individual flux contributions from all the particles flowing in and out as follows:

$$\begin{aligned} F_{MASS} &= \left(\sum_{J=1}^M F_{MASS}^J \right)_{in} - \left(\sum_{J=1}^N F_{MASS}^J \right)_{out} , & F_{MOM} &= \left(\sum_{J=1}^M F_{MOM}^J \right)_{in} - \left(\sum_{J=1}^N F_{MOM}^J \right)_{out} , \\ F_{ENG} &= \left(\sum_{J=1}^M F_{ENG}^J \right)_{in} - \left(\sum_{J=1}^N F_{ENG}^J \right)_{out} \end{aligned} \quad (16)$$

where F_{MASS}^J , F_{MOM}^J and F_{ENG}^J is the individual mass flux, individual momentum and individual energy from particle J respectively, M and N is the number of inflow and outflow particles respectively into the cell under consideration. Each of the individual contribution (with first order spatial accuracy) can be described by the expressions, e.g., in one-dimensional case:

$$F_{MASS}^J = \frac{v_J \Delta t}{\Delta x} m_J \quad F_{MOM}^J = \frac{v_J \Delta t}{\Delta x} m_J v_J \quad F_{ENG}^J = \frac{v_J \Delta t}{\Delta x} m_J \left[\frac{1}{2} v_J^2 + \varepsilon_J \right] \quad (17)$$

where the particle mass m_J , particle velocity v_J , and particle internal energy ε_J are expressed as:

$$m_J = \frac{\rho \Delta x w_J}{\sqrt{\pi}} \quad v_J = u + \sqrt{2} \sigma q_J \quad \varepsilon_J = \frac{(\xi - \Omega) \sigma^2}{2} \quad (18)$$

where ρ is the density, u is the bulk (or mean) flow velocity, and $\sigma = (RT)^{1/2}$ in a given source cell. Note R is the universal gas constant, and T is the gas temperature. The total number of degrees of freedom ξ is defined as $\xi = 2(\gamma-1)^{-1}$ and Ω is the number of simulated degrees of freedom (e.g., $\Omega = 1$ for one dimensional flow). In the existing QDS-2N [Smith *et al.*, 2009], the values of ρ , u , and σ employed in QDS particle initialization are taken from reconstructions based on linear variations. Despite fluxes being true direction in nature, the reconstructions performed by previous implementations are direction decoupled – i.e. a flux is computed through the product of (separate) fluxes previously computed (for 2D flow) in the x and y directions. For the 2D case, the particle mass and velocities in Eq. (9) become:

$$m_{JK} = \frac{\rho \Delta x \Delta y w_J w_K}{\pi} \quad v_J = u_x + \sqrt{2\sigma^2} q_J \quad v_K = u_y + \sqrt{2\sigma^2} q_K \quad (19)$$

where there are $K=1, \dots, M$ particles in the y -direction and the definition of other variables are the same as those in 1D case. The internal energy remains identical to the 1-D case, allowing for a corresponding increase in Ω to account for the extra simulated dimension. The fluxes from sources cell to any arbitrary destination cell can be calculated by the particle position distributions. The fluxes of mass, momentum and energy, which are based on the proportion of the overlapped area to the area of the original cell, are given by:

$$F_{MASS} = \frac{A}{A_s} m_{JK} \quad F_{MOM-X} = \frac{A}{A_s} m_{JK} v_J \quad F_{MOM-Y} = \frac{A}{A_s} m_{JK} v_K$$

$$F_{ENG} = \frac{A}{A_s} m_{JK} \left[\frac{1}{2} (v_J^2 + v_K^2) + \epsilon_{JK} \right] \quad (20)$$

where A is the overlapped area as $u \times v \times dt^2$ and A_s is the source cell area as $dx \times dy$.

2.3 QDS-2N Method

In the QDS-2N algorithm used in the present study, the concept of QDS “particles” whose properties are interpolated onto a grid (as used by Albright *et al.* [2002] in their original development of the technique) is replaced by the concept of fluxes of a large number of particles uniformly distributed across the cell, as described by Smith *et al.* [Smith *et al.*, 2008]. In this finite volume approach, quantities such as mass, momentum and energy are exactly conserved by tracking fluxes from source volumes to destination volumes. If the particle position distributions (i.e. gradients of density in the flow) are known, the flux from the source region to any arbitrary destination volume can be calculated.

In the present implementation of QDS-2N, the flux scheme employed by Smith *et al.* [2009] is used for the efficient calculation of two dimensional, true direction fluxes. Here the N_x fluxes in each coordinate direction are computed separately requiring the calculation of $2N$ fluxes for the two-dimensional case.

In the second order scheme the gradients of cell velocity in the x -coordinate direction (du/dx), can be used to update the flux velocity:

$$v_j = u + \frac{du}{dx} \Delta x_L + \sqrt{2\sigma_v^2} q_j \quad (21)$$

where Δx_L represents the location in the cell from where the flow properties are taken. Fluxes moving to the right are assumed to take their quantities from the reconstructed state $\Delta x_L = 0.5(\Delta x - v_{xj}\Delta t)$ to the right of the cell center, where Δx is the cell size and Δt is the simulation time step. This corresponds to the displacement of the centre of mass of the flux which moves into the destination cell. Left moving fluxes have properties constructed in a similar fashion for which $\Delta x_L = 0.5(-\Delta x - v_{xj}\Delta t)$. The flux then moves in free flight, justifying the use of a linear interpolation routine.

The total mass and energy associated with the particles in the particular “bucket” for the second-order case in the x -direction can be determined from the cell’s density (ρ), energy (E) and their respective gradients by:

$$m_j = \frac{\left(\rho + \frac{d\rho}{dx} \Delta x_L\right) \Delta x w_j}{\sqrt{\pi}} \quad (22)$$

where w_j are weights of the Gauss-Hermite quadrature, and:

$$\varepsilon_j = \frac{(\xi - \Omega) \left(\sigma + \frac{d\sigma}{dx} \Delta x_L\right)^2}{2\Omega} \quad (23)$$

where $\Omega=2$ for two-dimensional simulations. Any unused translational and other non-translational degrees of freedom are thus treated as internal structural degrees of freedom.

The amount of mass which fluxes to the new cell can be determined by multiplying Eq. (22) by $v_j \Delta t / \Delta x$. The gradients used in Eq. (21) to (23) are determined using the MINMOD (Minimum Modulus) and the MC (Monotonized Central Difference) scheme [Van Leer, 1977]. Using density in the x -direction as an example, the gradient using the MC slope limiter is:

$$\frac{d\rho}{dx} = \text{MINMOD} \left[\frac{\rho_{i+1} - \rho_{i-1}}{2\Delta x}, \text{MINMOD} \left(2 \frac{\rho_{i+1} - \rho_i}{\Delta x}, 2 \frac{\rho_i - \rho_{i-1}}{\Delta x} \right) \right] \quad (24)$$

where the MINMOD scheme is:

$$\text{MINMOD}[a, b] = \begin{cases} 0 & \text{IF SIGN}(ab) < 0 \\ a & \text{IF (SIGN}(ab) > 0) \text{ AND } (|a| < |b|) \\ b & \text{IF (SIGN}(ab) > 0) \text{ AND } (|b| < |a|) \end{cases} \quad (25)$$

It should be noted that when non-uniform grids are employed (for example, when adaptive mesh refinement and coarsening is employed) the fluxes must be calculated together (for a total of $N_x * N_y$ fluxes). In this case, for a purely two-dimensional

simulations, the amount of flux from one cell to another can be calculated trivially by determining the overlap area $A = v_j v_k \Delta t^2$ (where there are $k = 1, \dots, N$ fluxes in the y -direction and v_k is calculated in the same manner as Eq. (21) divided by the source cell area $A_S = \Delta x \Delta y$, as shown in Figure 2-1. The mass m and the energy ε are thus given by:

$$m_{jk} = \frac{\left[\rho + \left(\Delta x_L \frac{d\rho}{dx} + \Delta y_L \frac{d\rho}{dy} \right) \right] \Delta x \Delta y w_j w_k}{\pi} \quad (26)$$

$$\varepsilon_{jk} = \frac{(\xi - \Omega) \left[\sigma + \left(\Delta x_L \frac{d\sigma}{dx} + \Delta y_L \frac{d\sigma}{dy} \right) \right]}{2} \quad (27)$$

where Δy_L is calculated in a similar manner to Δx_L . Thus the amount of mass m_{flux} , energy E_{flux} and momentum in each coordinate direction $p_{x,flux}$ and $p_{y,flux}$ which must be added to the destination cell and subtracted from the source cell are given by:

$$m_{flux} = \frac{A}{A_S} m \quad (28)$$

$$E_{flux} = \frac{A}{A_S} m \left[\frac{1}{2} (v_j^2 + v_k^2) + \varepsilon_{jk} \right] \quad (29)$$

$$p_{flux,x} = \frac{A}{A_S} m v_j \quad (30)$$

$$p_{flux,y} = \frac{A}{A_S} m v_k \quad (31)$$

A variable time step scheme is used to maintain the maximum kinetic Courant–Friedrichs–Levy (CFL) number in the domain below a desired value (usually ≤ 1). It is important to note that this CFL restriction is to maintain physical realism and is not related to the numerical stability of the scheme. For a two-dimensional or axisymmetric simulation, the CFL number is given by:

$$CFL = \frac{\left(\sqrt{(u^2 + v^2)} + q_{J(\max)} \sqrt{RT} \right) \Delta t}{\sqrt{(\Delta x^2 + \Delta y^2)}} \quad (32)$$

where $q_{J(\max)}$ is the maximum value of the particle abscissas (i.e. the value which gives the maximum particle thermal velocity).

In the current implementation boundary conditions are handled using ghost cells. These cells can be used to represent walls, stream boundaries, inflow boundaries and zero-gradient outflow boundaries. The interaction of a gas with a wall is identical to the interaction of that flow with an adjacent cell having the same flow properties but a reversed flow direction normal to the wall. The basic description of the simulation processes for QDS-2N method is available in Figure 2-2.

2.4 QDS-N² Method

2.4.1 Spatial Reconstruction and Flux Calculation

In the current study, referring to Figure 2-3, the general extension to higher order in QDS in one-dimensional case is performed using a spatial reconstruction of the form:

$$Q(x) = Q_c + \left(\frac{dQ}{dx} \right)_{x=0.5\Delta x} (x - 0.5\Delta x) + \left(\frac{d^2Q}{dx^2} \right)_{x=0.5\Delta x} \frac{(x - 0.5\Delta x)^2}{2} + \dots + \left(\frac{d^{n-1}Q}{dx^{n-1}} \right)_{x=0.5\Delta x} \frac{(x - 0.5\Delta x)^{n-1}}{(n-1)!} \quad (33)$$

where $Q(x)$ is the value of a conserved property (mass, momentum, or energy) at a distance x from the left hand side of the cell, and integer n indicates the order of the reconstruction. Note Q_c is the value of $Q(x)$ at the cell centre. This value is calculated from $Q(x)$ integrating over the cell width divided by the cell width equalling to the existing average value of the source cell \bar{Q}_s , presented below:

$$\begin{aligned}\bar{Q}_s &= \frac{1}{X_R - X_L} \int_{X_L}^{X_R} Q(x) dx \\ &= \left[Q_c x + \frac{1}{2} \left(\frac{dQ}{dx} \right) (x - 0.5\Delta x)^2 + \frac{1}{6} \left(\frac{d^2Q}{dx^2} \right) (x - 0.5\Delta x)^3 + \dots \right]_{x=X_L}^{x=X_R}\end{aligned}\quad (34)$$

By using our revised reconstruction, the bounds of integration are $X_L=0$ and $X_R=\Delta x$.

Then, Eq. (34) leads to:

$$\bar{Q}_s = Q_c + \frac{\Delta x^2}{24} \left(\frac{d^2Q}{dx^2} \right) + \frac{\Delta x^4}{1920} \left(\frac{d^4Q}{dx^4} \right) + \dots + \frac{2\Delta x^{n-1}}{n!} \left(\frac{1}{2} \right)^n \left(\frac{d^{n-1}Q}{dx^{n-1}} \right)\quad (35)$$

Alternatively, Q_c can be expressed as follows:

$$Q_c = \bar{Q}_s - \frac{\Delta x^2}{24} \left(\frac{d^2Q}{dx^2} \right) - \frac{\Delta x^4}{1920} \left(\frac{d^4Q}{dx^4} \right) - \dots - \frac{2\Delta x^{n-1}}{n!} \left(\frac{1}{2} \right)^n \left(\frac{d^{n-1}Q}{dx^{n-1}} \right)\quad (36)$$

where n is assumed to be an odd number. This shows that the correction is only required when the scheme is third order ($n = 3$) accurate or higher, otherwise $Q_c = \bar{Q}_s$ (e.g., $n=2$).

Thus, the complete correct form of the higher order reconstruction of $Q(x)$ using \bar{Q}_s contains additional terms on every even derivative:

$$\begin{aligned}Q(x) &= \left(\bar{Q}_s - \frac{\Delta x^2}{24} \left(\frac{d^2Q}{dx^2} \right) - \frac{\Delta x^4}{1920} \left(\frac{d^4Q}{dx^4} \right) \right) + \left(\frac{dQ}{dx} \right) (x - 0.5\Delta x) + \left(\frac{d^2Q}{dx^2} \right) \frac{(x - 0.5\Delta x)^2}{2!} \\ &\quad + \frac{1}{3!} \left(\frac{d^3Q}{dx^3} \right) (x - 0.5\Delta x)^3 + \left(\frac{d^nQ}{dx^n} \right) \frac{(x - 0.5\Delta x)^n}{n!}\end{aligned}\quad (37)$$

Specifically, as $n=2$, the above is reduced to the following form because of $Q_c = \bar{Q}_s$,

as shown below:

$$Q(x) = \bar{Q}_s + \frac{dQ}{dx} (x - 0.5\Delta x) + \frac{1}{2!} \frac{d^2Q}{dx^2} (x - 0.5\Delta x)^2\quad (38)$$

The above reduces to exactly the same form as in QDS-2N [Smith *et al.*, 2009].

Next, referring to Figure 2-4, the outgoing flux value of average conserved quantity successfully moving from the source cell into the destination cell (denoted by \bar{Q}_{tr}) is:

$$\begin{aligned}\bar{Q}_{tr} &= \frac{1}{(X_R - X_L)} \int_{X_L}^{X_R} Q(x) dx = \frac{1}{(X_R - X_L)} \left[Q_c x + \frac{1}{2} \left(\frac{dQ}{dx} \right) (x - 0.5\Delta x)^2 + \dots \right]_{x=\Delta x - u\Delta t}^{x=\Delta x} \\ &= Q_c + \frac{1}{(X_R - X_L)} \left[\frac{1}{2} \left(\frac{dQ}{dx} \right) (x - 0.5\Delta x)^2 + \dots \right]_{x=\Delta x - u\Delta t}^{x=\Delta x}\end{aligned}\quad (39)$$

where the bounds of integration are $X_L = \Delta x - u\Delta t$ and $X_R = \Delta x$.

Now, the transition of mean values \bar{Q}_{tr} can be used to calculate particle properties.

Assigning the flux out of average conserved properties \bar{Q}_{1tr} , \bar{Q}_{2tr} and \bar{Q}_{3tr} as the mass, momentum, and energy, respectively, the resulting QDS particle properties for particle J are:

$$m_J = \frac{\bar{Q}_{1tr} W_J}{\sqrt{\pi}}, \quad v_J = \frac{\bar{Q}_{2tr}}{\bar{Q}_{1tr}} + \left[\frac{2R}{(C_v)^2} \left(\frac{\bar{Q}_{3tr}}{\bar{Q}_{1tr}} - \frac{1}{2} \left(\frac{\bar{Q}_{2tr}}{\bar{Q}_{1tr}} \right)^2 \right) \right]^{\frac{1}{2}} q_J, \quad (40)$$

$$\varepsilon_J = \frac{(\xi - \Omega) R}{2} \left(\frac{\bar{Q}_{3tr}}{\bar{Q}_{1tr}} - \frac{1}{2} \left(\frac{\bar{Q}_{2tr}}{\bar{Q}_{1tr}} \right)^2 \right)$$

To calculate the average value of conserved property for higher order reconstruction, it is important how the flux limiting is coupled. According to the value of conserved property $Q(x)$ (see Eq. (33)), the gradient of Q_c is defined in flux limiting during the reconstruction process. In each cell, we employ the monotized central difference (MC) limiter to the effective gradients of conserved properties, as described below:

$$\left(\frac{dQ}{dx} \right) = \left(\frac{dQ}{dx} \right)_F \phi(\theta) \quad (41)$$

$$\phi(\theta) = \max \left(0, \min \left(2, \frac{\theta + 1}{2}, 2\theta \right) \right) \quad (42)$$

where ϕ is the equivalent flux limiter and F is the gradient calculated using forward differences. The theta θ is the ratio of the first order gradient calculated using forward and backward differences:

$$\theta = \left(\frac{dQ}{dx} \right)_B \left(\frac{dQ}{dx} \right)_F^{-1} \quad (43)$$

Therefore, an alternate representation of the variation of $Q(x)$ over space must be:

$$Q(x) = Q_c + \left[\left(\frac{dQ}{dx} \right)_F \phi(\theta) \right]_{x=0.5\Delta x} (x - 0.5\Delta x) + \frac{1}{2} \left[\left(\frac{d^2Q}{dx^2} \right)_F \phi(\theta) \right] (x - 0.5\Delta x)^2 + \dots + \frac{1}{n!} \left[\left(\frac{d^n Q}{dx^n} \right)_F \phi(\theta) \right]_{x=0.5\Delta x} (x - 0.5\Delta x)^n \quad (44)$$

2.4.2 One-Dimensional Flux Calculation and Implementation

In QDS simulations, we require flux from a volume to another volume. Since fluxes are split, the qualities of the flux depend entirely on the region from which they originated. The flux calculation is described as a flowchart in Figure 2-5, and summarized briefly as follows:

1. The gradients of conserved properties Q are first calculated using standard finite difference approximations in each cell i . For example, for a 5th order accurate reconstruction, one might use the stencils like:

$$\left(\frac{dQ}{dx} \right)_i = \left(\frac{Q_{i+1} - Q_{i-1}}{\Delta x} \right) \quad \left(\frac{d^2Q}{dx^2} \right)_i = \left(\frac{Q_{i+1} + Q_{i-1} - 2Q_i}{2\Delta x} \right) \quad (45)$$

$$\left(\frac{d^3Q}{dx^3} \right)_i = \frac{1}{\Delta x^2} \left(\left(\frac{dQ}{dx} \right)_{i+1} + \left(\frac{dQ}{dx} \right)_{i-1} - \left(\frac{dQ}{dx} \right)_i \right)$$

$$\left(\frac{d^4Q}{dx^4} \right)_i = \frac{1}{\Delta x^2} \left(\left(\frac{d^2Q}{dx^2} \right)_{i+1} + \left(\frac{d^2Q}{dx^2} \right)_{i-1} - \left(\frac{d^2Q}{dx^2} \right)_i \right)$$

2. For each QDS particle:

- a. Calculate the approximate particle velocity based on the current cell \overline{Q}_s , which should give the same particle velocity as 1st order QDS.

$$v_J = \frac{\overline{Q}_{s2}}{\overline{Q}_{s1}} + \left[\frac{2R}{C_v^2} \left(\frac{\overline{Q}_{s3}}{\overline{Q}_{s1}} - \frac{1}{2} \left(\frac{\overline{Q}_{s2}}{\overline{Q}_{s1}} \right)^2 \right) \right]^{\frac{1}{2}} q_J \quad (46)$$

- b. Calculate the integral bounds X_L and X_R :

$$\text{If } V > 0, \left\{ \begin{array}{l} X_R = \Delta x - u\Delta t \\ X_L = \Delta x \end{array} \right\}, \text{ otherwise } \left\{ \begin{array}{l} X_R = 0 \\ X_L = u\Delta t \end{array} \right\} \quad (47)$$

- c. Calculate the flux out values of average conserved properties \overline{Q}_{tr} of particles to successfully move into the destination region.
- d. Calculate the particle properties based on the average values \overline{Q}_{tr} .
- e. Calculate the fluxes of conserved properties to neighbouring cells following the standard QDS algorithm in subsection 2.2.

2.4.3 Two-Dimensional Flux Calculation and Implementation

Multi-dimensional extension is performed using the same principles applied for a one-dimensional reconstruction. The variation of conserved quantity $Q(x, y)$ over two-dimensional space is assumed to be:

$$\begin{aligned} Q(x, y) = & Q_c \\ & + \left(\frac{dQ}{dx} \right)_{x=0.5\Delta x} (x - 0.5\Delta x) + \left(\frac{d^2Q}{dx^2} \right)_{x=0.5\Delta x} \frac{(x - 0.5\Delta x)^2}{2} + \dots + \left(\frac{d^{n-1}Q}{dx^{n-1}} \right)_{x=0.5\Delta x} \frac{(x - 0.5\Delta x)^{n-1}}{(n-1)!} \\ & + \left(\frac{dQ}{dy} \right)_{y=0.5\Delta y} (y - 0.5\Delta y) + \left(\frac{d^2Q}{dy^2} \right)_{y=0.5\Delta y} \frac{(y - 0.5\Delta y)^2}{2} + \dots + \left(\frac{d^{n-1}Q}{dy^{n-1}} \right)_{y=0.5\Delta y} \frac{(y - 0.5\Delta y)^{n-1}}{(n-1)!} \end{aligned} \quad (48)$$

The subsequent cell centred value of Q_c is:

$$\begin{aligned}
Q_c = \bar{Q}_s - \frac{\Delta x^2}{24} \left(\frac{d^2 Q}{dx^2} \right) - \frac{\Delta x^4}{1920} \left(\frac{d^4 Q}{dx^4} \right) \cdots - \frac{2\Delta x^{n-1}}{n!} \left(\frac{1}{2} \right)^n \left(\frac{d^{n-1} Q}{dx^{n-1}} \right) \\
- \frac{\Delta y^2}{24} \left(\frac{d^2 Q}{dy^2} \right) - \frac{\Delta y^4}{1920} \left(\frac{d^4 Q}{dy^4} \right) \cdots - \frac{2\Delta y^{n-1}}{n!} \left(\frac{1}{2} \right)^n \left(\frac{d^{n-1} Q}{dy^{n-1}} \right)
\end{aligned} \tag{49}$$

Following this, the average value of conserved quantity in the region bound by $[X_L, Y_B] - [X_R, Y_T]$ is formulated as:

$$\begin{aligned}
\bar{Q}_r = \frac{1}{(X_R - X_L)(Y_T - Y_B)} \int_{Y_B}^{Y_T} \int_{X_L}^{X_R} Q(x, y) dx dy = Q_c \\
+ \frac{1}{(X_R - X_L)} \left[\left[\left(\frac{dQ}{dx} \right) \frac{(X_R - 0.5\Delta x)^2}{2} \cdots + \left(\frac{d^{n-1} Q}{dx^{n-1}} \right) \frac{(X_R - 0.5\Delta x)^n}{n!} \right] \right. \\
\left. - \left[\left(\frac{dQ}{dx} \right) \frac{(X_L - 0.5\Delta x)^2}{2} \cdots + \left(\frac{d^{n-1} Q}{dx^{n-1}} \right) \frac{(X_L - 0.5\Delta x)^n}{n!} \right] \right] \\
+ \frac{1}{(Y_T - Y_B)} \left[\left[\left(\frac{dQ}{dy} \right) \frac{(Y_R - 0.5\Delta y)^2}{2} \cdots + \left(\frac{d^{n-1} Q}{dy^{n-1}} \right) \frac{(Y_R - 0.5\Delta y)^n}{n!} \right] \right. \\
\left. - \left[\left(\frac{dQ}{dy} \right) \frac{(Y_L - 0.5\Delta y)^2}{2} \cdots + \left(\frac{d^{n-1} Q}{dy^{n-1}} \right) \frac{(Y_L - 0.5\Delta y)^n}{n!} \right] \right]
\end{aligned} \tag{50}$$

where Y_T and Y_B are the bounds of integration in y direction.

Since the average requires bounding regions in both translational directions, application of splitting (as applied to TDEFM to improve computational efficiency) is impossible, and the full N^2 number of particles (i.e. nine when three particles are used per direction, sixteen for four, etc.) are required for a complete flux computation. Previous extensions required only the $2N$ particles. Unlike the one-dimensional reconstruction, each particle carries three separate fluxes (for three different destination cells) and so any single QDS particle possesses three “sub-particles” based on different integral bounds. This concept is demonstrated in Figure 2-6, showing each unique sub-region (A – C). The area of the sub-region A is $u \times v \times dt$ as described earlier in Section 2.2 for the QDS-2N method.

2.4.4 Three-Dimensional Flux Calculation and Implementation

As previous section, the three-dimensional flux calculation is followed the same way for a one-dimensional reconstruction. The variation of conserved quantity $Q(x, y)$ over three-dimensional space is assumed as follows:

$$\begin{aligned}
 Q(x, y, z) = & Q_c \\
 & + \left(\frac{dQ}{dx} \right)_{x=0.5\Delta x} (x - 0.5\Delta x) + \left(\frac{d^2Q}{dx^2} \right)_{x=0.5\Delta x} \frac{(x - 0.5\Delta x)^2}{2} + \dots + \left(\frac{d^{n-1}Q}{dx^{n-1}} \right)_{x=0.5\Delta x} \frac{(x - 0.5\Delta x)^{n-1}}{(n-1)!} \\
 & + \left(\frac{dQ}{dy} \right)_{y=0.5\Delta y} (y - 0.5\Delta y) + \left(\frac{d^2Q}{dy^2} \right)_{y=0.5\Delta y} \frac{(y - 0.5\Delta y)^2}{2} + \dots + \left(\frac{d^{n-1}Q}{dy^{n-1}} \right)_{y=0.5\Delta y} \frac{(y - 0.5\Delta y)^{n-1}}{(n-1)!} \\
 & + \left(\frac{dQ}{dz} \right)_{z=0.5\Delta z} (z - 0.5\Delta z) + \left(\frac{d^2Q}{dz^2} \right)_{z=0.5\Delta z} \frac{(z - 0.5\Delta z)^2}{2} + \dots + \left(\frac{d^{n-1}Q}{dz^{n-1}} \right)_{z=0.5\Delta z} \frac{(z - 0.5\Delta z)^{n-1}}{(n-1)!}
 \end{aligned} \tag{51}$$

The subsequent cell centred value of Q_c is:

$$\begin{aligned}
 Q_c = \bar{Q}_s - & \frac{\Delta x^2}{24} \left(\frac{d^2Q}{dx^2} \right) - \frac{\Delta x^4}{1920} \left(\frac{d^4Q}{dx^4} \right) \dots - \frac{2\Delta x^{n-1}}{n!} \left(\frac{1}{2} \right)^n \left(\frac{d^{n-1}Q}{dx^{n-1}} \right) \\
 & - \frac{\Delta y^2}{24} \left(\frac{d^2Q}{dy^2} \right) - \frac{\Delta y^4}{1920} \left(\frac{d^4Q}{dy^4} \right) \dots - \frac{2\Delta y^{n-1}}{n!} \left(\frac{1}{2} \right)^n \left(\frac{d^{n-1}Q}{dy^{n-1}} \right)
 \end{aligned} \tag{52}$$

Following this, the average value of conserved quantity in the region bound by $[X_L, Y_B, Z_I] - [X_R, Y_T, Z_O]$ is formulated as:

$$\begin{aligned}
\bar{Q}_v &= \frac{1}{(X_R - X_L)(Y_T - Y_B)(Z_O - Z_I)} \int_{Z_I}^{Z_O} \int_{Y_B}^{Y_T} \int_{X_L}^{X_R} Q(x, y, z) dx dy = Q_c \\
&+ \frac{1}{(X_R - X_L)} \left\{ \left[\left(\frac{dQ}{dx} \right) \frac{(X_R - 0.5\Delta x)^2}{2} \dots + \left(\frac{d^{n-1}Q}{dx^{n-1}} \right) \frac{(X_R - 0.5\Delta x)^n}{n!} \right] \right. \\
&\quad \left. - \left[\left(\frac{dQ}{dx} \right) \frac{(X_L - 0.5\Delta x)^2}{2} \dots + \left(\frac{d^{n-1}Q}{dx^{n-1}} \right) \frac{(X_L - 0.5\Delta x)^n}{n!} \right] \right\} \\
&+ \frac{1}{(Y_T - Y_B)} \left\{ \left[\left(\frac{dQ}{dy} \right) \frac{(Y_R - 0.5\Delta y)^2}{2} \dots + \left(\frac{d^{n-1}Q}{dy^{n-1}} \right) \frac{(Y_R - 0.5\Delta y)^n}{n!} \right] \right. \\
&\quad \left. - \left[\left(\frac{dQ}{dy} \right) \frac{(Y_L - 0.5\Delta y)^2}{2} \dots + \left(\frac{d^{n-1}Q}{dy^{n-1}} \right) \frac{(Y_L - 0.5\Delta y)^n}{n!} \right] \right\} \\
&+ \frac{1}{(Z_O - Z_I)} \left\{ \left[\left(\frac{dQ}{dz} \right) \frac{(Z_O - 0.5\Delta z)^2}{2} \dots + \left(\frac{d^{n-1}Q}{dz^{n-1}} \right) \frac{(Z_O - 0.5\Delta z)^n}{n!} \right] \right. \\
&\quad \left. - \left[\left(\frac{dQ}{dz} \right) \frac{(Z_I - 0.5\Delta z)^2}{2} \dots + \left(\frac{d^{n-1}Q}{dz^{n-1}} \right) \frac{(Z_I - 0.5\Delta z)^n}{n!} \right] \right\} \tag{53}
\end{aligned}$$

where Z_O and Z_I are the bounds of integration in z direction.

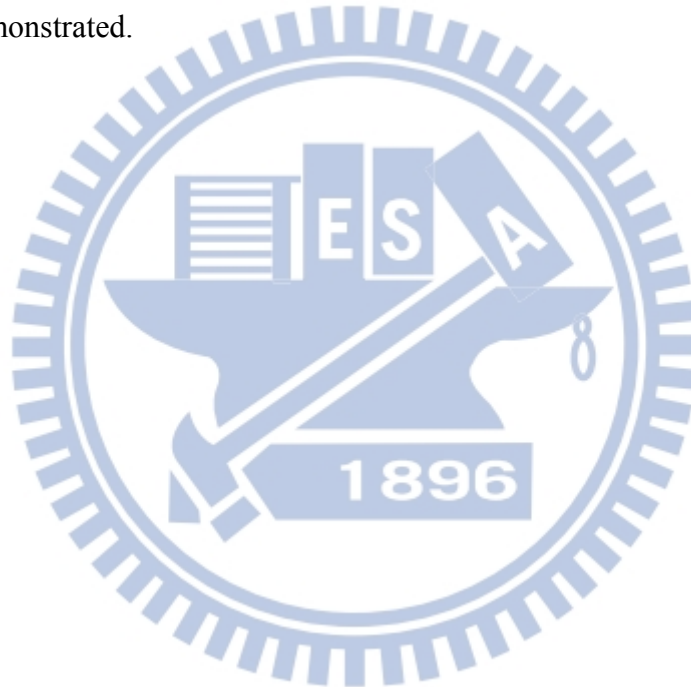
The N^2 number of particle is 27 which 3 particles are used in one direction. Therefore, each particle must be completed calculation for flux reconstruction in a time step. Especially the calculation for diagonal cell, the particle has 7 sub-regions (A – G) to be considered which are based on the difference bound. The concept is same as section 2.4.5 demonstrated in Figure 2-7.

2.5 Brief Summary

The characterization of the QDS- N^2 method developed in this chapter can be summarized as follows:

1. The QDS method replaces the random sampling method used in the DSMC method. Particles are permitted to move in physically realistic directions; therefore flux exchange is not limited to cells sharing an adjacent interface as in conventional direction decoupled finite volume solvers.

2. In QDS method, the particles are recreated deterministically from the properties stored on the mesh using Gauss–Hermite quadrature weights and abscissas.
3. The QDS- N^2 and QDS-2N methods use the same procedure to calculate flux reconstruction in one-dimension.
4. In the QDS- N^2 method, particle properties are updated, considering the average value of the conserved quantity between the region bounds, which are required in translational directions and the application of splitting.
5. With parallel implementation, an extension to three-dimensional QDS method is also demonstrated.



Chapter 3

Complex Gas Flow Simulations using the QDS-N²

Method

3.1 Introduction

To determine the effectiveness of the QDS algorithm, several test cases, including three cases of one-dimensional domain, six of two-dimensional domain, and one of three-dimensional domain were used. The test cases were chosen for the following reasons:

- The cases are suitable for solving the Euler equation.
- The benchmark is well known and many numerical methods or experimental results are available for comparison.
- All qualitative, quantitative, computational, and experimental results are readily available.

The QDS-2N and QDS-N² methods are compared for both accuracy and computational time. We also parallelize the QDS-N² method to increase calculation speed. As well, the literature related to the test cases is surveyed to determine useful benchmarks to which the present code can be compared.

3.2 QDS Method in One-Dimension Flow

3.2.1 Shock Tube

The shock tube is an important application in unsteady wave motion, the study of high-temperature gases in physics and chemistry, and the testing of supersonic bodies

and hypersonic entry vehicles. Figure 3-1 shows the features of a shock tube after the diaphragm has been broken. The region to the left of the diaphragm is the driver section and the region to the right is the driven section.

We consider the shock tube problem to validate the accuracy of the QDS code, especially a Riemann solver [Toro, 1999], which represents the majority of solution methods. The initial condition for the simulation consists of two constants:

$$(\rho, v, T) = \begin{cases} (10.0, 0.0, 1.0) & 0 \leq x < 0.5, \\ (1.0, 0.0, 1.0) & 0.5 \leq x \leq 1. \end{cases} \quad (54)$$

To compare the results easily, we set the number of cells for QDS and the Riemann solver to 200. Simulation time is 0.1 s, and the walls are reflected. Figure 3-2 shows density results for the first to the third order QDS and the Riemann solver. We observed a great improvement between the first and the second orders. Although the second and the third order QDS results are closer to the benchmark than first order results, the improvement between the second and the third order is negligible.

3.2.2 Shock-blast wave interaction

The shock blast problem suggested as a benchmark in [Woodward *et al.*, 1984] included two blast waves contacted by strong shocks. By initial pressure jumps, this version of the problem will indicate a flow containing three distinct fluids.

The initial condition for simulation is expressed as:

$$(\rho, v, p) = \begin{cases} (1.0, 0.0, 10^3) & 0.0 \leq x < 0.1 \\ (1.0, 0.0, 10^{-2}) & 0.1 \leq x < 0.9 \\ (1.0, 0.0, 10^2) & 0.9 \leq x \leq 1.0 \end{cases} \quad (55)$$

Each result was examined at time 0.038 s. The reflective boundary condition is applied to both ends. The comparable benchmark is an almost identical to shock tube interaction using the WENO-3 scheme (fifth order) [Jiang *et al.*, 1996] with 10,000

grids. The benchmark is used to measure errors by comparing the different methods considered here. Figure 3-3 shows a contrasting profile of the density computed by the QDS method with 400 cells using the MC limiter. As can be seen, the second order QDS method is much better than the first order, and the third order QDS method is slightly better than the second order. The difference between second and third order schemes can be seen easily at a range of 0.7 to 0.8 in the x direction. However, the pre-QDS method can be extended to calculate the case in which acoustic wave oscillation is quite large. Therefore, the next test case considers the pre-QDS method, which is an easy way to measure the oscillation accurately by ignoring the limiter.

3.2.3 Shock acoustic wave interaction

An ideal case for testing the general one-dimensional extension of the pre-QDS method is the interaction of a Mach 3 shock wave with an acoustic wave as proposed by Shuv [Shu, *et al.*, 1988]. When a higher density shock wave contacts a smooth acoustic wave, an amplified wave with higher frequency results. The initial conditions are:

$$\left(\rho, v, P \right) = \begin{cases} \left(3.857143, 2.629369, 10.333333 \right) & x < -4, \\ \left(1.0 + \frac{1}{5} \sin 5x, 0.0, 1.0 \right) & -4 \leq x. \end{cases} \quad (56)$$

Results for various QDS configurations with 200 cells compared to a WENO [Huang, *et al.*, 2009] benchmark with 2000 cells are shown in Figure 3-4. The result is obtained at time 1.8 and the limiter is not applied. The improvement from first to second order is the most significant; higher orders show only slight improvement. The general trend is in agreement with the WENO benchmark and third order QDS solutions that result in similar levels of dissipation to those of a fifth-order WENO solution.

3.3 QDS Method in Two-Dimension Flow

In this section, we present four test cases for comparing the N^2 and $2N$ methods. The major discussions focus on the time cost and accuracy between the two methods in two-dimensional problems.

3.3.1 Shock-Bubble Interaction

The strength of correct multi-dimension reconstruction is demonstrated in two dimensions with the shock/bubble interaction problem [Čada *et al.*, 2009]. The initial conditions for this problem are shown in Figure 3-5. The simulation calculated a shock wave, moving from left to right with a velocity of Mach number 2.85 in an ideal, inviscid gas and interacting with a pseudo bubble at $x=0.3$. The results are presented at $t=0.2$. The results of the numerical schlieren (gradients of density) are presented in Figure 3-6 for various QDS methods and the TVD schemes on a grid of 1700×500 cells. The application of correct multi-dimensional reconstructions results in a relatively high resolution of the circulation and reflected shock located at $x = 0.6$.

Figure 3-7 displays two QDS methods with different numbers of cells. We compare the N^2 method (Figure 3-7a) against the $2N$ method (Figures 3-7b, c and d) by using 300×100 , 450×150 , and 600×200 cells. For the sake of comparison, the limiter for each simulation is the monotonized central (MC) limiter. In Figures 3-7a and b the difference in resolution is clear despite the fact that both these methods employ the same number of cells. As the number of cells employed by the $2N$ method increases (shown up to 600×200 cells here), the results gradually approach those of the N^2 scheme with relatively few cells (1/4). Obviously, the multi-dimensional computation (N^2 method) achieves higher accuracy than the $2N$ scheme.

Further, we consider the computation time required by each method in this case. The N^2 method is true-directional, in that each possible combination of discrete velocity

must be considered (nine instances with three discrete velocities per direction), while the 2N method employs approximate dimensional extension and only requires six discrete velocity computation in a two-dimensional computation. Moreover, for each particle, three space-averaging computations are required for each fraction falling into separate destination cells. Therefore, the N^2 method requires more computation time for the same number of cells. The computation time of the two solvers are summarized in Table 3-1. According to these data, the N^2 extension of QDS requires approximately three times the computation time as compared to that of the original 2N method for the same number of cells. However, for any given degree of accuracy, we find that the N^2 method provides an increase in computational efficiency of almost three times (300×100 vs. 600×200 for 2N vs. N^2). Thus, the application of the N^2 method is justified over that of the 2N method for high-resolution solutions.

3.3.2 Euler-Four-Shocks problem

This test case was introduced in Serna[2006], which computed the numerical solution employing the piecewise hyperbolic method-Marquina's flux formula (PHM-MFF) and power PHM-MFF schemes. The test problem is initially divided into four quadrants sharing a common corner at 0.75 and 0.75 in the domain $[0,1] \times [0,1]$, as illustrated in Figure 3-8. These quadrants initially have the following different but uniform conditions:

$$(\rho, u, v, p) = \begin{cases} (1.5, 0, 0, 1.5), & [0.75, 1] \times [0.75, 1] \\ (0.5323, 1.206, 0, 0.3), & [0, 0.75) \times [0.75, 1] \\ (0.138, 1.206, 1.206, 0.029), & [0, 0.75) \times [0, 0.75) \\ (0.5323, 0, 1.206, 0.3), & [0.75, 1] \times [0, 0.75) \end{cases} \quad (57)$$

Figure 3-9 shows four results of a comparison between the 2N and N^2 solvers at the time of 0.4. The Courant–Friedrichs–Lewy factor (CFL) is set as 0.5. We compare

the results of the two QDS solvers using 100×100 to 300×300 cells. As can be seen, the result of the QDS N^2 solver obtained using a coarse grid (100×100 cells) is only approached by the $2N$ solver when employing considerably fine grids (300×300 cells). Furthermore, the result we obtained using the QDS N^2 solver on a computational grid of 1000×1000 cells is similar to that obtained using the TVD-MUSCL scheme [Čada *et al.*, 2009] (see Figure 3-10a).

An investigation of the computational expense of each scheme showed that the N^2 solver takes approximately four times longer to complete the simulation than the $2N$ solver. This comparison of computational expense is summarized in Table 3-2. The increase in computational time with the refinement of the computational grid is due to the constant “kinetic” CFL condition that we employ, which is defined as follows:

$$CFL = \text{Max} \left(\left(\frac{(\sqrt{u^2 + 3 * \sqrt{RT}}) * dt}{dx} \right), \left(\frac{(\sqrt{v^2 + 3 * \sqrt{RT}}) * dt}{dy} \right) \right) \quad (58)$$

This basically ensures that particles in free flight do not travel further than the adjacent cells. Although the result take more time to compute using the N^2 solver, the accuracy is considerably better than that of the $2N$ solver, in fact, it is not clear that the $2N$ solver will ever approach the solution obtained using the N^2 solver, irrespective of the number of cells employed.

3.3.3 Euler-Four-Contacts problem

This test case involves the Euler-four-contacts interaction problem defined by Schulz-Rinne, Collins, and Glaz [Schulz-Rinne *et al.*, 1993]. The same test case with a different higher-order method is also presented in [Salichs *et al.*, 2005]. This Riemann problem briefly shows four constant states consisting of four quadrants and two shocks generated clockwise at the origin. The contact point is cantered about the location (x,

$y)=(0.5, 0.5)$. A representation of the structure of the flow domain is shown in Figure 3-11. The initial flow condition is imposed by four difference shock waves and satisfies the following relation:

$$(\rho, u, v, p) = \begin{cases} \left(1, 0.75, -0.5, 1 \right), & [0.5, 1] \times [0.5, 1] \quad (A) \\ \left(2, 0.75, 0.5, 1 \right), & [0, 0.5] \times [0.5, 1] \quad (B) \\ \left(1, -0.75, 0.5, 1 \right), & [0, 0.5] \times [0, 0.5] \quad (C) \\ \left(3, -0.75, -0.5, 1 \right), & [0.5, 1] \times [0, 0.5] \quad (D) \end{cases} \quad (59)$$

Figure 3-12 shows the numerical result of the second-order TVD-MUSCL method for a density contour profile on a 1000×1000 uniform grid, taken from [Čada *et al.*, 2009]. For the QDS method, the result obtained at the time of 0.8 on a 1000×1000 uniform grid can be seen in Figure 3-13. Two results are shown for the second-order method with the N^2 and $2N$ solvers. Both enforce a constant CFL number of 0.25. The contours of density are presented with levels of 0 to 2.4. In this case, a shock wave is generated and spirals from the contact point in an unsteady fashion. By comparing the two figures, we find that both the N^2 and the $2N$ solver results are symmetrical and that the result obtained using the N^2 solver is closer to the TVD-MUSCL result presented in Figure 3-12. As in the previous test cases, in the current test case, the accuracy of the N^2 method is superior to that of the $2N$ method. In this instance, however, the WENO results [Schulz-Rinne *et al.*, 1993] are still superior to the N^2 results: this can be attributed to the small stencil employed for the estimation of the higher-order gradients, or to flux splitting employed and the inevitably associated numerical dissipation; this may require further investigation.

Further, we have compared the timings and the accuracy for this test problem with different N for both QDS- $2N$ and QDS- N^2 with 1000×1000 cells since both schemes

scale differently with N . The results are essentially the same as those obtained for $N = 3$ when N increases to 5 or 9 for both the abovementioned methods, as shown in Figure 3-14. This is reasonable since the integration of a Gaussian function with a polynomial, having two or less degrees, becomes exact, if the number of Gaussian-Hermite integration points is 3 or more. Expectedly, the computation time increases roughly 3 times from $N = 3$ to $N = 9$ for both the methods. Further, Figure 3-15 shows the density contours when the grid resolution increases from 1000×1000 cells to 2000×2000 and 3000×3000 cells. In brief summary, for both the QDS-2N and the QDS- N^2 methods for solving the Euler equation, accuracy effectively increases with increasing grid resolution, while it is essentially the same when $N \geq 3$.

3.3.4 Mach 3 Flow over a Forward Step

The fourth test problem for the second-order QDS method is the Mach 3 flow over a forward facing step in a high-speed wind tunnel. The main of this case is designed to solve complex oblique shock reflections. This problem was first introduced by Emery [Emery *et al.*, 1968] and has since been used by Woodward and Colella to test a number of differencing schemes [Woodward *et al.*, 1984]. The same problem using second order QDS scheme was used by Smith [2009] to demonstrate that QDS the effectively captures all features of the flow fluid and compare with Keats and Lien's scheme [Keats *et al.*, 2004]. Keats mentions that this case is well known problem to evaluate the robustness of numerical method. It is difficult to maintain positivity pressure and density using various numerical methods when the strong shock reflection at a step during first time step. Therefore, this test case has proven to be a well test for a long time by several of methods. For QDS method, it must be more careful to deal with particle actions facing the corner of the step. That will useful for us to expend a laugh of

blocks in a domain.

Here present the geometry and boundary conditions used in the problem (see Figure 3-16). As an initial condition, the flow is everywhere uniform at Mach 3 with a density of 1.4, a pressure of 1.0, gas constant $R = 1.0$ and a specific heat ratio $c = 1.4$. The CFL number is set as 0.1. This is equivalent to an impulsively started flow and the simulations capture the unsteady development of the flow structure.

The QDS simulations utilized a second-order scheme and third-order with 4 QDS particles per cell on a uniform grid consisting of 100,800 square cells (the number of cells for total domain which included the step is 600×200). The number of contours is 30 from 0.2568 to 6.067. Figure 3-17 shows the density profile generated using two QDS solver – 2N solver and N^2 solver – at time = 4.0 s. The result is compared with that of Keats and Lien who employed a second order Godunov method on an adaptively refined mesh [Keats *et al.*, 2004]. We observe the results in both figures are similar whenever the solver is 2N or N^2 solver.

3.3.5 Shock Wave Diffraction over a 90 degree sharp corner

This test case uses the same geometrical as previous test case which a block in the domain. The geometric configuration of this case is the forward-facing steps. This case is also an important case to observe shock wave diffraction which is designed to solve the Euler equation. The shock wave diffraction induces more phenomena in the perturbed region behind the shock [Skews, 1967]. Those included shock wave, vortex, terminator and an incident sound wave. The problem contain both computational and the mathematical studies. Secondly, the experimental results are available for variety of geometries and Mach number [Takayama *et al.*, 1991]. More numerical studies can be found from Skews [1967], Schardin [Dyke, 1997], Bazhenova [Bazhenova *et al.*, 1984].

Figure 3-18 shows structure of the perturbed region behind a diffracting shock wave presented from Skews [1967]. Skews performed experiments for a variety of Mach numbers and convex corner angles and has outlined the structure of the perturbed region. The detail of the structure is described in appendix A.

The output format of this case shows in Figure 3-19[Takayama *et al.*, 1991]. The incident shock Mach number is 1.5 which the normal shock moves to right. The isopycnics are to be displayed with each isopycnic corresponding to an increase of 4% of the initial density. The geometry and boundary conditions of this test case can be seen in Figure 3-20. The normal shock wave which propagates through space to the right is set at the edge of the step between the fluid state 1 and state 2. The moving shock Mach number M_s is defined as:

$$M_s = \frac{W}{a_1} \quad (60)$$

where W is velocity of the gas ahead of the shock wave, relate the wave. a_1 is the speed of the sound of the gas in state 1. Figure 3-21 illustrates the schematic of moving shock waves relating the W , u_p , state 1 and 2. The W is important for that is relates the wave velocity of the moving shock wave to the pressure ratio across the wave and the speed of sound of the gas into which the wave is propagating, shown as follows (derived in [Anderson, 1990]):

$$W = a_1 \sqrt{\frac{\gamma+1}{2\gamma} \left(\frac{p_2}{p_1} - 1 \right) + 1} \quad (61)$$

the velocity U_p behind the wave in state 2 is defined as:

$$u_p = W \left(1 - \frac{p_1}{p_2} \right) \quad (62)$$

The initial velocity in the state 1 is set to zero. The x-component of the initial velocity in the state 2 is set to u_p . Table 3-3 summarizes the temperature ratio, density

ratio and up initial conditions for the moving shock Mach number M_s , determined from [Anderson, 1990]. The simulation time t is depend on the location of the incident shock, which is approximately $W \times t$. For example in this test case, the incident shock is 1.3L as shown in Figure 3-19 , the initial normal shock wave is set at the 0.3L where near from inlet boundary on the edge of the step, the simulation time is 1.464.

Figure 3-22 shows three density results that obtain using the second-order TVD extension of Godunov method [Takayama *et al.*, 1991], N^2 and 2N method with 400×400 cells. The vortex obtained using both QDS method below the slipstream is close to the benchmark. The position of the vortex, incident shock and slipstream are perfectly in the correct please as the second-order TVD extension of Godunov method [Takayama *et al.*, 1991].It is able to gauge the ability of the QDS method to detect shock, contact and expansion regions. To compare with experimental result made by Ritzerfeld *et al.* [Takayama *et al.*, 1991], the schlieren result is easily to identify that the vortex obtained using N^2 method is clearer to observe as we can see from Figure 3-23. According the results in this test case, the accuracy obtain using N^2 method is considerably better than that of the 2N method.

3.3.6 Advection of Vortical Disturbance

The final test case consists of an inviscid unsteady flow in which a vortex is located at the canter of a uniform domain (x_c, y_c) . The mean flow for this case uses Mach number $M_\infty=0.1$. The case tests the capabilities of the QDS method compared to the exact solution taken from [Visbal *et al.*, 1999] in order to accurately advent vertical disturbance. This problem also appears in Tutkun and Bdis [Tutkun *et al.*, 2010]. The initial conditions are shown as follows:

$$\begin{aligned}
u &= U_\infty - \frac{C(y-y_c)}{dx} \exp\frac{-r^2}{2}, \quad v = \frac{C(x-x_c)}{dy} \exp\frac{-r^2}{2} \\
p - p_\infty &= \frac{\rho C^2}{2R_c^2} \exp(r^2), \quad r^2 = \frac{(x-x_c)^2 + (y-y_c)^2}{R_c^2}
\end{aligned} \tag{63}$$

where u , v and R_c determine the Cartesian velocity components and the vortex radius. C is the vortex strength parameter, defined as follows:

$$\frac{C}{(U_\infty R_c)} = 0.02 \tag{64}$$

The density is assumed to be constant and the vortex radius R_c is taken to be 1.0 in this case.

Figure 3-24 shows the vorticity contours of the N^2 and the 2N methods with 800×800 cells using the second-order method. The limiter in this case is the monotized central (MC) method. A constant CFL number (0.1) is enforced such that the non-dimensional time step size is $\Delta t U_\infty / R_c = 4.0 \times 10^{-3}$. The result of the N^2 solver is essentially the same as the exact solution and shows a perfect circular shape of the vorticity distribution while that of the 2N solver does not. The result of the 2N solver shows more significant dissipation and anisotropy errors as compared to that of the N^2 solver. Figure 3-25 shows the vorticity distributions of various simulations along a horizontal line (at $y = 8.0$) passing through the vortex center in Figure 3-24. We have compared the results obtained by using the two solvers (2N and N^2) on a uniform grid containing three different levels of resolution (160×160 , 800×800 , and 1600×1600 cells). The result obtained using the N^2 solver in the case of 800×800 cells is in excellent agreement with the exact solution and radial symmetry, while the results obtained using the 2N solver are far from the correct solution even in the case of 1600×1600 cells. Thus, the influence of multi-dimensional reconstruction is significant for the

QDS, particularly on the numerical accuracy of the solution for a gas flow field as in the current problem.

The investigation of the computational expense again reveals a trade-off between computational time and accuracy. The computational time of the N^2 solver in terms of calculation time is approximately 3~4 times less than that of the $2N$ solver for any given computational grid although the accuracy of the former is considerably better than that of the latter. This leads to a question whether the use of the N^2 method is worthwhile or not. Thus, we compare the results obtained using the N^2 method using 160×160 cells with those obtained using the $2N$ method using 1600×1600 cells, as shown in Figure 3-25. The results show that they are essentially the same for the same level of accuracy; thus, the proposed the N^2 solver is approximately 25 times faster than the $2N$ solver in this case. Once again, we are unsure whether the $2N$ result will ever converge to the analytical solution, thereby justifying the application of the N^2 solver and its proposed multi-dimensional reconstruction of QDS particles.

3.4 QDS Method in Three-Dimension Flow

The three-dimensional QDS method is necessary to develop a complete method for large-scale domains. Such a method will cover many problems that the two-dimensional method cannot solve. In this paper, the second-order QDS- N^2 method is extended to a three-dimensional method. This extension is non-trivial and requires the application of a number of modifications. These modifications are required in QDS but not in conventional finite volume schemes because fluxes are calculated from volume to volume, incorporating the influence of spatially varying primitive quantities, and because the scheme is based on kinetic theory rather than a solution to a governing set of equations. The scheme is validated by simulating a simple test case.

3.4.1 Mach 2 Flow over a Pillar

This test case is to validate the three-dimensional method can be available as the two-dimensional method. The geometry represented in Figure 3-26 shows a pillar in the center of the domain facing a Mach number 2.0 in the x-direction. The y- and z-components of initial velocity are set to zero. The initial density and the temperature are set to 1.0. The number of cells is set to $200 \times 200 \times 100$ in a full domain $(x, y, z) = (1.0, 1.0, 0.5)$. The results are presented at $t = 0.1$ with the MINMOD limiter, and the CFL number is set to 0.5. The results obtained using N^2 method in a three-dimensional domain are compared to results obtained in a two-dimensional domain in Figure 3-27. The results for both domains are identical. This indicates that the results obtained in a three-dimensional domain can calculate any of those obtained in a two-dimensional domain without computational error. This case is an easy way to identify that the QDS code can be applied to a three-dimensional domain. Furthermore, we observe the same flow condition with a block in the center of the domain, as shown in Figure 3-28. Compared with Figure 3-27 b, the results are evident in the x-y surface. Note that Figure 3-29 shows different results. The z-component is considered in the three-dimensional domain but not in the two-dimensional domain. Therefore, it is evident that the three-dimensional method is necessary.

Furthermore, in both two- and three-dimensional simulation domains, the computational time increases when the number of cells is increased. Therefore, we improved the QDS method to include parallel code. Performance results are presented in the next section.

3.5 Parallel Computing of QDS method

As described in the previous section, although the accuracy of the results for the N^2 method in the two-dimensional flow is higher than the $2N$ method, computational time is longer. The capacity of the N^2 technique can be increased by parallelizing the code so that computational load is shared across a number of processors. In this section, a parallel QDS method is discussed. In addition, various code improvements and a validation simulation are also discussed.

3.5.1 Overview of Parallel Implementation

Parallel computing involves the division of a task into smaller subtasks and the assignment of such subtasks to individual processors. These processors perform the subtasks and communicate when required. One method for dividing work between processors is domain (or data) decomposition into subdomains. In one-dimensional decomposition, the subdomains are determined by latitude or longitude; in two-dimensional decomposition they are determined by both latitude and longitude.

In this work, we introduce the Message Passing Interface (MPI) to the N^2 code to speed up computation time. MPI is a parallel computer message-passing library for communication among processes that have separate address spaces.

3.5.2 Simulation Conditions

A 2D shock-bubble interaction problem is simulated to obtain the computation time for the parallel N^2 method, as shown in Figure 3-30. The initial condition is as same as Section 3.3.1, i.e., Mach 2.81 with pressure 10 from $x = 0$ moving to the right will face a low density gas bubble. The computational problem is a symmetric domain with a boundary at $y \geq 0$, reflecting boundary condition at $y = 0.5$ and inflow at $x = -0.1$.

3.5.3 Parallel Performance

Strong and weak scaling are two basic ways to measure the parallel performance of a given application, depending on whether the application is CPU bound or memory bound.

Tables 3-4 to 3-7 summarize the computational time using the parallel N^2 method. The results were computed on the ALPS–Acer AR585 F1 Cluster at the National Center for High-performance Computing (NCHC) of Taiwan. The F1 Cluster uses the AMD Opteron 6174 processor with 12 cores operating at 2.2 GHz and 128 GB of main memory (per node).

3.5.3.1 Weak Scaling

Weak scaling is used for programs that require significant memory or other system resources. The purpose of this measurement is to observe the run time while maintaining a constant or line scaling as the relationship between the number of processors and cells is gradually increased. Weak scaling efficiency is given as:

$$\left(\frac{t_N}{t_1} \right) 100\% \quad (65)$$

where t is the time required to complete a job unit. The subscript indicates the number of processors. t_N is the amount of time required to complete N job units with N processors.

The results of weak scaling for a shock-bubble interaction case are presented in Table 3-4. In this case, the largest number of processor is 122, and the largest number of cells is 2.4 million. Each process is assigned a constant number of cells (20,000 grids). Simulation time is 0.2 with 2000 time-steps.

Figure 3-30 shows a weak scaling diagram for the shock-bubble interaction case using the parallel N^2 method. The results summarized in Table 3-4 show that the

efficiency of this case is approximately 1.2. The ideal efficiency of weak scaling is 1.0, which is denoted by the dash-dot line in Figure 3-30 (60 processors). The average efficiency achieved (1.2) is an acceptable result. The result indicates that, when we employ larger core counts to simulate a problem with the N^2 method, 20% of computation is consumed communicating data.

3.5.3.2 Strong Scaling

Strong scaling, which fixes computational domain size but increases the number of processors, is also used to measure the parallel performance of a given application. Strong scaling is used to determine a reasonable length of time to process a relatively large application using many processors without excessive overhead cycles. Strong scaling efficiency is give as:

$$N \left(\frac{t_N}{t_1} \right) 100\%. \quad (66)$$

where t is the time required to complete a job unit. The subscript indicates the number of processors. t_N is the amount of time required to complete N job units with N processors.

In this section, in Tables 3-5 to 3-7, we present three strong scaling performance results for different numbers of cells, representing small, medium, and large-scale domains. These tables show the relationships among computation time, number of processors, and number of cells per processor. The largest number of processors we consider is 256. As shown in Figure 3-31, for a 2D shock-bubble problem using 500,000 cells and 2,000 time steps, there was a net increase in speed of approximately 78% when compared with ideal performance (red line). As illustrated in Figures 3-32 and 3-33, for 2 million and 12.5 million cells, the speed up was 68.5% and 65.5%,

respectively. On the other hand, if we compare results for the three cases when the number of cells per processor is equal, the results are approximately equal. For example, for 125,000 cells per processor, computation times are 2761.14 s, 2890.74 s, and 2806.29 s. This indicates that, regardless of the size of the computational domain, we can obtain a rational answer using the same number of cells for each processor.

3.6 Brief Summary

The major findings of the study of the QDS algorithm for the N^2 and $2N$ methods can be summarized as follows:

1. The one-dimensional QDS method extended to a higher order method is useful for simulating the shock acoustic wave problem and can be used to compute higher-order problems.
2. Using the N^2 method in a two-dimensional domain obtains results comparable to the benchmark. The accuracy achieved using the N^2 method is considerably better than that achieved using the $2N$ method.
3. The N^2 extension of the QDS method requires approximately three times the computation time compared to the original $2N$ method for the same number of cells.
4. For both the $2N$ and the N^2 methods, when solving the Euler equation, accuracy effectively increases with increasing grid resolution. However, it is essentially the same when $N \geq 3$.
5. The advection of vertical distribution test case results show that both methods are essentially equally accurate; however, the proposed the N^2 solver is approximately 25 times faster than the $2N$ solver.

6. The QDS method is suitable for three-dimensional computation and can be applied to three-dimensional simulation problems.
7. Parallel performance studies, including strong and weak scaling, show that the parallel efficiency for a large-scale problem (0.5, 2, and 12.5 million cells) can reach up to 75%, 68.5%, and 65.5%, respectively, using 256 processors at the NCHC APLS cluster.



Chapter 4

Analysis of QDS-2N Method as Compared to QDS- N² Method

4.1 Introduction

In the previous section, we identify the difference between 2N and N² method by comparing with several numerical methods as benchmark. Since both one-dimensional 2N and N² method are theoretical the same. The major difference of both methods is mathematically the flux reconstruction travelled to the diagonal cell in two-dimension. In this chapter, we use an analytical aspect to discuss the difference and to observe which flow condition is suitable for N² method or 2N method for simulation.

4.2 Derivation of Analytical Fluxes of QDS Methods (2N vs. N²)

4.2.1 Mass Flux

According to chapter 2, the different part of two methods is flux reconstruction in two-dimension. Here we present the fluxes value which contributed to correct cell after a time step Δt when the source cell travelled to the diagonal destination cell in Figure 1. The net of mass fluxes M_{2N} obtained from 2nd order 2N method shows blow.

$$M_{2N} = \frac{1}{\pi} \frac{m'_x m'_y}{m} w_j^2 \left(\frac{\Delta t}{\Delta x} \left(\frac{P'_x}{m'_x} + \sqrt{2 \frac{R}{C_v} \left(\frac{E'_x}{m'_x} - \frac{1}{2} \left(\frac{P'_x}{m'_x} \right)^2 - \frac{1}{2} \left(\frac{P'_y}{m'_y} \right)^2} \right)} \right) q_J \right) \left(\frac{\Delta t}{\Delta y} \left(\frac{P'_y}{m'_y} + \sqrt{2 \frac{R}{C_v} \left(\frac{E'_y}{m'_y} - \frac{1}{2} \left(\frac{P'_x}{m'_x} \right)^2 - \frac{1}{2} \left(\frac{P'_y}{m'_y} \right)^2} \right)} \right) q_J \right) \quad (67)$$

where $m'_x, m'_y, P'_x, P'_y, E'_x, E'_y$ are the value of conserved properties (mass, momentum, energy) for 2nd order in x and y-direction . Those are described blow,

$$m'_x = m + \frac{1}{2} \frac{dm}{dx} (\Delta x - u \Delta t) \quad m'_y = m + \frac{1}{2} \frac{dm}{dy} (\Delta y - v \Delta t) \quad (68)$$

$$P'_x = P_x + \frac{1}{2} \frac{dP_x}{dx} (\Delta x - u \Delta t) \quad P'_y = P_y + \frac{1}{2} \frac{dP_y}{dy} (\Delta y - v \Delta t) \quad (69)$$

$$E'_x = m \left(C_v T + \frac{1}{2} u^2 + \frac{1}{2} v^2 \right) + \frac{1}{2} \frac{dE}{dx} (\Delta x - u \Delta t) \quad (70)$$

$$E'_y = m \left(C_v T + \frac{1}{2} u^2 + \frac{1}{2} v^2 \right) + \frac{1}{2} \frac{dE}{dy} (\Delta y - v \Delta t) \quad (71)$$

the total mass, momentum and energy in the source cell is m , P_x , P_y , E .

On the other hand, the analytical mass flux equation M_N^2 obtained from 2nd order N² method is

$$M_{N^2} = \frac{1}{\pi} m'_{n^2} w_J^2 \left[\frac{\Delta t}{\Delta x} \left(\frac{P'_{x_{N^2}}}{m'_{N^2}} + \sqrt{2 \frac{R}{C_v} \left(\frac{E'_{N^2}}{m'_{N^2}} - \frac{1}{2} \left(\frac{P'_{x_{N^2}}}{m'_{N^2}} \right)^2 - \frac{1}{2} \left(\frac{P'_{y_{N^2}}}{m'_{N^2}} \right)^2} \right)} \right) q_J \right] \quad (72)$$

$$\left[\frac{\Delta t}{\Delta y} \left(\frac{P'_{y_{N^2}}}{m'_{N^2}} + \sqrt{2 \frac{R}{C_v} \left(\frac{E'_{N^2}}{m'_{N^2}} - \frac{1}{2} \left(\frac{P'_{x_{N^2}}}{m'_{N^2}} \right)^2 - \frac{1}{2} \left(\frac{P'_{y_{N^2}}}{m'_{N^2}} \right)^2} \right)} \right) q_J \right]$$

where the subscript shows N^2 is the value of conserved properties for N² method described as follows:

$$m'_{N^2} = m + \frac{1}{2} \frac{dm}{dx} (\Delta x - u \Delta t) + \frac{1}{2} \frac{dm}{dy} (\Delta y - v \Delta t) \quad (73)$$

$$P'_{y_{N^2}} = P_y + \frac{1}{2} \frac{dP_y}{dx} (\Delta x - u \Delta t) + \frac{1}{2} \frac{dP_y}{dy} (\Delta y - v \Delta t) \quad (74)$$

$$P'_{x_{N^2}} = P_x + \frac{1}{2} \frac{dP_x}{dx} (\Delta x - u \Delta t) + \frac{1}{2} \frac{dP_x}{dy} (\Delta y - v \Delta t) \quad (75)$$

$$E'_{N^2} = m \left(C_v T + \frac{1}{2} u^2 + \frac{1}{2} v^2 \right) + \frac{1}{2} \frac{dE}{dx} (\Delta x - u \Delta t) + \frac{1}{2} \frac{dE}{dy} (\Delta y - v \Delta t) \quad (76)$$

As we can see, the difference of 2N and N² method for net mass flux form source cell to the diagonal destination cell is presented

$$M_{N^2} - M_{2N} \quad (77)$$

The difference of 2N method can be identified form Eq.(78).

$$\left| \frac{M_{N^2} - M_{2N}}{M_{N^2}} \right| 100\% \quad (78)$$

4.2.2 Momentum Fluxes

The momentum flux is performed using the same principles applied for two-dimensional reconstruction of mass flux. The momentum flux for the 2N method in x-component and y-component can be described as follows:

$$P_{x_{2N}} = M_{2N} \left(\frac{P'_x}{m'_x} + \sqrt{2 \frac{R}{C_v} \left(\frac{E'_x}{m'_x} - \frac{1}{2} \left(\frac{P'_x}{m'_x} \right)^2 - \frac{1}{2} \left(\frac{P'_y}{m'_y} \right)^2 \right)} q_J \right) \quad (79)$$

$$P_{y_{2N}} = M_{2N} \left(\frac{P'_y}{m'_y} + \sqrt{2 \frac{R}{C_v} \left(\frac{E'_y}{m'_y} - \frac{1}{2} \left(\frac{P'_x}{m'_x} \right)^2 - \frac{1}{2} \left(\frac{P'_y}{m'_y} \right)^2 \right)} q_J \right) \quad (80)$$

The N^2 method of momentum fluxes in x-component $P_{x_{N^2}}$ and in y-component $P_{y_{N^2}}$ are present as below:

$$P_{x_{N^2}} = M_{N^2} \left(\frac{P'_{x_{N^2}}}{m'_{N^2}} + \sqrt{2 \frac{R}{C_v} \left(\frac{E'_{N^2}}{m'_{N^2}} - \frac{1}{2} \left(\frac{P'_{x_{N^2}}}{m'_{N^2}} \right)^2 - \frac{1}{2} \left(\frac{P'_{y_{N^2}}}{m'_{N^2}} \right)^2 \right)} q_J \right) \quad (81)$$

$$P_{y_{N^2}} = M_{N^2} \left(\frac{P'_{y_{N^2}}}{m'_{N^2}} + \sqrt{2 \frac{R}{C_v} \left(\frac{E'_{N^2}}{m'_{N^2}} - \frac{1}{2} \left(\frac{P'_{x_{N^2}}}{m'_{N^2}} \right)^2 - \frac{1}{2} \left(\frac{P'_{y_{N^2}}}{m'_{N^2}} \right)^2 \right)} q_J \right) \quad (82)$$

To simplify the equation of momentum fluxes, those equations are described with the net of mass flux reconstruction. The net momentum fluxes in two components are described as follows:

$$P_{x_{-N^2}} - P_{x_{-2N}}, \quad P_{y_{-N^2}} - P_{y_{-2N}} \quad (83)$$

The difference of 2N method can be identified from Eq. (83):

$$\left| \frac{P_{x_{-N^2}} - P_{x_{-2N}}}{P_{x_{-N^2}}} \right| 100\% \quad , \quad \left| \frac{P_{y_{-N^2}} - P_{y_{-2N}}}{P_{y_{-N^2}}} \right| 100\% \quad (84)$$

4.2.3 Energy Flux

Follow the previous section, the energy fluxes of the 2N method are divided with Eq. (68) ~ Eq. (71), shown in below:

$$E_{2N} = M_{2N} \left[\begin{array}{l} \left(\frac{1}{2} \left(\frac{P'_x}{m'_x} + \sqrt{2 \frac{R}{C_v} \left(\frac{E'_x}{m'_x} - \frac{1}{2} \left(\frac{P'_x}{m'_x} \right)^2 - \frac{1}{2} \left(\frac{P'_y}{m'_y} \right)^2} \right)} q_J \right)^2 \right. \\ \left. + \frac{1}{2\Omega C_v} \left(\frac{2C_v}{R} - \Omega \right) \left(\frac{E'_x}{m'_x} - \frac{1}{2} \left(\frac{P'_x}{m'_x} \right)^2 - \frac{1}{2} \left(\frac{P'_y}{m'_y} \right)^2 \right) \right) \\ \left(\frac{1}{2} \left(\frac{P'_y}{m'_y} + \sqrt{2 \frac{R}{C_v} \left(\frac{E'_y}{m'_y} - \frac{1}{2} \left(\frac{P'_x}{m'_x} \right)^2 - \frac{1}{2} \left(\frac{P'_y}{m'_y} \right)^2} \right)} q_J \right)^2 \right. \\ \left. + \frac{1}{2\Omega C_v} \left(\frac{2C_v}{R} - \Omega \right) \left(\frac{E'_y}{m'_y} - \frac{1}{2} \left(\frac{P'_x}{m'_x} \right)^2 - \frac{1}{2} \left(\frac{P'_y}{m'_y} \right)^2 \right) \right) \end{array} \right] \quad (85)$$

where Ω is the number of simulated degrees of freedom (i.e. in this chapter, $\Omega = 2$). The energy fluxes in N^2 method is described by following equation:

$$E_{N^2} = M_{N^2} \left[\begin{array}{l} \frac{1}{2C_v} \left(\frac{2C_v}{R} \right) \left(\frac{E'_{N^2}}{m'_{N^2}} - \frac{1}{2} \left(\frac{P'_{x_{-N^2}}}{m'_{N^2}} \right)^2 - \frac{1}{2} \left(\frac{P'_{y_{-N^2}}}{m'_{N^2}} \right)^2 \right) + \\ \frac{1}{2} \left(\frac{P'_{x_{-N^2}}}{m'_{N^2}} + \sqrt{2 \frac{R}{C_v} \left(\frac{E'_{N^2}}{m'_{N^2}} - \frac{1}{2} \left(\frac{P'_{x_{-N^2}}}{m'_{N^2}} \right)^2 - \frac{1}{2} \left(\frac{P'_{y_{-N^2}}}{m'_{N^2}} \right)^2} \right)} q_J \right)^2 \\ \frac{1}{2} \left(\frac{P'_{y_{-N^2}}}{m'_{N^2}} + \sqrt{2 \frac{R}{C_v} \left(\frac{E'_{N^2}}{m'_{N^2}} - \frac{1}{2} \left(\frac{P'_{x_{-N^2}}}{m'_{N^2}} \right)^2 - \frac{1}{2} \left(\frac{P'_{y_{-N^2}}}{m'_{N^2}} \right)^2} \right)} q_J \right)^2 \end{array} \right] \quad (86)$$

Therefore, the net energy flux is combined with Eq. (85) and Eq. (86) that can be formulated as

$$E_{N^2} - E_{2N} \quad (87)$$

According to Eq. (87), the difference of two methods can be shown that

$$\left| \frac{E_{N^2} - E_{2N}}{E_{N^2}} \right| 100\% \quad (88)$$

4.3 Results and Discussion

4.3.1 Diagrams of Relative Difference Distribution

In order to estimate the difference between the two methods, the unknown elements in the equation have to be defined. The test cases that we simulate contain a domain of 1000×1000 cells; the cell size in the x and y directions is $1.0e^{-3}$ ($\Delta x = \Delta y = 1.0e^{-3}$), and the time step Δt is equal to $1.0e^{-4}$. The density, velocity, and temperature are changed from 0.1 to 5.0, which are observed for the difference in the fluxes. Therefore, the CFL number is calculated to be 0.01–0.5 on the basis of the changing value of the density, velocity, and temperature. The gradients for all the conserve properties are assumed to be $1.0e^{-5}$ and $1.0e^{-6}$ for two cases. Therefore, on the basis of our assumptions, we calculate the difference in density ($\Delta\rho$) to be $1.0e^{-2}$ for the first case by using the mass gradient shown in Eq. (67). Furthermore, the difference in velocity (Δv , Δu) and temperature (ΔT) are obtained in the same manner. For another case, the difference in the density, velocity, and temperature are $1.0e^{-3}$.

$$\frac{dm}{dx} = \frac{V\Delta\rho}{\Delta x} = 1.0e^{-5} \quad (89)$$

The purpose of this simulation is to estimate the difference in the fluxes between the 2N and the N^2 methods in terms of the mass flux, momentum flux, and energy flux

on the basis of the variations of the density, velocity, and energy observed when the source cell travels to the diagonal destination cell. We compare two cases in which the differences in the density, velocity, and temperature are $1.0e^{-2}$ and $1.0e^{-3}$, respectively.

Figure 4-1a shows the mass value of the difference between the 2N and the N^2 method in the density, velocity, and temperature range from 0.1 to 5.0. Most of the significant difference in the mass flux is observed in the low-density range, and in particular, the largest difference is observed when the temperature is equal to 0.1 and the velocity is increased to 2.5. Another range in which we can clearly see the difference is the low-density and low-velocity range in which the temperature is either low or high. The tendency of case 2 for the largest difference is shown in Figure 4-1b. The other results of the comparison of the difference between the two methods with respect to the momentum and the energy are shown in Figures 4-2 to 4-4.

As we can see from the figures, the highest value of the difference is obtained in the low-density range. Figure 4-5 shows two cases when the difference value is in the low-density range. We compare velocity with the value of mass flux for three temperatures that each of them has the lowest point which is 1.2, 2.1, and 2.6. Even case 2 has the same lowest point as case 1.

Therefore, when the simulation domain is in the low-density, low-temperature, and high-velocity range, the accuracy obtained using the N^2 method is considerably better than that obtained using the 2N method.

4.3.2 Example with Large Difference

In the previous section, we discussed that most of the different fluxes between 2N and N^2 are around two parts: the first part is at the low density, low speed, and the second part is at the low density, low temperature, and high speed as shown in Figures

4-1 to 4-4. In order to validate the discussion, section 4.3.1 is provided; here, we discuss four test cases, namely shock-bubble interaction, Euler-four-shock, and Mach 3 over a forward step and a backward step.

4.3.2.1 Shock-Bubble Interaction

The first test case is demonstrated in the same manner as the preceding case discussed in Section 3.3.1. The comparisons shown in the schlieren image show that the accuracy obtained by using the N^2 method is considerably better than that obtained by using the 2N method. Although both methods can identify the right position for the shock wave, the result obtained using the 2N method does not describe specifically at a complex place, especially in the bubble. In this section, we discuss in more detail, the conditions in the fluid that lead to a more significant difference between the two methods. Figure 4-6 shows the four contours of the N^2 method, namely density, temperature, and two dimensions of velocity. The result obtained is the same as that shown in Figure 3-6. According to Figure 3-6, most differences are almost around the $x = 0.6\sim 0.7$ and $y = 0.1\sim 0.15$ region. In order to analyze the result, the properties around the bubble that attacked after the shock wave are considered to be low density, high temperature, and high velocity. In order to observe higher difference of two methods, we decrease the temperature of the bubble from 10 to 2 initially. The schlieren result shows that the N^2 method describes more details than the 2N method at a low density and a low temperature as shown in Figure 4-7. The density and the temperature contours of this result are illustrated in Figures 4-8 and 4-9. The temperature contour shows a more considerable difference between the two methods than the density contour. As expected, the difference between the two methods is more distinct in the complex

region. Therefore, the complex region provides more specific results in the low-density environment in the case of the N^2 method.

4.3.2.2. Euler-Four-Shock Simulation

The analytical fluxes that we discussed in the previous section are focused on the diagonal direction. The first case gave a hint about the difference between the two methods in a complex fluid. Therefore, the second test case combines the diagonal direction and the complex flow introduced in Salichs [2006]. The benchmark is used for computing the numerical solution employing the piecewise hyperbolic method-Marquina's flux formula (PHM-MFF) and the power PHM-MFF schemes. The test problem is initially divided into four quadrants sharing a common corner at 0.75 and 0.75 in the domain $[0, 1] \times [0, 1]$, as illustrated in Figure 3-8. These quadrants initially have the relationship shown in Eq. (57).

The result that we obtained using the N^2 solver on a computational grid of 1000×1000 cells at the time of 0.4 is similar to that obtained using the total variation diminishing-monotone upstream centered schemes for conservation laws (TVD-MUSCL) [Čada *et al.*, 2009] (see Figure 3-10a). The Courant–Friedrichs–Lewy (CFL) factor is set as 0.5. All three approximations obtain the basic structure of the solution where the four shock waves interact. Three results show that the position of the shock wave is the same as that shown in Figure 3-10. However, the area from $(x, y) = (0.2, 0.2)$ to $(0.4, 0.4)$ is not for the $2N$ method that has less variation. The differences between the N^2 and the $2N$ methods are observed in the contact area. In the same way, in order to analyze the differences, we observe four properties of the contour results of the N^2 method in Figure 4-10. The results indicate that the density and the temperature in the contact area are lower than those in any other area. According to Figure 4-10, it is

reasonable to explicate why the accuracy of the N^2 method is better than that of the 2N method.

4.3.2.3 Mach 3 Flow over a Forward Step

This case is designed for a high-speed velocity model through a forward step and involves complex oblique shock reflections. The inlet and the outlet boundary conditions in the domain are both supersonic flows. The geometry of the test case is illustrated in Figure 3-16, and the result of the flow is shown in Figure 3-17. The purpose of this test case is to demonstrate that the two methods obtain approximately the same result. Since a normal shock wave moves along the x direction, the flux reconstruction calculated in the diagonal direction is not considered to be significant. Based on the discussion presented in Section 4.3.1, we know that most of the differences in the flux can be observed in the diagonal direction. Moreover, the oblique shocks usually occur with an increase in the temperature, pressure, and density. This is contrary to the definition of the difference between both the QDS methods carried out under low-density, low-temperature, and high-velocity conditions. Figures 4-11 and 4-12 show that the density and the temperature contours use the same initial flow and boundary conditions as those discussed in Section 3.3.4. The results revealed a considerably high density and temperature; few results of low density and temperature were observed behind a corner. The most obvious discrepancy between the 2N method, the N^2 method, and Keats's results is the location of the shock reflection on the upper wall. The point located at $x = 2.4$ is the contact point between an incident shock and a reflected shock obtained using the N^2 method; it is at the same position as that in Keats's result. Consequently, the results reveal two not-so-apparent differences: first,

the flow properties as low velocity, high density, and high temperature; and second, the flow around the shock wave and the oblique shock.

4.3.2.4 Shock Wave Diffraction over a 90-degree Sharp Corner

Different from the preceding geometric configuration, the oblique shock does not occur in this test case instead of secondary physical phenomena such as a second shock, contact surface, and vortex. The last case discussed in this chapter involves the use of the same geometrical and boundary conditions as those considered in the case discussed in Section 3.3.5. The initial conditions of the flow for M_s are listed in Table 3-3. According to the explanation of the structure of the perturbed region by Skews [1967], the location of the vortex is well defined for $M_s < 1.5$. Therefore, in order to observe more secondary physical phenomena in this test case, we discuss the case of shock wave diffraction by using the initial flow velocity of $M_s = 2.4$. The experimental result obtained by Schardun [Dyke, 1997] is selected as the benchmark. The flow structure around a perturbed region is outlined in Appendix A. Because the comparison has an experimental result as a benchmark, the resolutions of the simulation are calculated using a considerably fine cell: 1000×1000 uniform grids. The CFL number is set to 0.2. The simulation time is calculated using the same principle as that discussed in Section 3.3.4 and is $t = 0.775$.

Figure 3-13 shows three schlieren results using the second-order 2N method, N^2 method, and the experimental result separately. These results can be used for gauging the ability of these methods to detect the expansion region by juxtaposing them with the three results shown in Figure 3-18. The shape of the primary shock wave shown in Figure 3-13b and c matches the experimental result. The secondary shock waves obtained using the two methods are accurately located at the correct position behind the

wall and between the slipstream and the contact surface corresponding to the experimental result. The accuracy of the second shock wave in both the results is clear. However, the phenomena in the vortex and the contact surface of both the results are contrary to the second shock. It is obvious that the vortex obtained using the N^2 method is presented in considerable detail than that obtained using the 2N method. The contact wave is considerably diffused as compared to that in the case of the N^2 method and the experimental result. The density, temperature, and velocity contours in this case are shown in Figures 4-14 to 4-16. These results show that the vortex belongs to the region with a low density, low temperature, and high velocity. The contact surface in the results is shown in the region of low density, low temperature, and low velocity. This is reasonable for supporting the theory in Section 4.3.1 that a more significant difference between the two methods shows the same trend as the large discrepancy is in the region of low density, low temperature, and low velocity.

4.4 Brief Summary

The major findings of the study of the difference analysis of the QDS-2N method presented in this chapter can be summarized as follows:

1. There are two regions of flow properties where a large discrepancy of conservative fluxes occurs between the QDS-2N and the QDS- N^2 methods. The first is in the region of low density (down to 1.0), low temperature (down to 2.5), and high velocity (up to 2.0). The second is in the region of low density and low velocity (down to 1.2).
2. The conservative fluxes of the QDS-2N method that move along the diagonal direction exhibit a considerably large difference as compared to the QDS- N^2

method. In contrast, the conservative fluxes that move along the horizontal or the vertical direction exhibit a significantly smaller discrepancy.

3. The normal shock and oblique shock waves in the resolution obtained by using the two methods are approximately located in the same region, and most of the shock waves, as predicted by the QDS-2N method, move in the diagonal direction.
4. Because the properties of an after-expansion wave are low density, low temperature, and high velocity, we have found a large discrepancy between the QDS-2N method and the QDS-N² method.



Chapter 5

Conclusion and Recommendations of Future Work

5.1 Summary

In this thesis, a true-direction multi-dimensional higher-order extension of the QDS method, referred to as the QDS- N^2 method, for solving the inviscid Euler equation is investigated numerically and theoretically. The major findings of this thesis are summarized in the following two sections in turn.

5.1.1 Numerical Investigation of QDS- N^2 Method

1. The results of the one-dimensional shock and acoustic wave interaction problem demonstrate an improvement for higher orders of accuracy (up to third-order) of the QDS- N^2 method.
2. The QDS- N^2 method improves the solution in the flows unaligned with the computational grid as compared to the QDS-2N method.
3. The QDS- N^2 method significantly reduced the amount of numerical dissipation within the solution as compared to the QDS-2N method.
4. Despite the additional computational expense associated with the QDS- N^2 method for the same computational grid, for any given degree of accuracy, the proposed solver was found to be several times (up to 25 times in the case of the advection of vortical disturbances) faster than the original QDS-2N method.
5. Of particular interest is the test case of the advection of vortical disturbances, where the QDS- N^2 method improves the radial symmetry of the result

approaching the analytical solution, while the QDS-2N method failed to converge to the analytical solution even when a very fine grid is used.

6. The results are essentially the same when $N \geq 3$ because the integration of the Gauss function with a polynomial (degree ≤ 2) using the Gauss-Hermite integration technique becomes exact.
7. Parallel performance studies, including strong and weak scaling, show that the parallel efficiency of shock bubble interaction for a large-scale problem (0.5, 2, and 12.5 million cells) can reach up to 75%, 68.5%, and 65.5% respectively using 256 processors at the APLS cluster of National Center for High-Performance Computing, Taiwan.
8. Parallel performance of weak scaling shows that the average efficiency of shock bubble interaction using 20,000 cells per processor is about 1.2, which the ideal efficiency is 1.0.

5.1.2 Theoretical Analyses of Conservation Fluxes of QDS-2N Method and QDS-N² Method

1. There are two regions of flow properties where a large discrepancy of conservative fluxes occurs between the QDS-2N and the QDS-N² methods. The first is in the region of low density (down to 1.0), low temperature (down to 2.5), and high velocity (up to 2.0). The second is in the region of low density, and low velocity (down to 1.2).
2. The conservative fluxes of the QDS-2N method that moves along the diagonal direction has considerably large difference as compared to the QDS-N² method. On the contrary, the conservative fluxes move along horizontal or vertical direction has a much smaller discrepancy.

3. The normal shock and oblique shock wave in the flow obtained using two methods are approximately located in the same region, even the direction of the shock wave, predicted by the QDS-2N method, moves to be more in diagonal direction.
4. Because the properties of an after expansion wave are in the region of low density, low temperature, and high velocities, we have found that a large discrepancy occurs between the QDS-2N method and the QDS-N² method.

5.2 Recommendations of Future Work

In this thesis, we have demonstrated that the QDS-N² method is a very fast numerical method without being subject to convergence problem like conventional CFD methods. However, there are several areas need to be done in pushing the method forward, The areas outlined below should be examined in the future:

- To further reduce the computational time for large-scale multi-dimensional problems, the method should be implemented on multiple extension graphics processing units (GPU).
- To further reduce the numerical diffusion, a high-order stencil in calculating the conservative fluxes may be considered.
- To implement an adaptive mesh function in the region where large gradient of flow properties occurs.
- To extend the QDS-N² method for modelling the Navier-Stokes equation by employing the Chapmann-Engskog expansion theory to account for the viscous effect.

References

- [1] Albright B.J. Don S. Lemons, Michael E. Jones, and Dan Winske., 2002, “Quiet direct simulation of Eulerian fluids,” *Phys. Rev. E*, Vol. 65, pp.1-4.
- [2] Albright B.J, W. Daughton, D.S. Lemons, D. Winske, and M.E. Jones, 2002, “Quiet direct simulation of plasmas,” *Phys. Plasma*, Vol. 9, Issue 5,pp. 1898.
- [3] Anderson J. D.,1990, *Modern Compressible Flow*. McGraw-Hill, New York.
- [4] Bazhenova T. V., Gvozdeva L. G., and Nettleton M. A., 1984, “Unsteady interactions of shock waves.” *Prog. Aerospace Sci.*, Vol. 21, pp. 249–331.
- [5] Bird G.A., 1994, *Molecular Gas Dynamics and the Direct Simulation of Gas Flows*, Clarendon Press, Oxford.
- [6] Bird G.A., 1963, “Approach to translational equilibrium in a rigid sphere gas,” *Phys. Fluids*, Vol. 6, pp. 1518-1519.
- [7] Boyd I.D., Y. Jafry and J.V. Beukel, 1994, “Particle simulations of helium micro thruster flows,” *J. Spacecraft Rockets*, Vol. 31, Issue 2, pp. 271-277.
- [8] Cave H.M., C.-W. Lim, M.C. Jermy, S.P. Krumdieck, M.R. Smith Y.-J. Lin, and J.-S. Wu, 2010, “Multi-Species Fluxes for the Parallel Quiet Direct Simulation (QDS) Method,” in: *Proceedings of 27th International Symposium on Rarefied Gas Dynamics*.
- [9] Čada M., Torrilhon M., 2009, “Compact third-order limiter functions for finite volume methods,” *J. Compt. Phys.*, Vol.228, pp. 4118-4145.
- [10] Coronell D.G. and K.F. Jensen, 1992, “Analysis of Transition Regime Flows in Low Pressure Chemical Vapor Deposition Reactors Using the Direct Simulation Monte Carlo Method,” *J. Electro chemical. Soc.*, Vol. 8, pp. 2264-2273.
- [11] Chen W.F., 2003, “Study of hybrid DSMC/EPsm method,” *Chin. J. Comput. Phys.* Vol. 20, Issue 3, pp. 274.

- [12] Cook G., 1998, "High accuracy capture of curved shock fronts using the method of space-time conservation element and solution element," in: Proceedings of 37th AIAA Aerospace Sciences Meeting and Exhibit.
- [13] Culbert B. Laney, 1998, "Computational Gasdynamics," Cambridge University Press.
- [14] Dyke M. van, 1997, An Album of Fluid Motion. Parabolic Press, Stanford.
- [15] Gardiner C.W., 1985, "Handbook of Stochastic methods," 2nd ed., Springer, New York, pp.106-107.
- [16] Gombosi T.I., 1994, Gaskinetic Theory, Cambridge University Press, Cambridge.
- [17] Godlewski, Edwige, 1996, "Numerical approximation of hyperbolic systems of conservation laws," Springer, New York.
- [18] Huang J.-C., Lin Heng, Yang J.-Y., 2009, "Implicit preconditioned WENO scheme for steady viscous flow computation," *J. Comp. Phys.*, Vol. 228, pp. 420-438.
- [19] Hirsch C., 1990, "Numerical Computation of Internal and External Flows, Vol. 2," John Wiley & Sons, New York.
- [20] Jameson A., W. Schmidt and E. Turkel, 1981, "Numerical solution of the Euler equations by finite volume methods using Runge-Kutta time-stepping schemes," the 14th Aerospace Sciences Meeting, AIAA-81-12S9.
- [21] Jameson A., T. J. Baker and N. P. Weatherill, 1986, "Calculation of inviscid transonic flow over a complete aircraft," AIAA24th Aerospace Sciences Meeting, AIAA -86-0103.
- [22] John D. Anderson Jr., 1995, Computational Fluid Dynamics.

- [23] Jiang G., Shu C.-W., 1996, "Efficient implementation of weighted ENO schemes," *J. Comp. Phys.*, Vol. 126, pp. 202–228.
- [24] Keats W.A., Lien F.S., 2004, "Two-dimensional anisotropic Cartesian mesh adaptation for the Euler Equations," *Int. J. Numer. Meth. Eng.*, Vol. 46, pp. 1099.
- [25] Kröner D, 1997, "Numerical Schemes for Conservation Laws." Wiley Teubner.
- [26] Le Beau G. J. and F. E. Lumpkin III, 2001, "Application highlights of the DSMC Analysis Code (DAC) software for simulating rarefied flows," *Comp. Meth. Appl. Mech. Eng.* Vol. 191, Issue 6, pp. 595-609.
- [27] Lim Chin Wai, Hadley M. Cave, Mark C. Jermy, Susan P. Krumdieck and Jong-Shinn Wu, 2010, "An Approximate Method for Solving Unsteady Transitional and Rarefied Flow Regimes in Pulsed Pressure Chemical Vapor Deposition Process using the Quiet Direct Simulation Method," in: Proceedings of 27th International Symposium on Rarefied Gas Dynamics, California.
- [28] LeVeque R. J., 2004, "The dynamics of pressureless dust clouds and delta waves," *J. Hyperbolic Differential Equations*, Vol 1, pp. 315-327.
- [29] Karniadakis G.E. and A. Beskok, 2002, "Micro flows: fundamentals and simulation" Springer, New York.
- [30] Kwon M.-K. and Y.-K. Hwang, 2006, "A Study on the Pumping Performance of a Molecular Drag Pump in the Rarefied Gas Flow," in: Proceedings of 25th International Symposium on Rarefied Gas Dynamics, St. Petersburg, Russia.
- [31] MacCormack R. W. and B. S. Baldwin, 1975, "A numerical method for solving the Navier-Stokes equations with application to shock boundary layer interaction", the 13th Aerospace Sciences Meeting, AIAA-7s-1.

- [32] Macrossan M.N., 1989, "The Equilibrium Flux Method for the calculation of flows with non-equilibrium chemical reactions," *J. Comp. Phys.* Vol. 80, Issue 1, pp. 204-231.
- [33] Macrossan M.N., 2001, "A particle only hybrid method for near continuum flows," in: Proceedings of 22nd International Symposium on Rarefied Gas Dynamics, Vol. 585, pp. 426.
- [34] Majda A., 1984, "Compressible fluid flow and systems of conservation laws in several space variables," Springer-Verlag, New York.
- [35] Pullin D.I., 1980, "Direct simulation methods for compressible inviscid ideal gas flow," *J. Comp. Phys.* Vol. 34, pp. 231-244.
- [36] Salichs S. Serna, 2005, High Order Accurate Shock Capturing Schemes for Hyperbolic Conservation Laws based on a new Class of Limiters, Ph.D. Thesis, Doctoral Theses in Applied Mathematics, Universitat de Valencia.
- [37] Schulz-Rinne C.W., Collins J.P., and H.M. Glaz, 1993, "Numerical Solution of the Riemann problem for two-dimensional gas dynamics," *SIAM J. Sci. Compt.*, Vol. 14, pp. 1394–1414.
- [38] Serna S., 2006, "A class of extended limiters applied to piecewise hyperbolic methods," *SIAM J. Sci. Compt.*, Vol. 28, pp. 123–140.
- [39] Shu C.-W., Osher S., 1988, "Efficient implementation of essentially non-oscillatory shock-capturing schemes," *J. Comp. Phys.*, Vol. 77, pp. 439–471.
- [40] Skews B.W., 1967, "The perturbed region behind a diffracting shock wave." *J. Fluid Mech.*, Vol. 29, Issue 4, pp.705–719.
- [41] Smith M.R., 2003, "Hybrid methods in near-continuum flows," M.Phil. Thesis, University of Queensland, Australia.

- [42] Smith M.R., M. N. Macrossan, M. M. Abdel-Jawad, 2008, "Effects of direction decoupling in flux calculation in finite volume solvers," *J. Comp. Phys.* Vol. 227, pp. 4142-4161.
- [43] Smith M.R., 2008, "The true direction equilibrium flux method and its application", PhD Thesis, University of Queensland, Australia.
- [44] Smith M.R., H.M. Cave , J.-S. Wu , M.C. Jermy , Y.-S. Chen, 2009, "An improved Quiet Direct Simulation method for Eulerian fluids using a second-order scheme," *J. Comp. Phys.* Vol. 228, pp. 2213–2224.
- [45] Smoller, Joel, 1983, "Shock waves and reaction-diffusion equations," Springer-Verlag, New York.
- [46] Sun M. and K. Takayama., 1997, "The formation of a secondary shock wave behind a shock wave diffracting at a convex corner." *Shock Waves*, Vol. 7, pp. 287–295.
- [47] Takayama K. and O. Inoue., 1991, "Shock wave diffraction over a 90 degree sharp corner." *Shock Waves*, Vol. 1, pp. 301–312.
- [48] Teshima K. and M. Usami, 2001, "DSMC simulation of axisymmetric supersonic free jets," *Comp. Fluid Dyne. J.*, Vol. 10, pp. 525-530.
- [49] Toro E.F., 1999, *Riemann Solvers and Numerical Methods for Fluid Dynamics*, second ed., Springer, Berlin, Germany.
- [50] Toro E. F., 1991, "A linearized Riemann solver for the time-dependent Euler equations of gas dynamics," *Proc. Roy. Soc. London Ser. A*, 434, pp. 683-693.
- [51] Toro E. F., 2009, "Riemann solvers and numerical methods for fluid dynamics: a practical introduction." Springer-Verlag, New York.

- [52] Tutkun, B., Edis, F., O., 2010, "A GPU Application for High-Order Compact Finite Difference Scheme," 22nd Int. Conference on Parallel CFD 2010, Kaohsiung, Taiwan.
- [53] Van Leer B., 1977, "Towards the ultimate conservative difference scheme III. Upstream-centered finite-difference schemes for ideal compressible flow", *J. Comp. Phys.*, Vol. 23, Issue 3, pp. 263–275.
- [54] Visbal Miguel R., Gaitonde Datta V., 1999, "High-Order Accurate Methods for Complex Unsteady Subsonic Flows," *AIAA Journal*, Vol. 37, pp. 10.
- [55] Wagner W., 1992, "A convergence proof for Bird's direct simulation Monte Carlo method for the Boltzmann equation," *J. Stat. Phys.*, Vol. 66, pp. 1011-1044.
- [56] Woodward P., Colella P., 1984, "The numerical simulation of two-dimensional fluid flow with strong shock," *J. Comp. Phys.*, Vol. 54, pp.115.
- [57] Wu M.G., 2003, "Study on hybrid EPSM/EPSM method for chemical reacting flow," *Chin. J. Comp. Phys.*, Vol. 20, Issue 3, pp. 564.

Appendix A

Flow Structures of the Shock Wave Diffraction

Keats [Keats *et al.*, 2004] describes the theory of the shock wave diffraction that including experimental and computational result from Skews [1967], and summarized the secondary physical phenomena in the perturbed region behind the shock wave. Skews performed experiments for a variety of Mach numbers and convex corner angles, and has outline the structure of the perturbed region; the structure is shown in Figure 3-

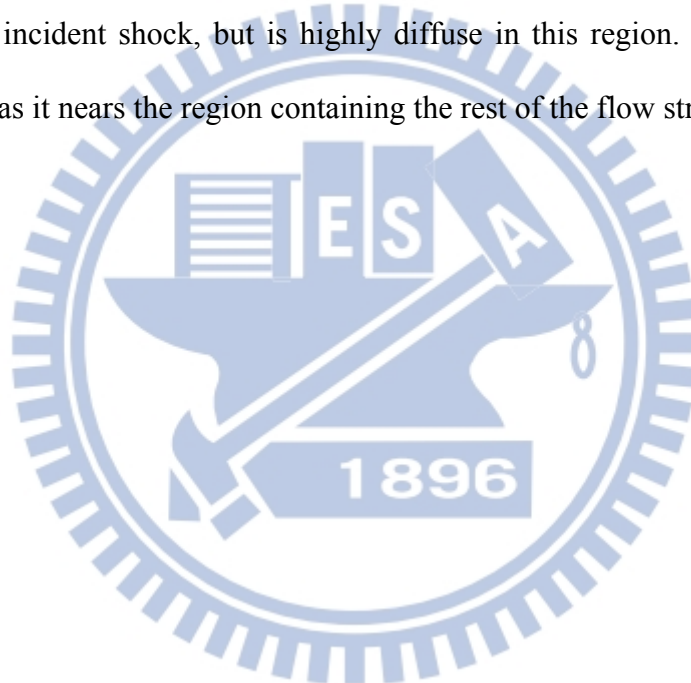
5.1. Skews determined experimentally and tabulated the following correlations:

- The slipstream angle variation with the shock Mach number M_s .
- The terminator angle variation with M_s .
- The relationship between M_s and the velocity of the secondary shock.
- The contact surface velocity variation with M_s .
- The variation of the vortex angle and velocity with M_s .

The flow structures can be described as follows:

- Incident shock: Diffracts in a similar way to a sound wave: its radius of curvature is approximately Wt .
- Reflected sound wave: Propagates upstream and marks the start of the curvature of the incident shock.
- Slipstream: Due to separation, it separates high-velocity gas on the upper side from almost stationary gas on the lower side. It represents the outermost characteristic of the Prandtl-Meyer expansion fan.

- Terminator: The first characteristic of the Prandtl-Meyer expansion; the angle separating the terminator from the horizontal increases with rising M_s .
- Second shock: The region between the slipstream and the terminator is a uniform flow region parallel to the slipstream, and the second shock is a normal shock caused when the flow in this region exceed Mach 1.0 [Sun *et al.*, 1997].
- Vortex: Located just below the slipstream, its location is well defined for $M_s \leq 1.5$. The angle between the vortex and the slipstream decreases as M_s increases.
- Contact surface: Originates at the intersection point of the reflected sound wave and the incident shock, but is highly diffuse in this region. It becomes better-defined as it nears the region containing the rest of the flow structures.



Tables

Table 2-1 The value of weight and abscissas for the Gaussian quadrature.

Number of QDS particles	Weight (w_i)	Abscissas (q_i)
2	$\pm \frac{1}{2} \sqrt{2}$	$\frac{1}{2} \sqrt{\pi}$
3	0 $\pm \frac{1}{2} \sqrt{6}$	$\frac{2}{3} \sqrt{\pi}$ $\frac{1}{6} \sqrt{\pi}$
4	$\pm \frac{1}{2} \sqrt{\frac{3-\sqrt{6}}{2}}$ $\pm \frac{1}{2} \sqrt{\frac{3+\sqrt{6}}{2}}$	$\frac{\sqrt{\pi}}{4(3-\sqrt{6})}$ $\frac{\sqrt{\pi}}{4(3+\sqrt{6})}$

Table 3-1 Comparison of computational expenses for QDS schemes using $2N$ and N^2 dimensional reconstruction.

Number of cells	QDS solvers	
	$2N$	N^2
300x100	8.41 min	23.15 min
450x150	28.9 min	78.3 min
600x200	68.56 min	183.6 min
1000x500	478.4 min	1282.6 min

Table 3-2 QDS scheme time cost in Euler-4-shocks interaction case.

Number of cells	QDS solvers	
	2N	N ²
1000x1000	13.29 hours	55.6 hours
100x100	45 (s)	189 (s)
200x200	375(s)	1520 (s)
300x300	1307 (s)	5199 (s)

Table 3-3 pre- and post-shock fluid initial conditions.

	Mach number	
	1.5	2.4
ρ_2/ρ_1	1.862	3.212
T_2/T_1	1.32	2.04
U_p	0.8215	1.956

Table 3-4 Parallel Performance for a 2D shock-bubble problem with 2.4 million computational cells.

Number of processors	Computation time (sec.)	Number of cells
1	361.613	20000
4	348.995	80,000
9	428.812	180,000
16	410.294	320,000
25	425.229	500,000
36	444.135	720,000
49	472.599	980,000

Table 3-5 Parallel computation times for shock-bubble problem with 500,000 cells at 2000 time steps in simulation time 0.2.

Number of processors	Computation time (s)	Number of Cells for one processor
1	8220.19	500,000
2	4299.89	250,000
4	2761.14	125,000
8	1210.08	62,500
16	762.245	31,250
25	425.229	20,000
32	347.833	15,625
64	158.845	7,813
80	132.77	6,250
100	106.164	5,000
256	42.9935	1,953

Table 3-6 Parallel computation times for shock-bubble problem with 2 million cells in
2000 time steps.

Number of processors	Computation time (sec.)	Number of cells for one processor
1	29740.59	2,000,000
4	8744.45	500,000
8	4978.56	250,000
16	2890.74	125,000
25	1827.92	80,000
32	1348.79	62,500
64	679.745	31,250
128	340.572	15,625
256	172.599	7,813

Table 3-7 Parallel computation times for shock-bubble problem with 12.5 million cells
in 2000 time steps.

Number of processors	Computation time (sec.)	Number of cells for one processor
1	187130.1	12,500,000
8	27532.8	1,562,500
16	19929.3	781,250
32	8613.3	390,625
64	4463.82	195,313
100	2806.29	125,000
128	2225.91	97,656
256	1115.02	48,828

Figures

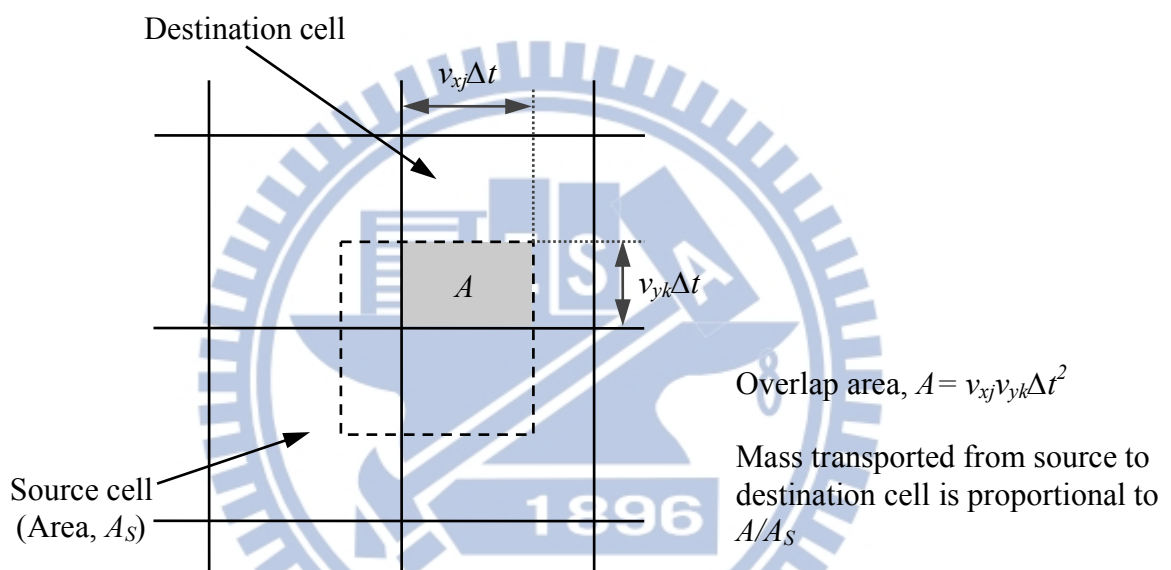


Figure 2-1. Schematic showing the way fluxes of conserved quantities between source and destination cells are calculated using the “overlap” function in QDS [Smith *et al.*,

2009].

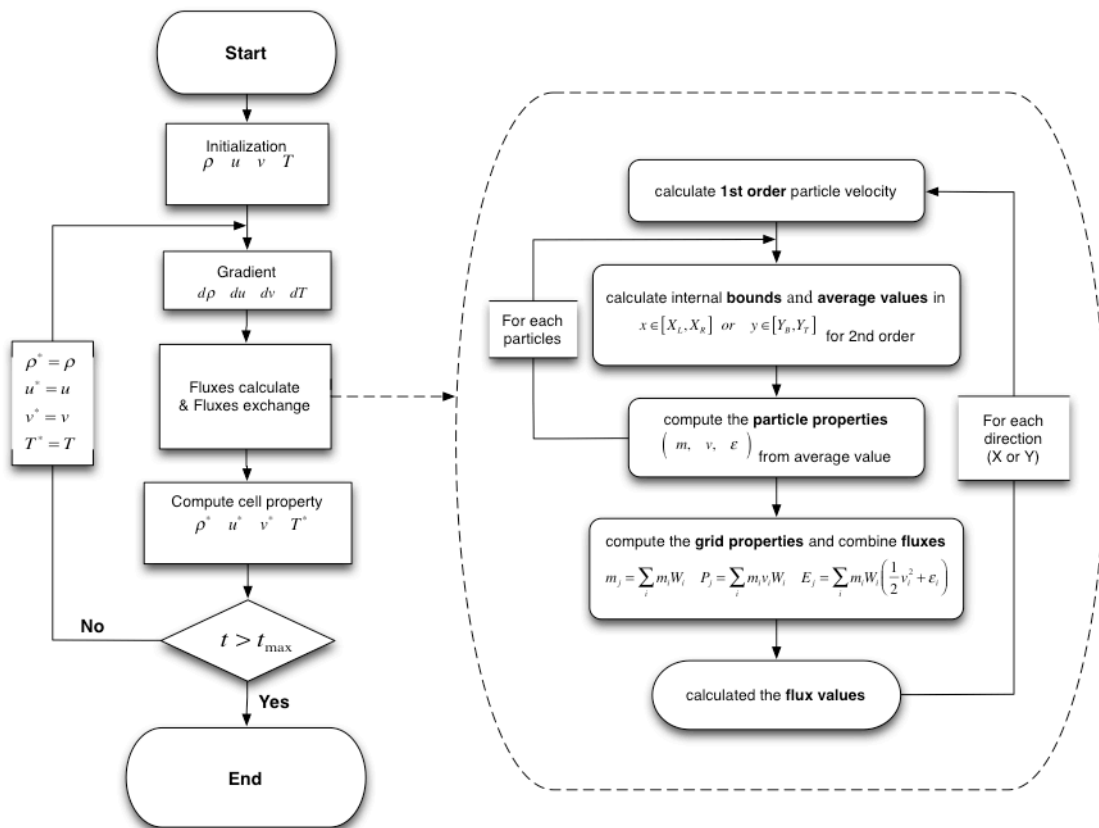


Figure 2-2. Flowchart describing QDS-2N particle computation with gradient inclusion.

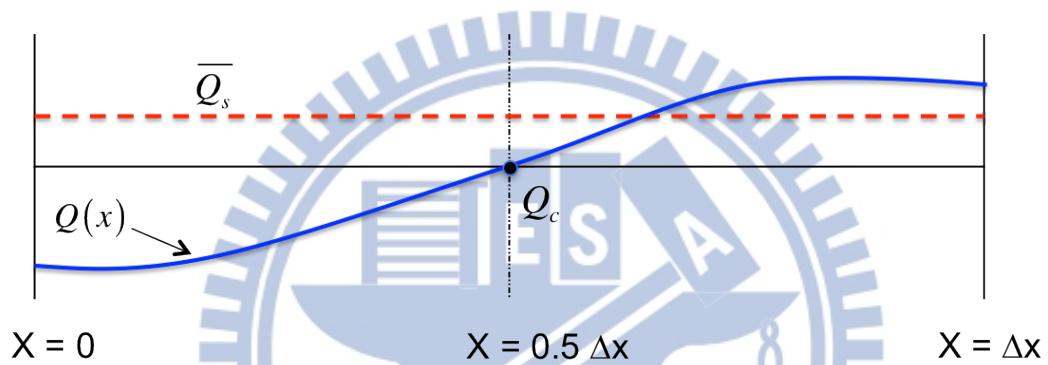


Figure 2-3. The special reconstruction convention for current amount of conserved quantity Q in one cell.

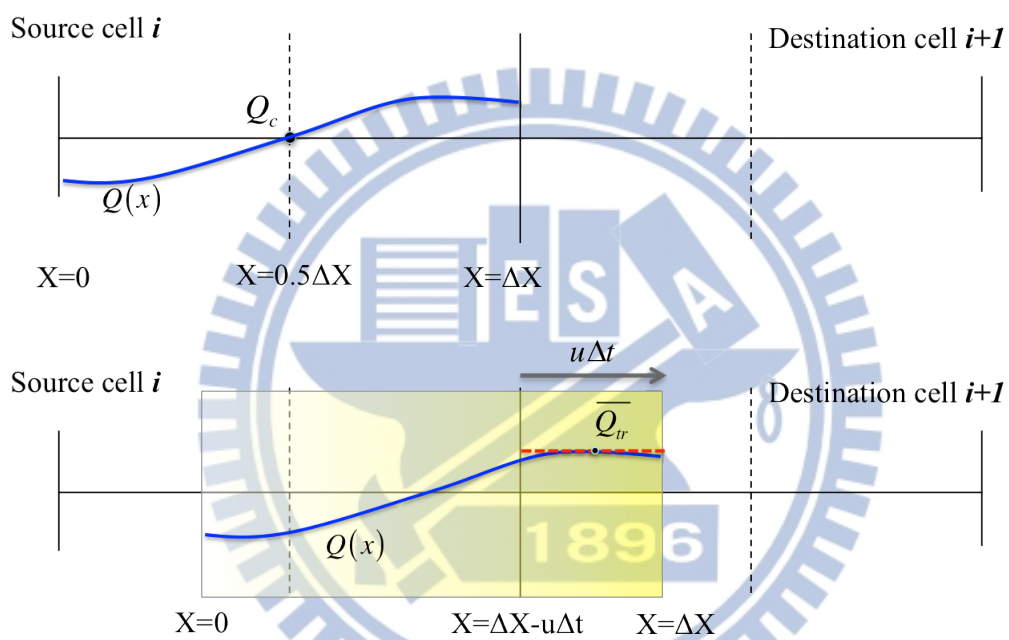


Figure 2-4. QDS flux procedure within a general (arbitrary) spatial reconstruction of conserved quantity Q .

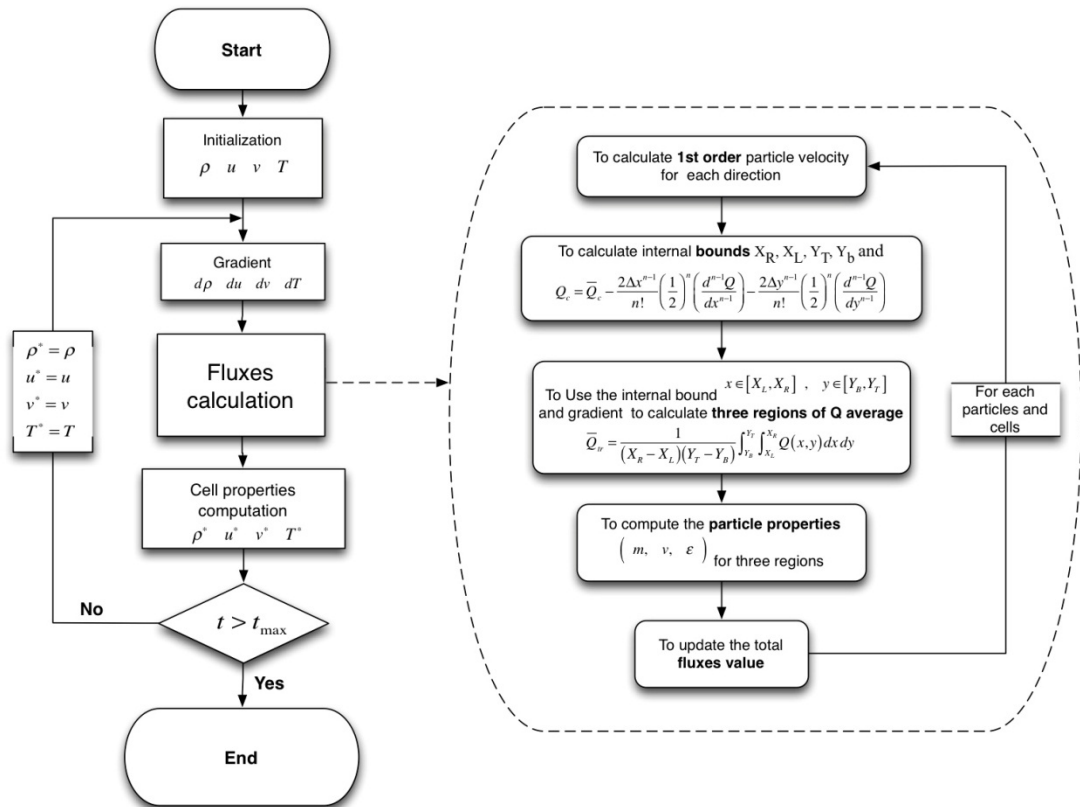


Figure 2-5. Flowchart describing QDS particle computation with gradient inclusion.

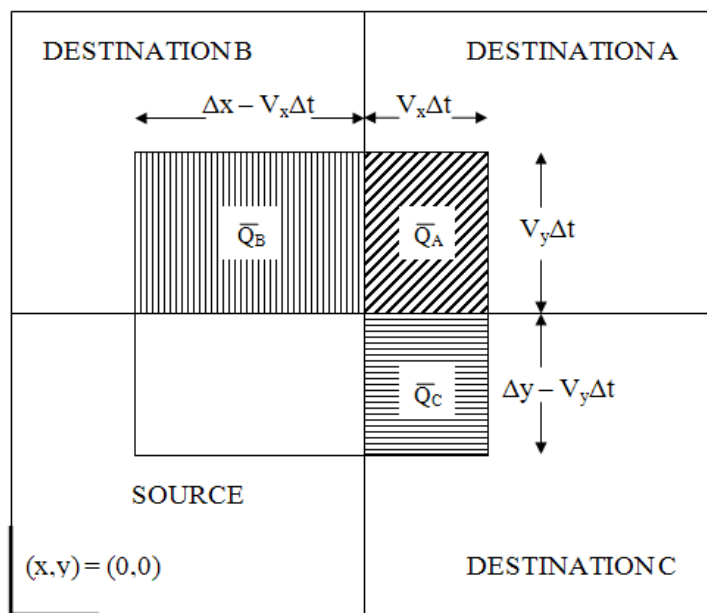


Figure 2-6. Two-dimensional motion of a single QDS particle showing “sub-particle” contributions.

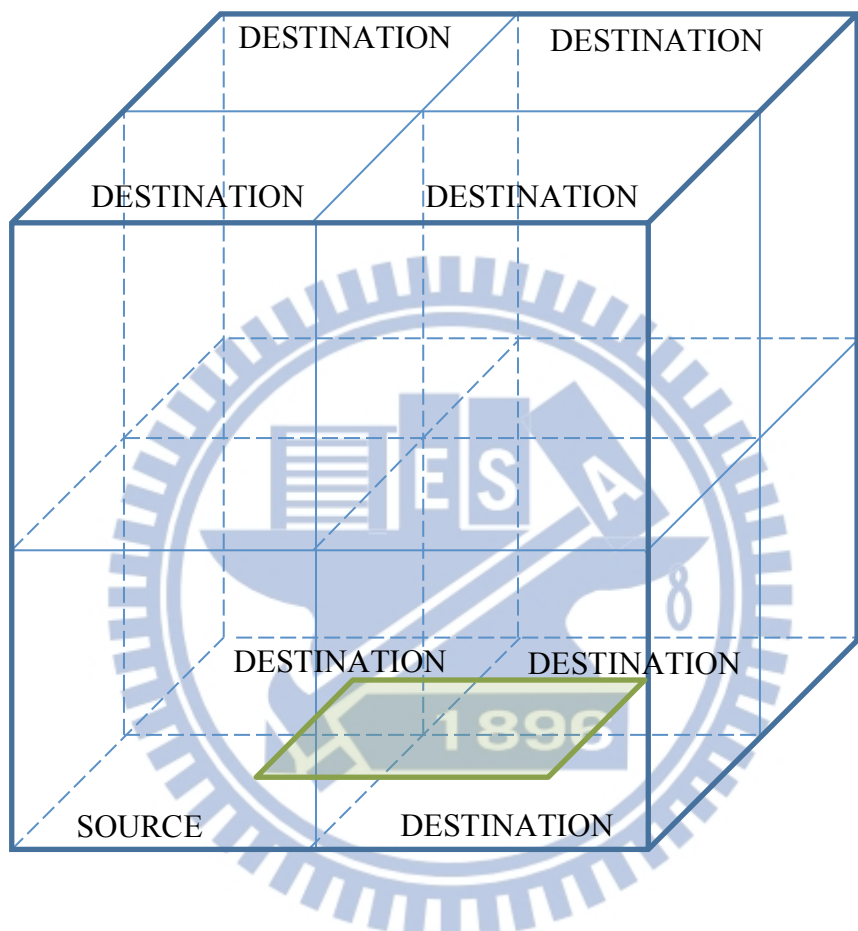


Figure 2-7. Three-dimensional motion of a single QDS particle showing “sub-particle” contributions. The green parallelogram is presented the concept in two-dimensional.

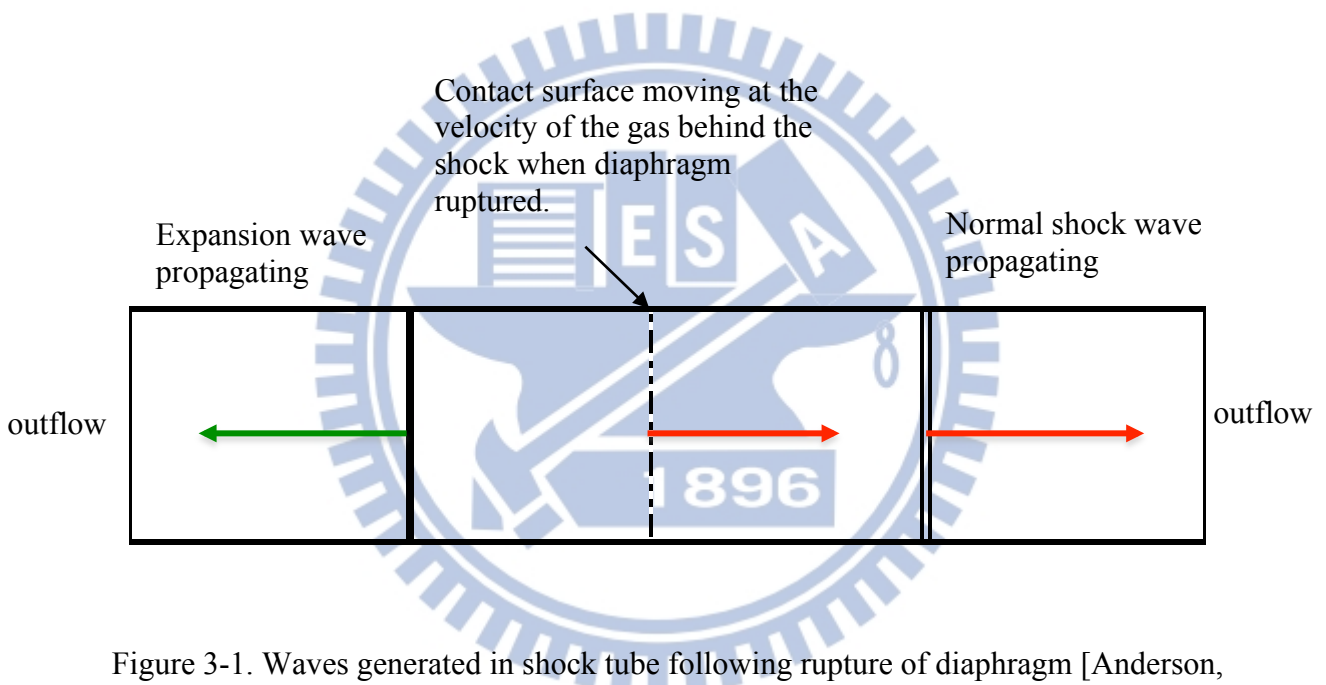


Figure 3-1. Waves generated in shock tube following rupture of diaphragm [Anderson, 1990].

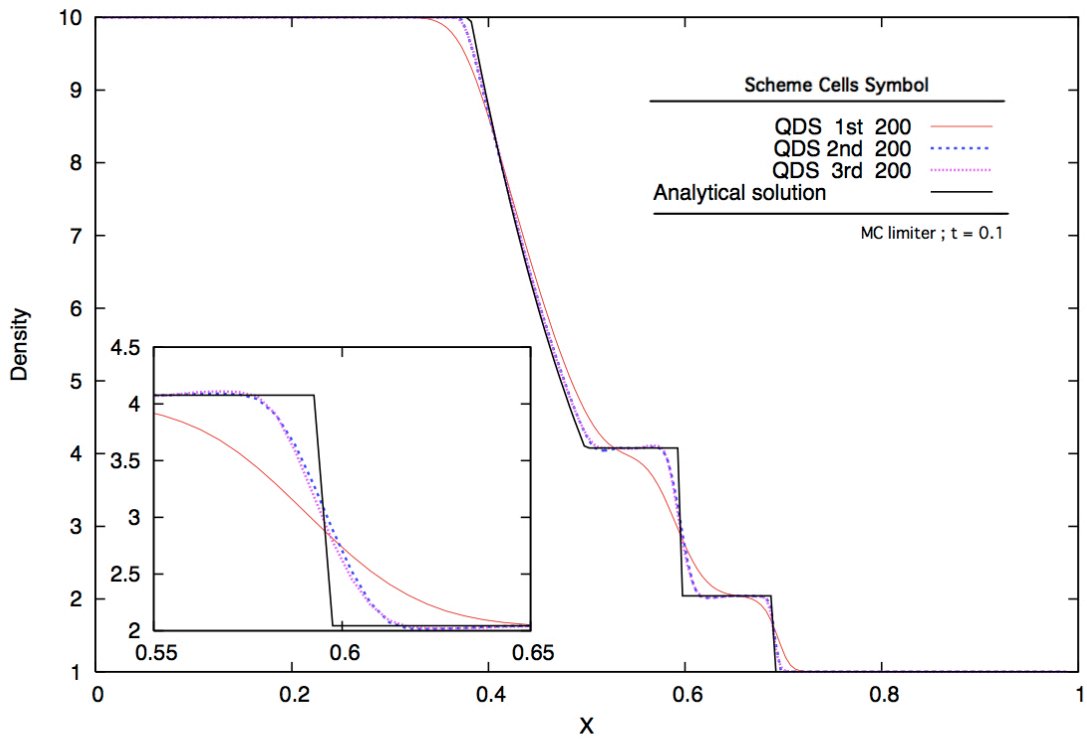


Figure 3-2. The shock tube problem as computed by pre-QDS method with a uniform grid of 200 zones. The results were discussed the difference to the QDS 1st ~3rd method and Riemann solver using MINMOD limiter at time 0.1.

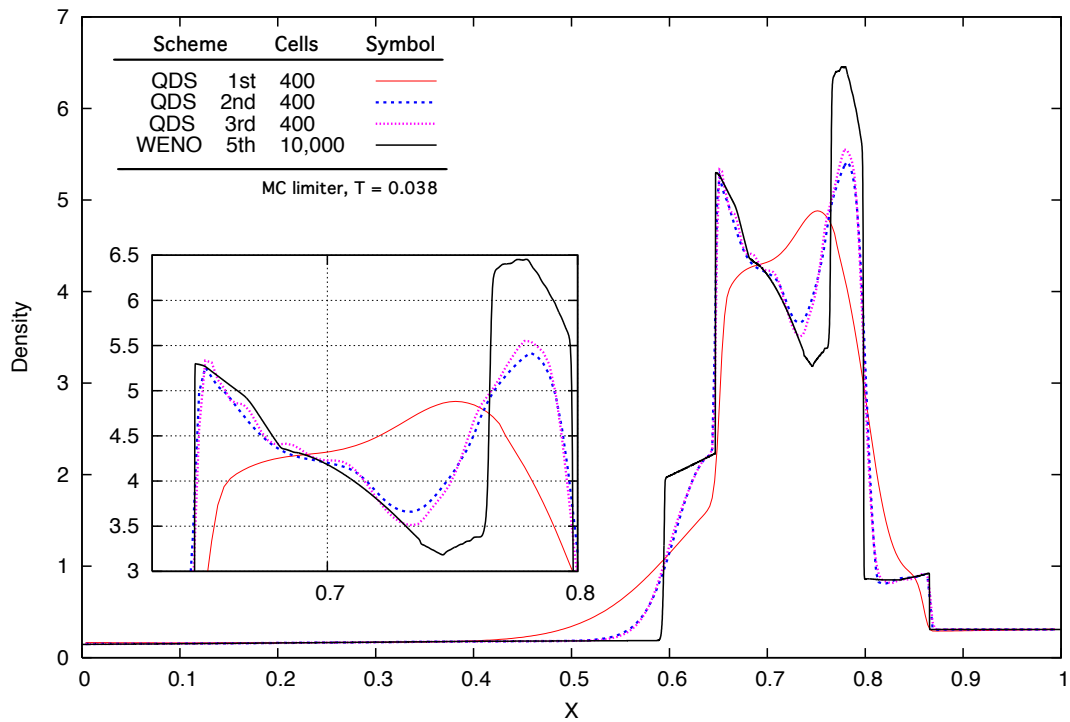


Figure 3-3. The interaction of two blast wave computed by the QDS method with 400 grids at $t = 0.0038$. The solid black line is WENO (fifth order) scheme with 10,000 grids.

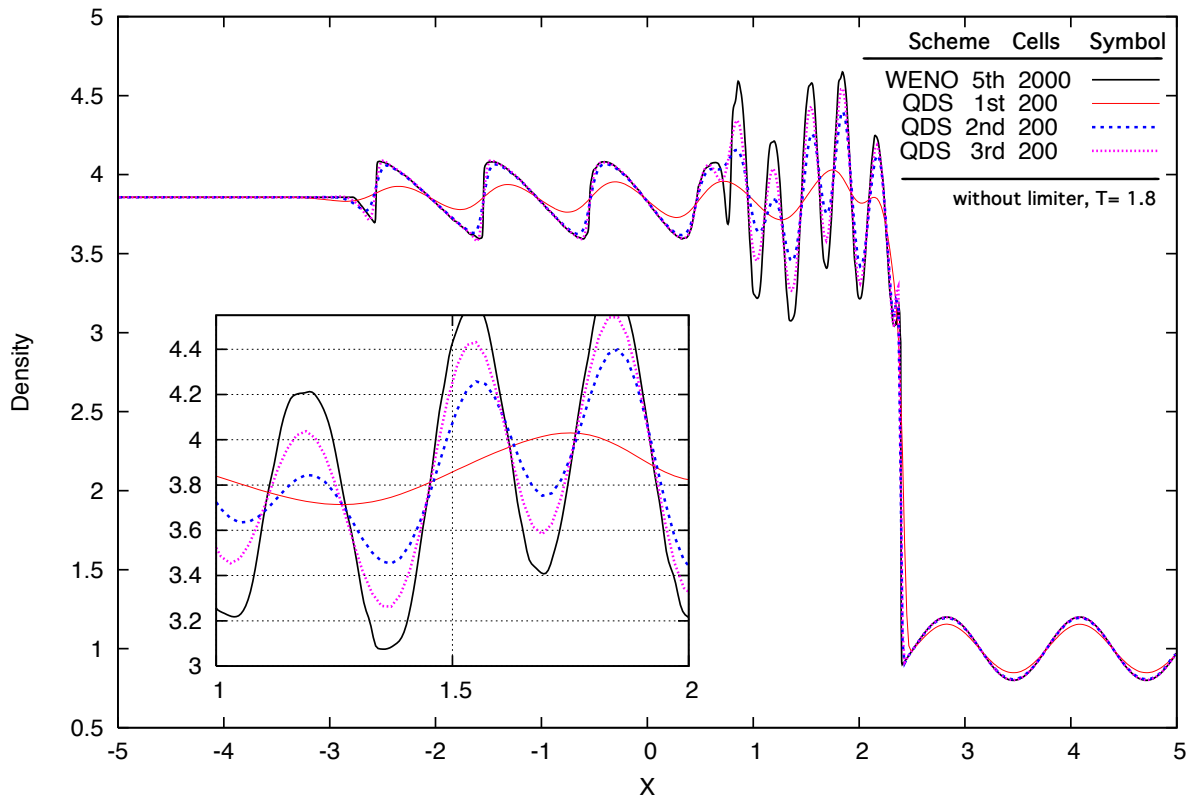


Figure 3-4. Density profile of the shock-acoustic-wave case at $t = 1.8$. The solid black line is WENO-3 (fifth order) with 2000 grids compared with QDS method which without limiter form 1st order to 3rd order.

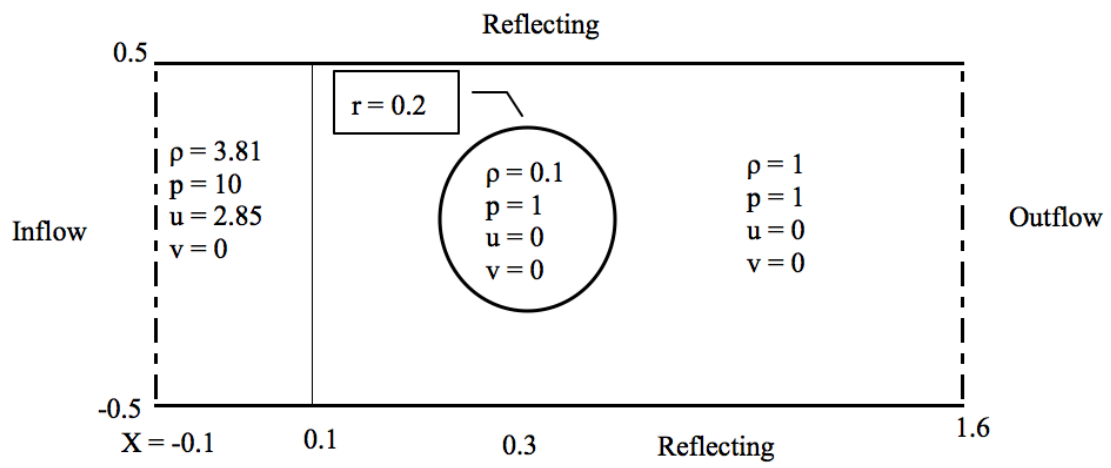


Figure 3-5. The structure of shock bubble interaction.

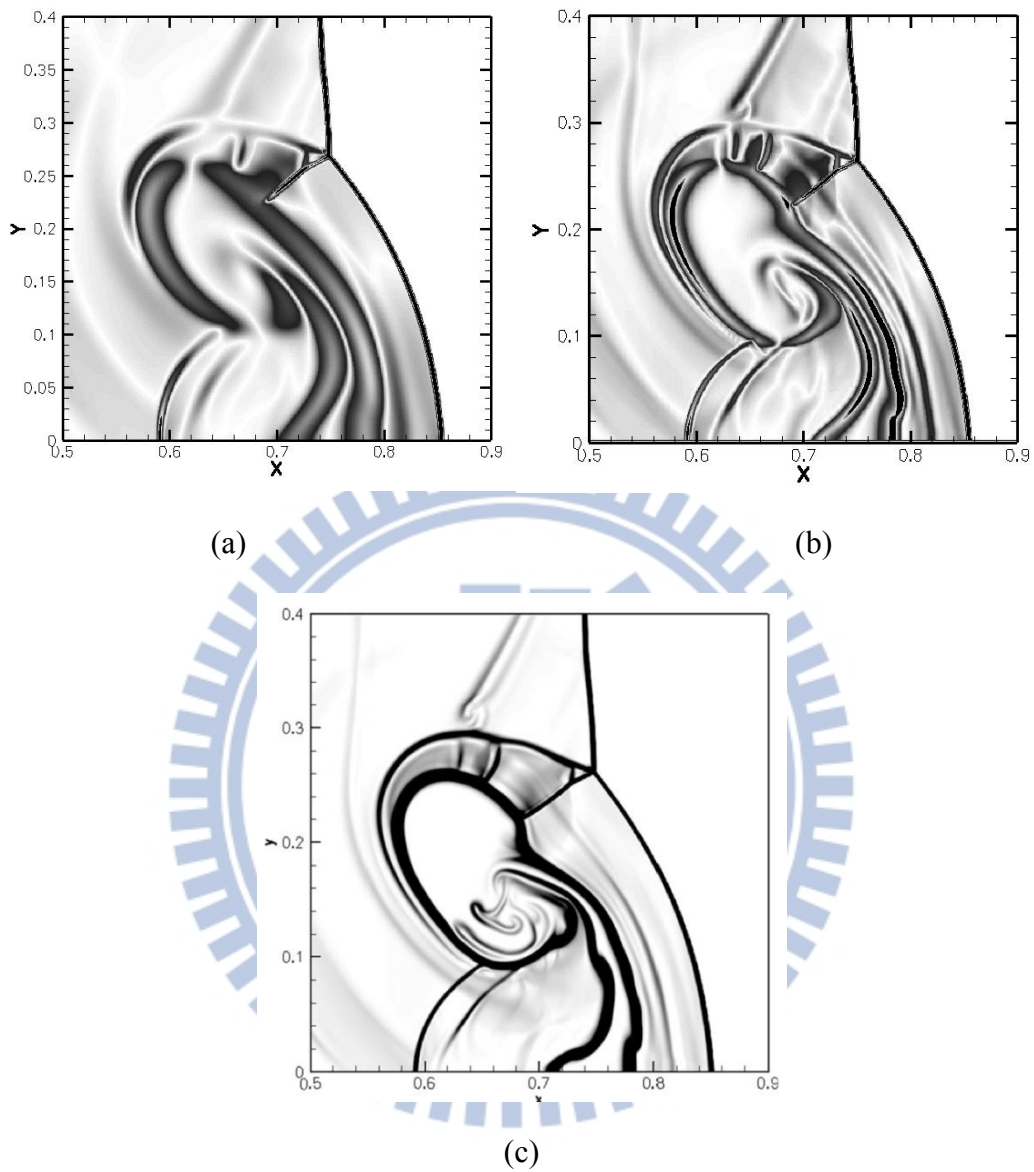


Figure 3-6. Zoom of shock-bubble Schlieren image with 1000×500 cells at time of 0.2. QDS 2nd order (a) 2N method with van Leer's limiter, (b) N^2 method, and (c) 2nd order TVD result presented in [Čada, 2009] using the same resolution.

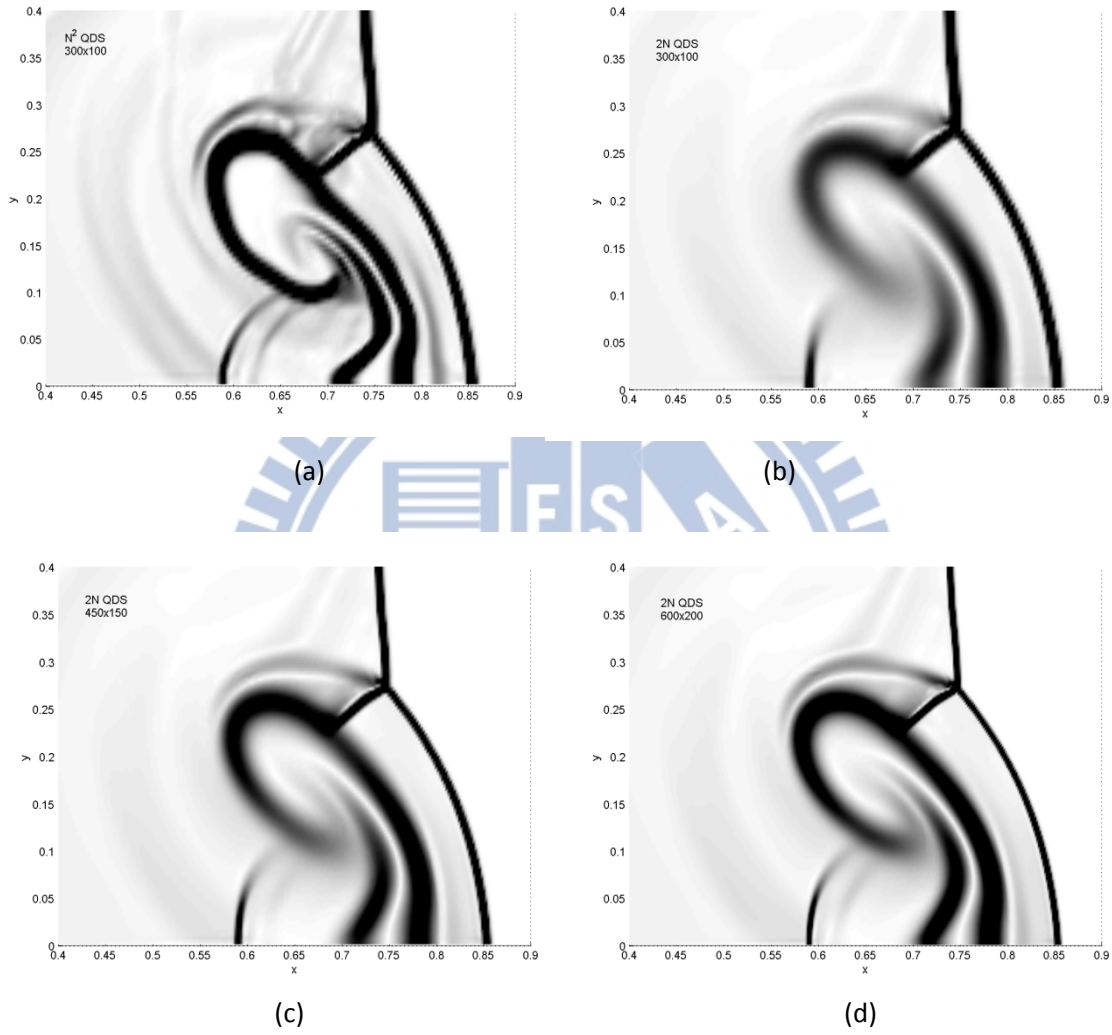


Figure 3-7. Zoom of Schlieren image of shock bubble problem at time of 0.2; (a) QDS- N^2 method with 300×100 cells; (b) QDS-2N method with 300×100 cells; (c) QDS-2N method with 450×150 cells; (d) QDS-2N scheme with 600×200 cells.

(1,1)	
B	A
$\rho = 0.5323, \quad u_x = 1.206$ $p = 0.3, \quad u_y = 0.0$	$\rho = 1.5, u_x = 0$ $p = 1.5, u_y = 0$
(0.75,0.75)	
C	D
$\rho = 0.138, \quad u_x = 1.206$ $p = 0.029, \quad u_y = 1.206$	$\rho = 0.5323,$ $u_x = 0.0,$ $u_y = 1.206,$ $p = 0.3,$
(0,0)	

Figure 3-8. The initial conditions for the first problem of Euler-4 shocks interaction.

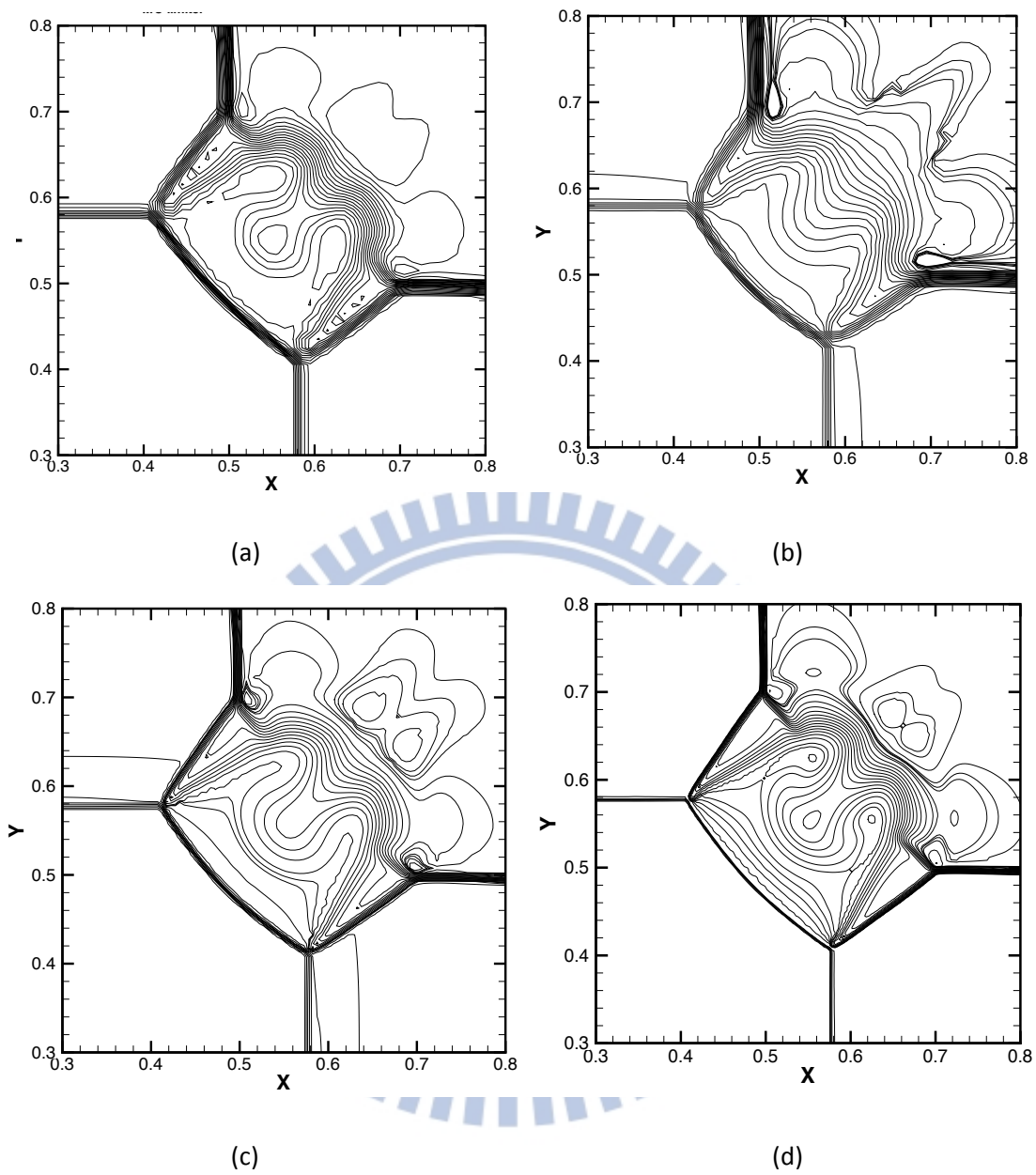


Figure 3-9. Zoom of density contour line of Euler-four-shocks problem. Comparing the second-order QDS- N^2 method (a) using 100×100 grids with MC limiter and 2N method using 100×100 grids (b) and 200×200 grids (c), 300×300 grids (d) with MC limiter at time of 0.4.

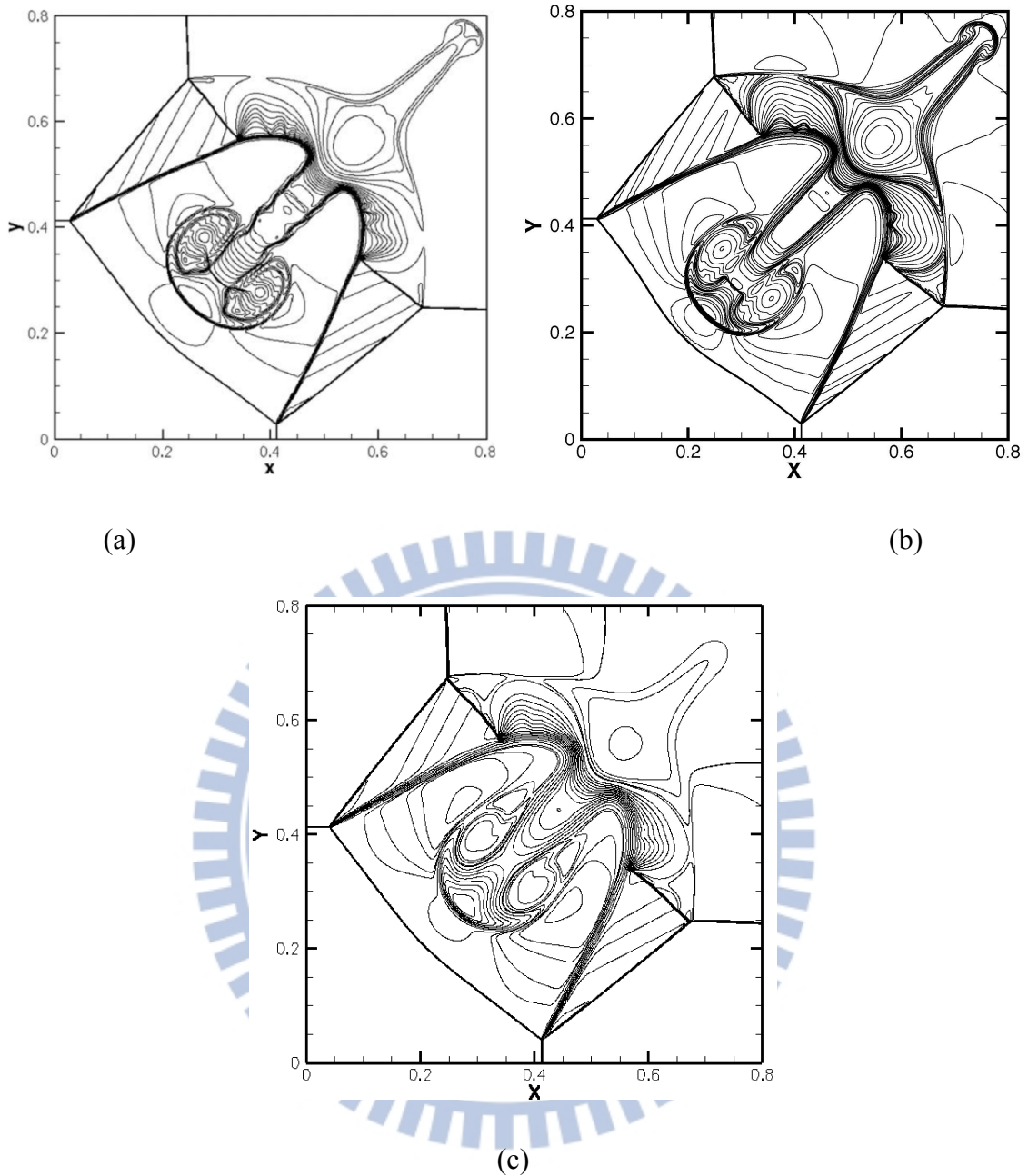


Figure 3-10. Zoom of the density contour lines of Euler four shocks problem. (a) the 2nd order TVD-MUSCL method taken from Čada [Čada *et al.*, 2009] using 1000x1000 points, CFL=0.8. (b) The third-order QDS-N² method used 1000x1000 grids with MC limiter at time of 0.8. (c) The third-order QDS-2N method used 1000x1000 grids with MC limiter.

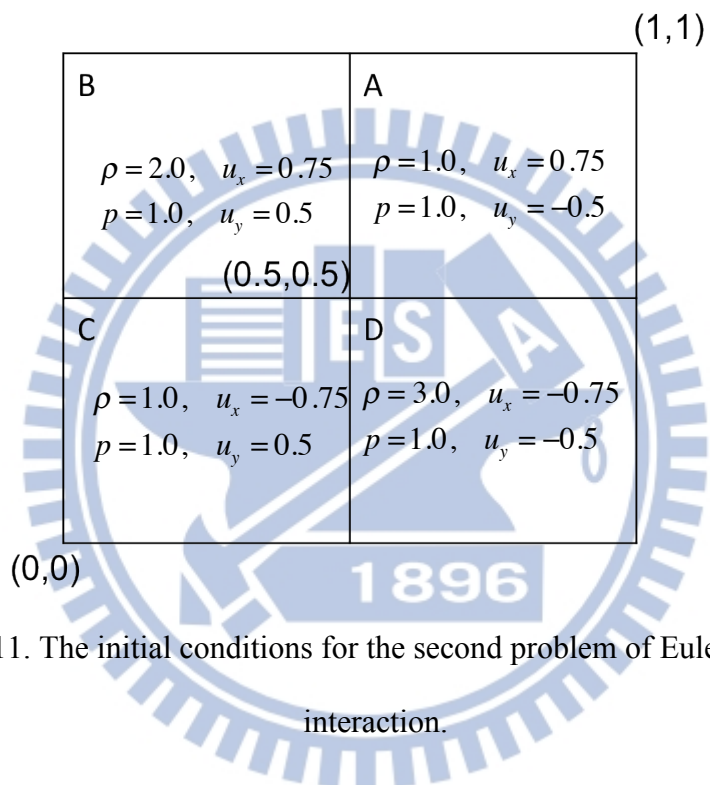


Figure 3-11. The initial conditions for the second problem of Euler-four-shock interaction.

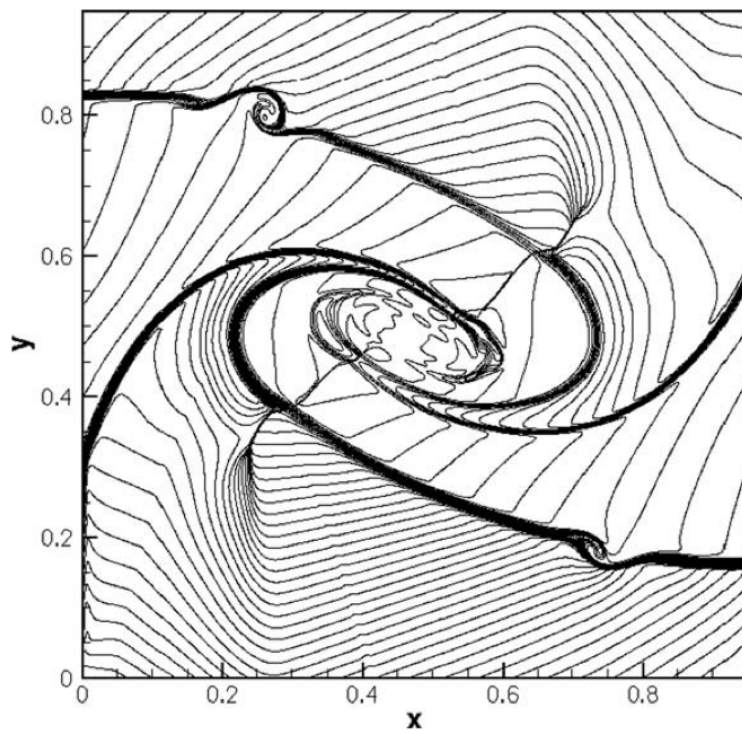
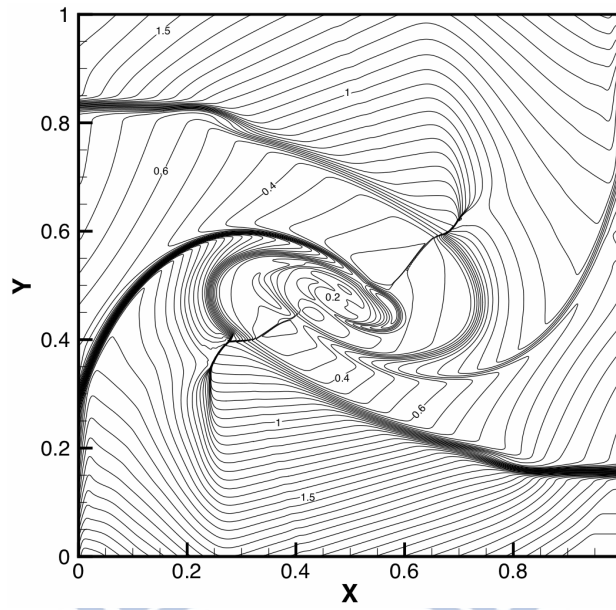
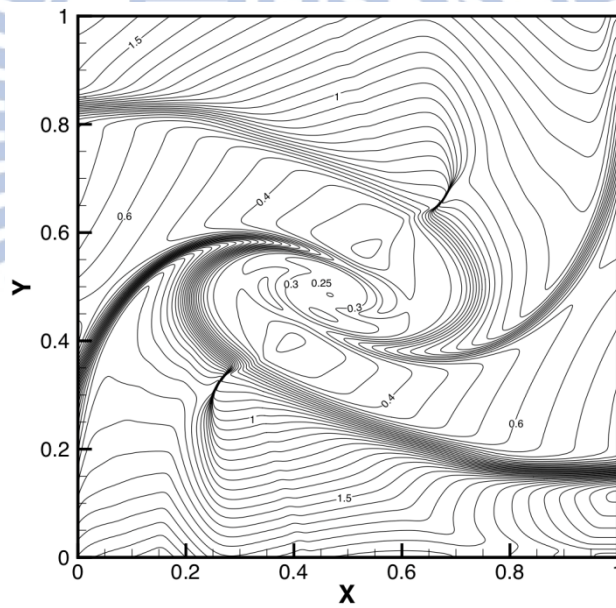


Figure 3-12. Density profile of the four contacts problem for second-order TVD-MUSCL method taken from [Čada *et al.*, 2009].



(a)



(b)

Figure 3-13. Density contour obtained from QDS N^2 solver (a) and 2N solver (b) by using 1000×1000 cells, 2nd order method with MINMOD limiter. The CFL number is 0.5. Level form 0 to 2.4 at 0.05 interval of line.

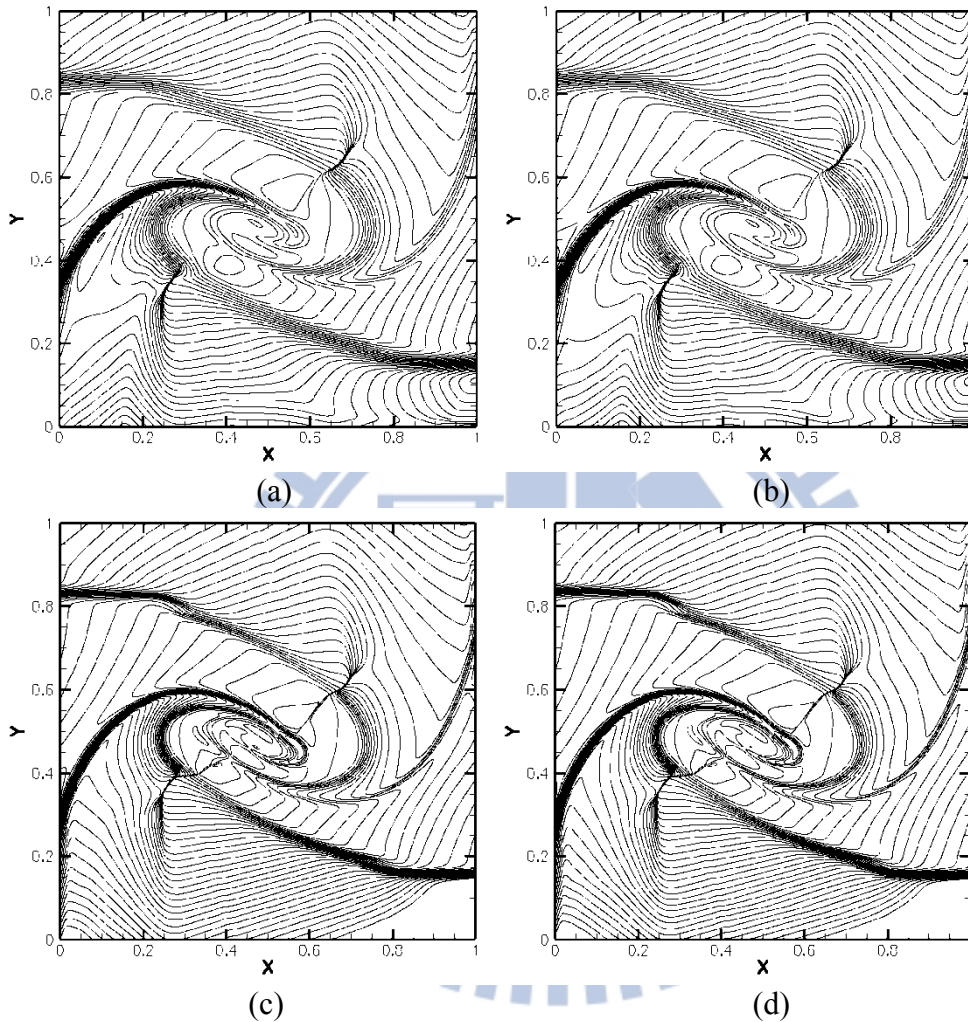
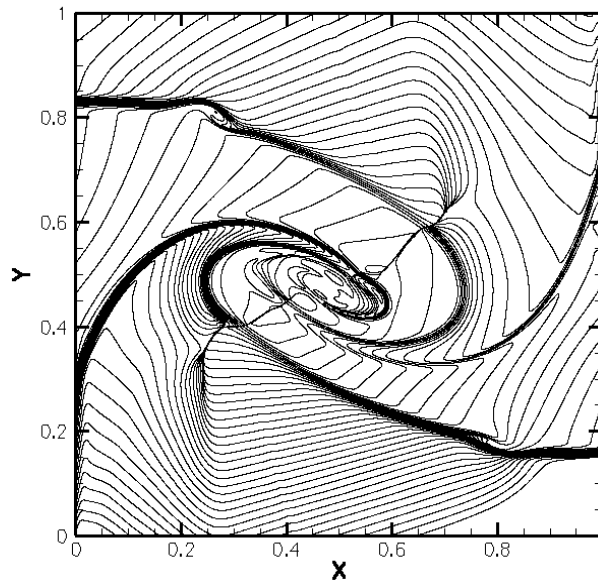
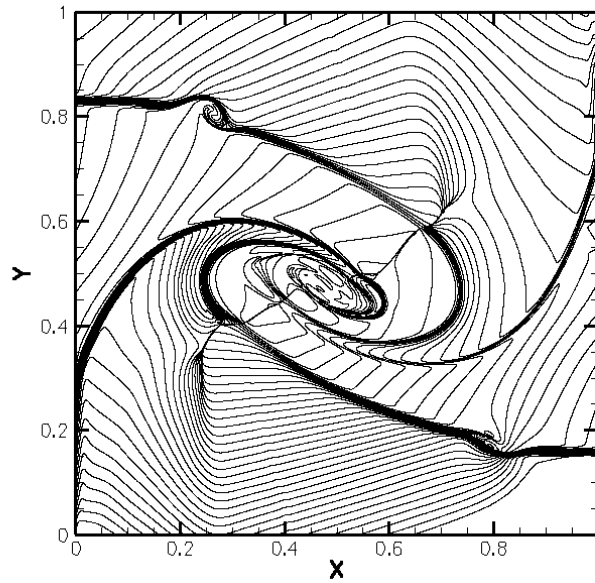


Figure 3-14. Density contour obtained from QDS-2N solver with 5 particles (a) and 9 particles in each direction (b); QDS- N^2 method with 5 particles (c) and 9 particles in each direction (d) by using $1,000 \times 1,000$ cells, 2nd order method with MINMOD limiter at time of 0.8. The CFL number is 0.5. Level form 0 to 2.1 at 0.05 interval of line.



(a)



(b)

Figure 3-15. Density contour obtained from QDS-N² solver using (a) 2,000×2,000 and (b) 3,000×3,000 cells, 2nd order method with MINMOD limiter at time of 0.8. The CFL number is 0.5. Level form 0 to 2.1 at 0.05 interval of line.

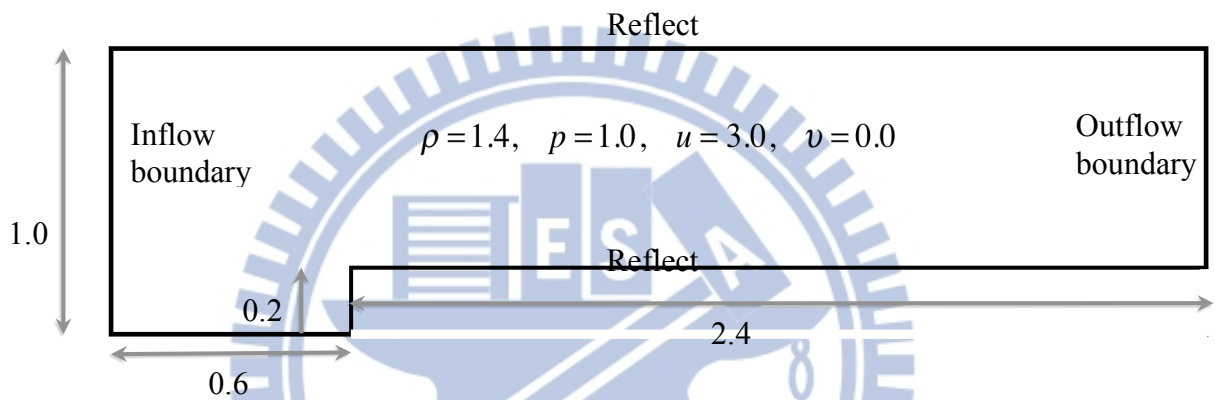


Figure 3-16. Geometry and boundary conditions for the Mach 3 flow over a forward facing step in a wind tunnel. All boundaries with exceptions to the inflow and outflow are secularly reflective. The outflow boundary is calculated through interpolation of states of interior cells.

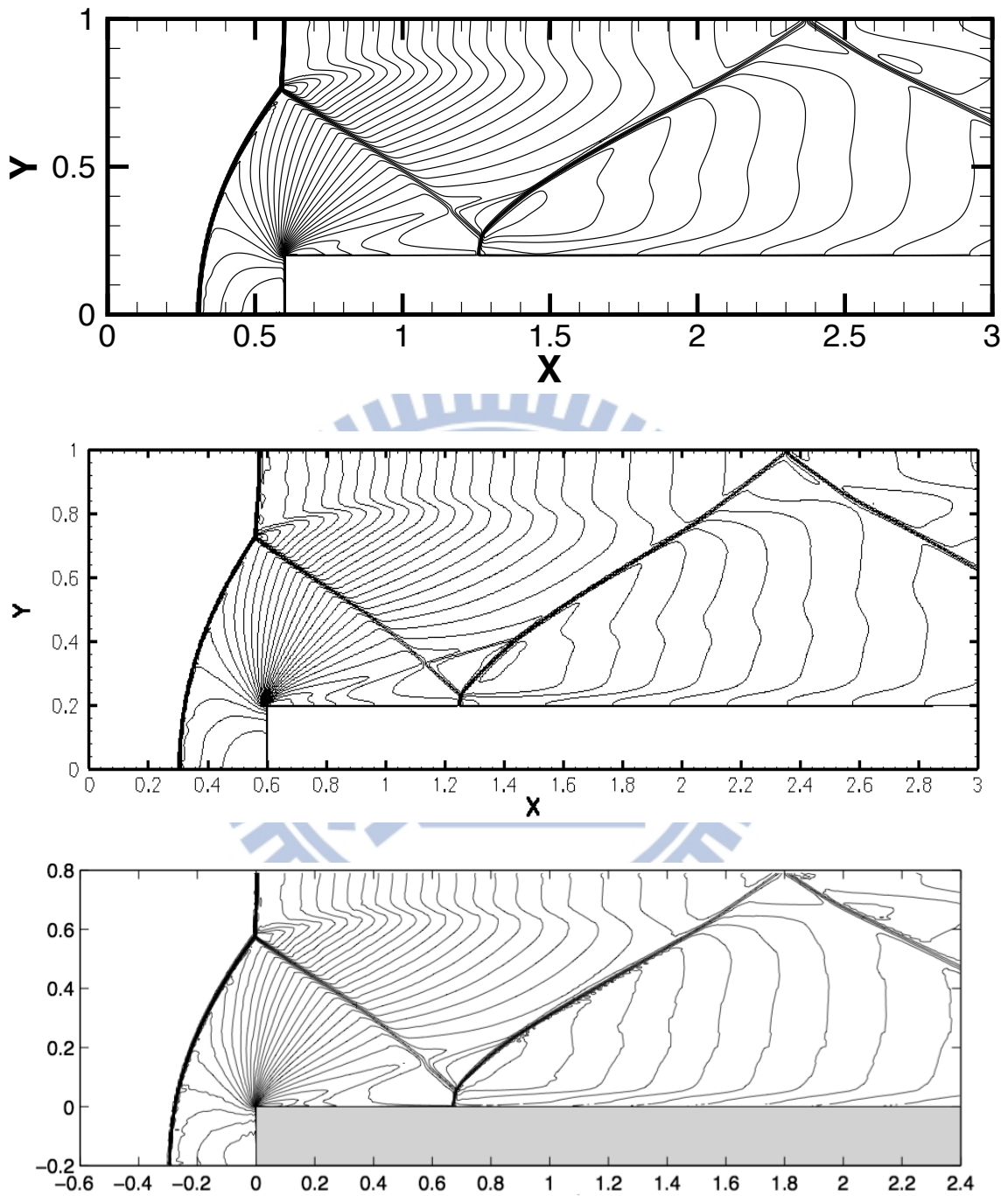


Figure 3-17. Contour of density at 4.0s for Mach 3 flow over a forward facing step in a wind tunnel. Compare the 2nd order QDS-2N method (top) and QDS-N² method (middle) for 600×200 grids. (bottom) The result of Keats and Lien [Keats *et al.*, 2004]

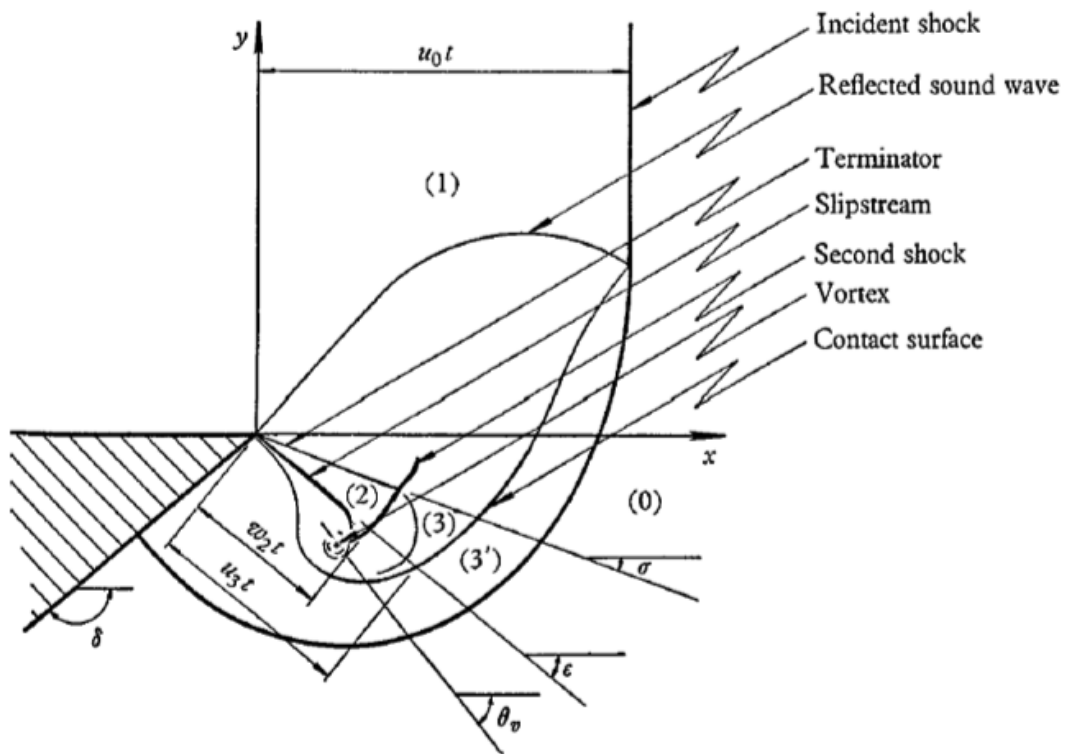


Figure 3-18. Structure of the perturbed region behind a diffracting shock wave, defined by from Skews [1967].

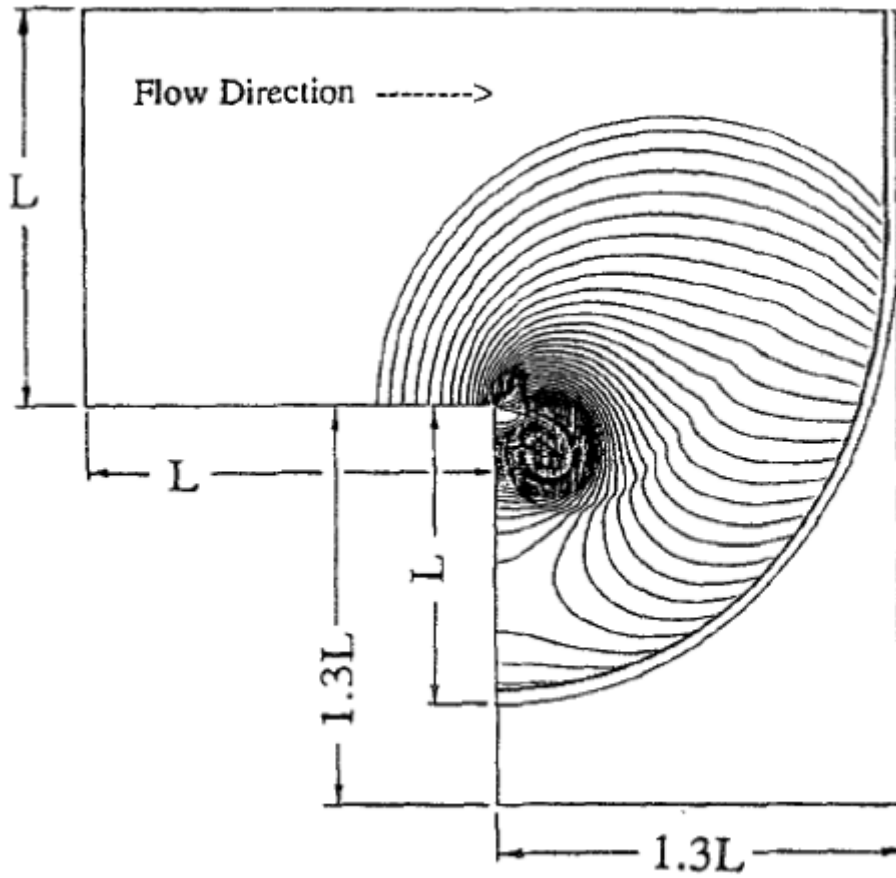


Figure 3-19. The output for compulsory figure for shock wave diffraction (by Takayama [1991]).

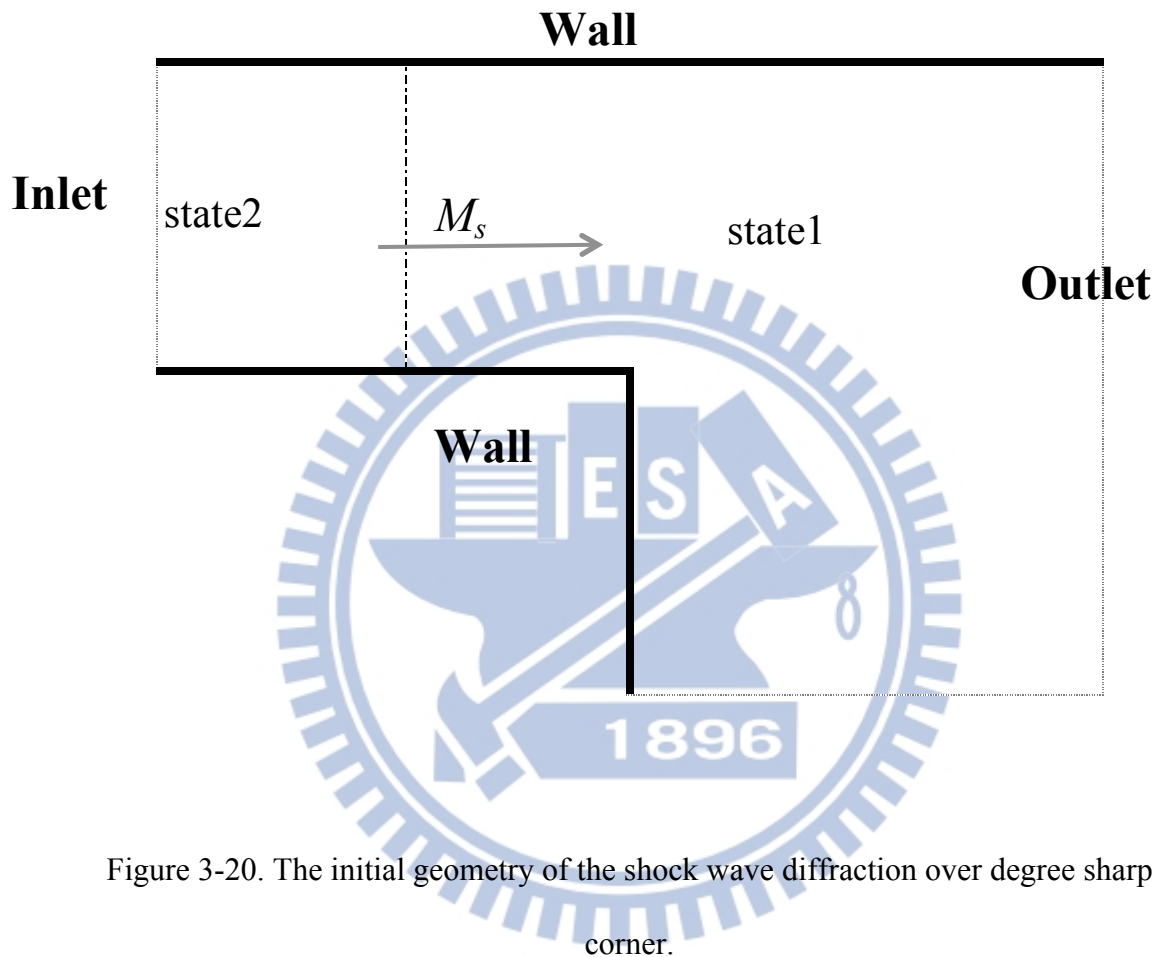


Figure 3-20. The initial geometry of the shock wave diffraction over degree sharp corner.

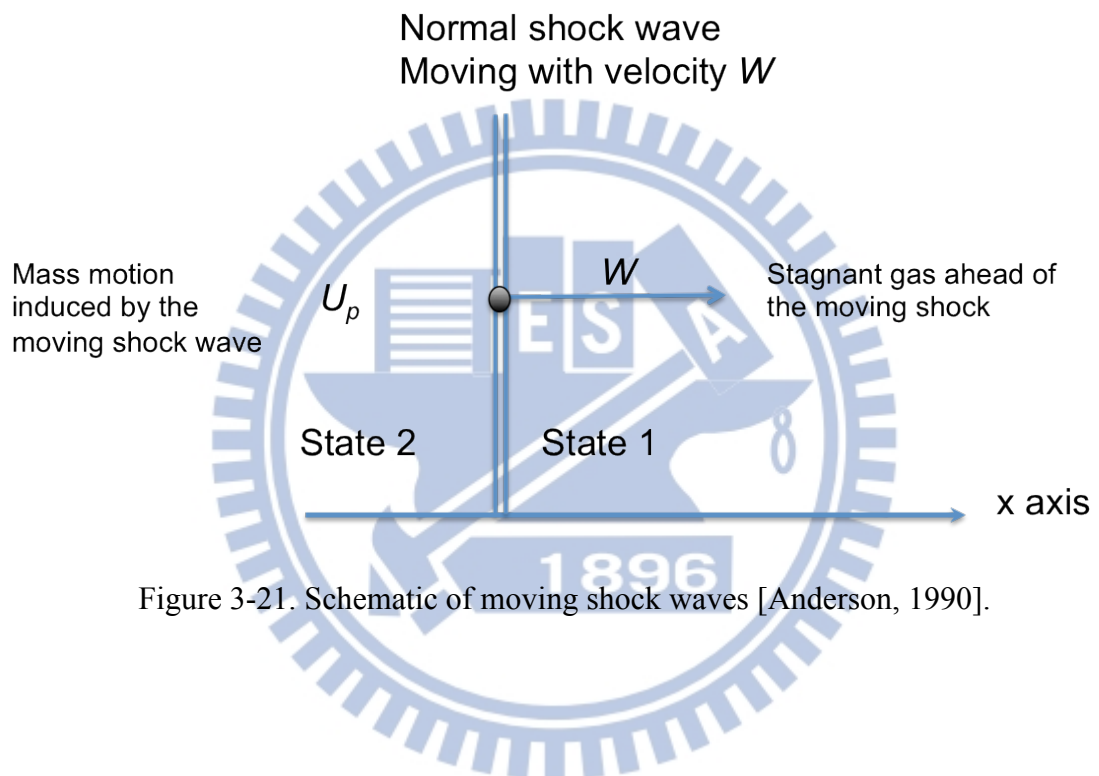
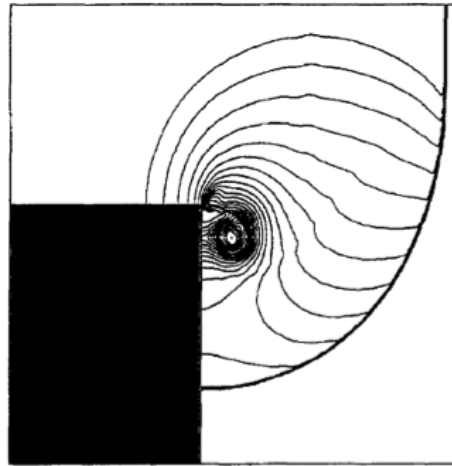


Figure 3-21. Schematic of moving shock waves [Anderson, 1990].



(a)

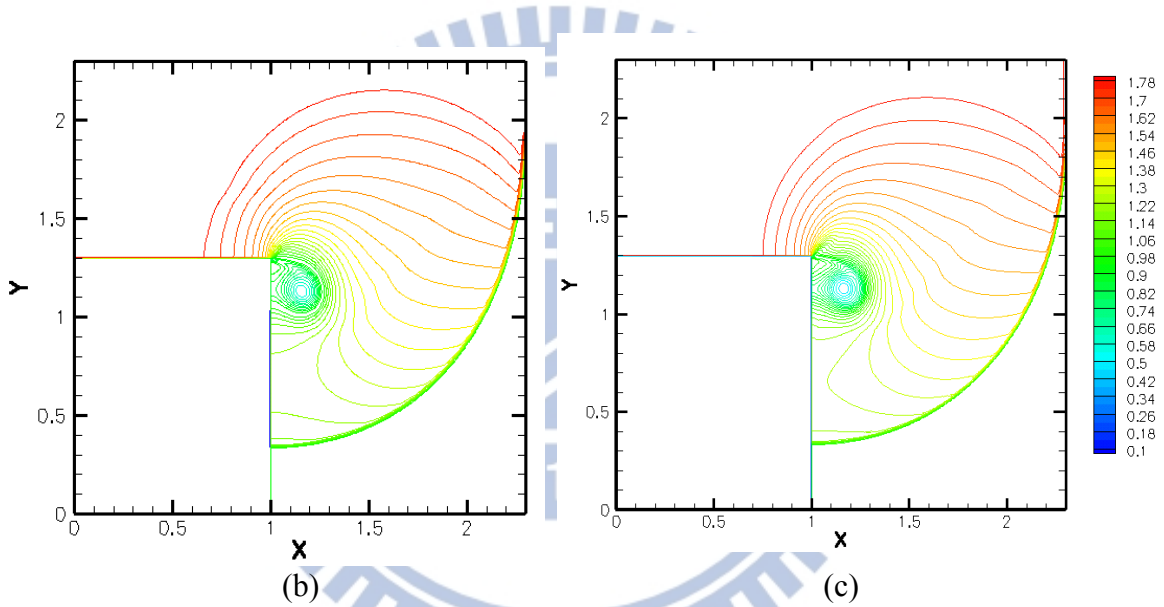
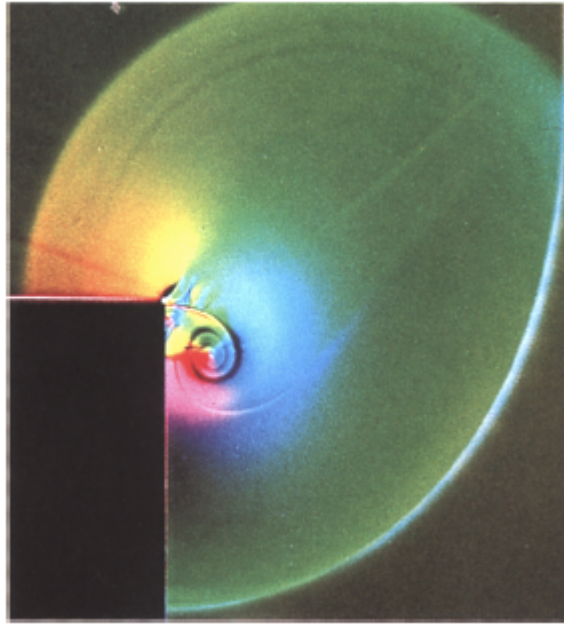
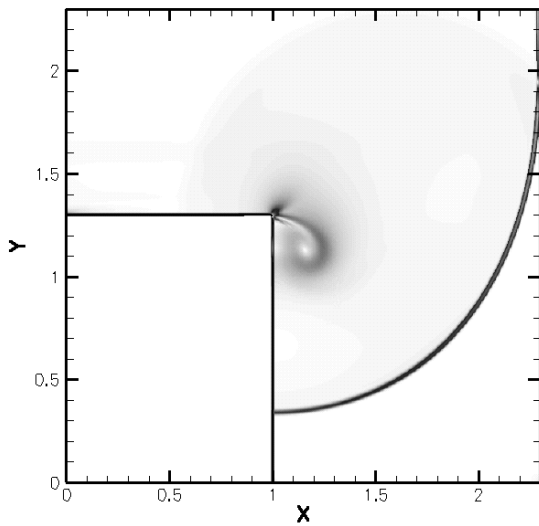


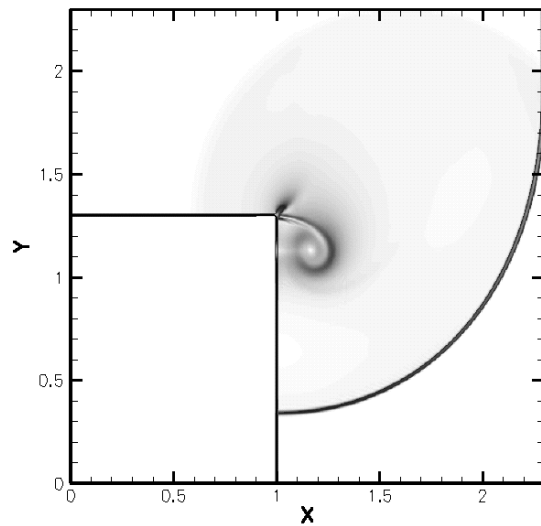
Figure 3-22. The density contours of the shock wave diffracting over 90 degree sharp corner with 400×400 grid, $M_s=1.5$. (a) the second-order TVD extension of Godunov method [Takayama *et al.*, 1991]. (b) the second-order QDS-2N method and (c) the second-order QDS- N^2 method with MC limiter, CFL=0.5.



(a)

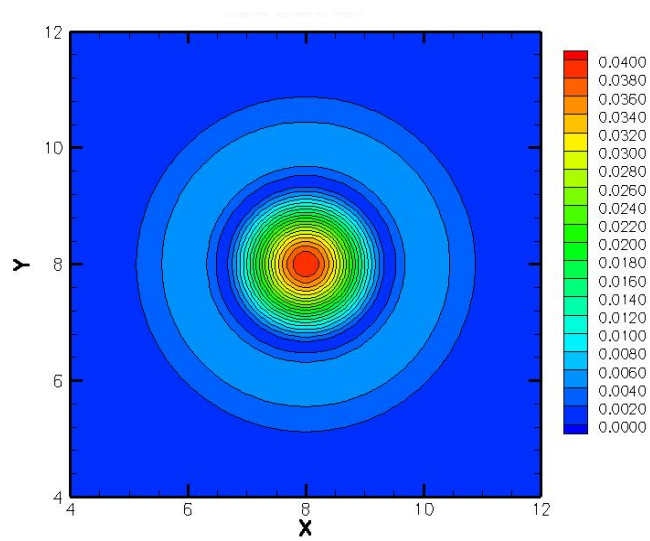


(b)

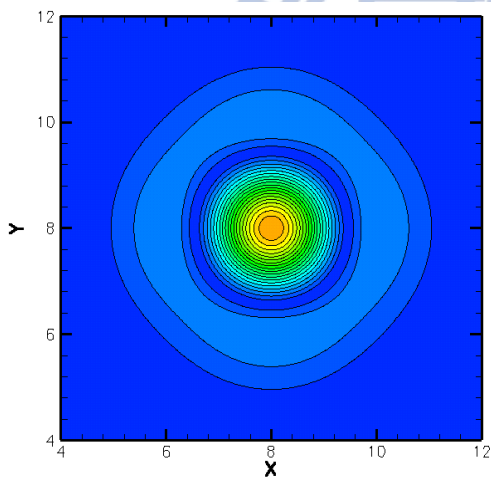


(c)

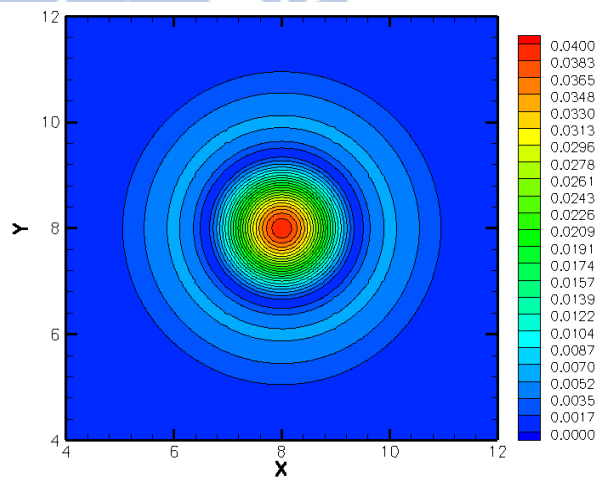
Figure 3-23. Schlieren image of the shock wave diffracting over a 90 degree sharp corner, $M_s=1.5$. (a) the experimental result made form Ritzerfeld *et al.* [Takayama *et al.*, 1991]. (b) second-order QDS-2N method and (c) QDS- N^2 method with 400×400 cells, MC limiter, CFL=0.5.



(a)



(b)



(c)

Figure 3-24. Vorticity magnitude contours compared (a) exact solution and two result using 2nd order (b) QDS 2N method and (c) QDS N² in 800×800 uniform cells. All results are taken the CFL number to 0.1.

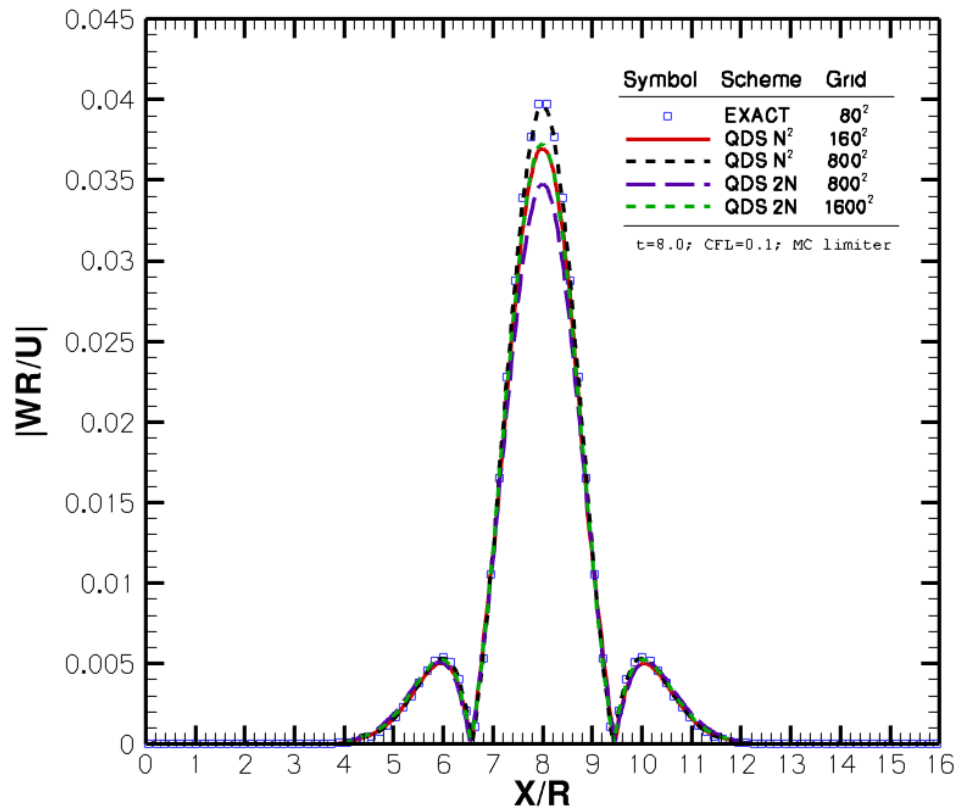


Figure 3-25. The vorticity profiles along the central line passing through the vortex. The comparison contained the exact solution (blue square-symbol line), the QDS- N^2 method using 160×160 cells (red line), 800×800 cells (black dash-dot line), and 2N method using 800×800 cells (purple long-dash line), 1600×1600 cells (green dotted line). Two methods are computed in MC limiter and CFL=0.1 at time 8.0.

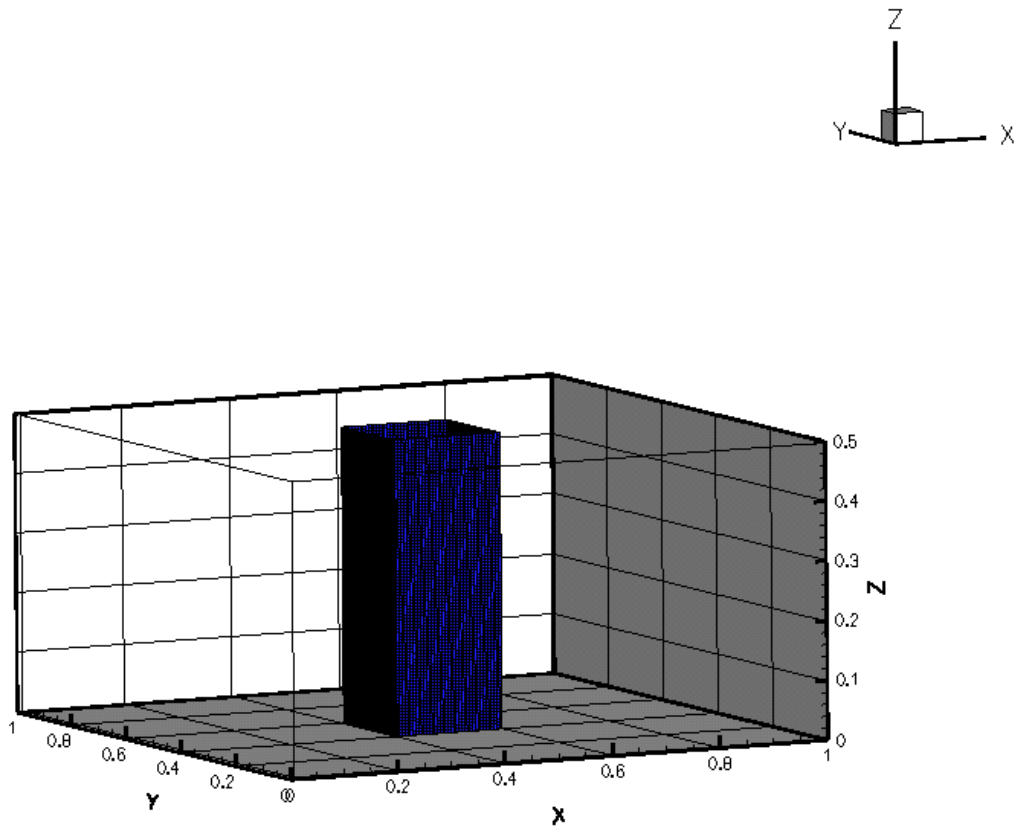


Figure 3-26. The three-dimensional geometry of the Mach 2 flow over a pillar.

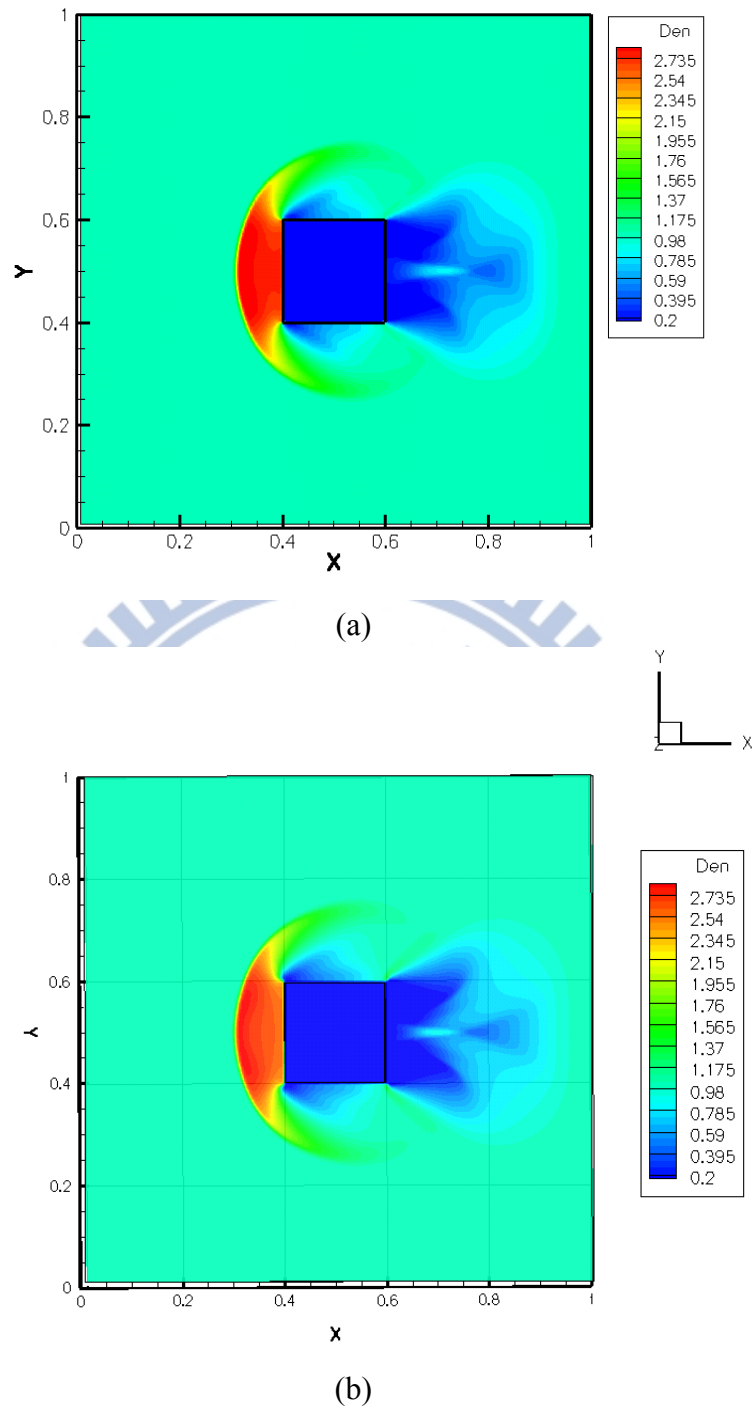


Figure 3-27. The Density contour of the Mach 2 flow over a pillar obtained using the second-order QDS- N^2 method (a) in two-dimension with 200×200 cells; (b) in three-dimension with $200 \times 200 \times 100$ cells. The CFL factor is 0.5 using MINMOD limiter.

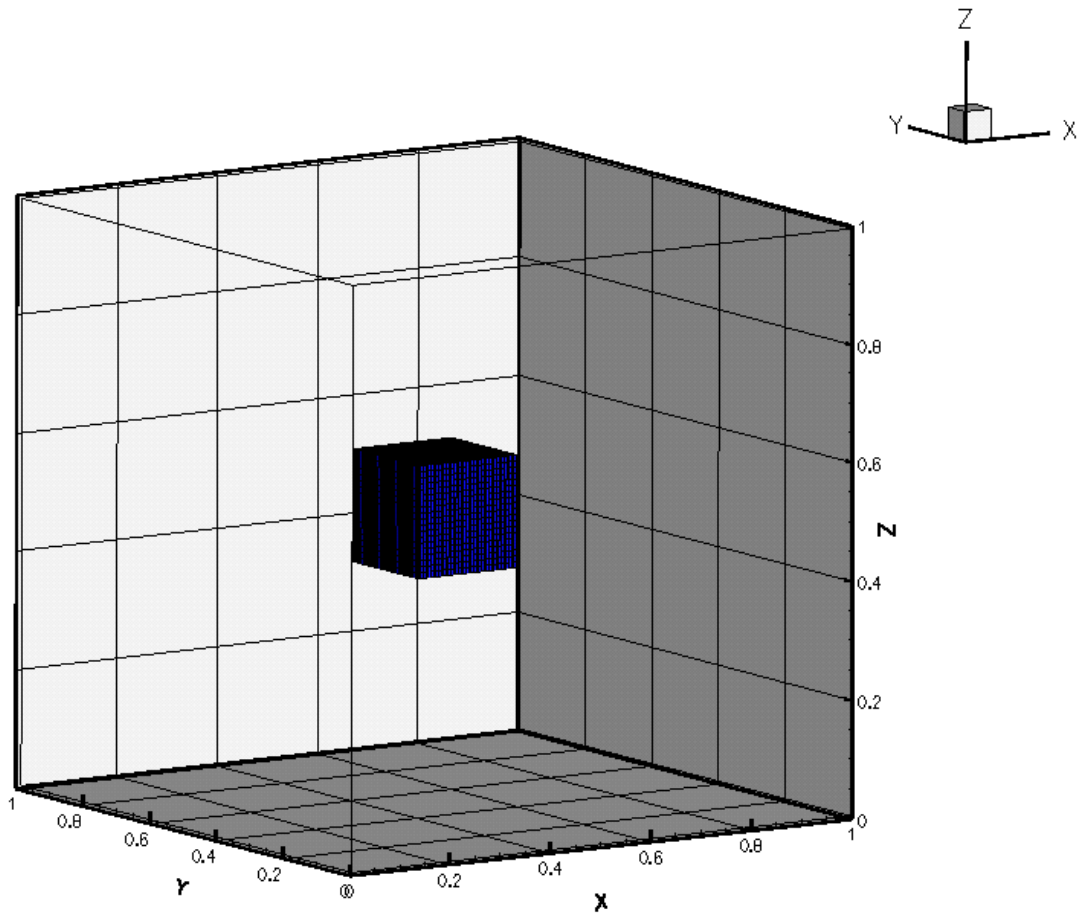
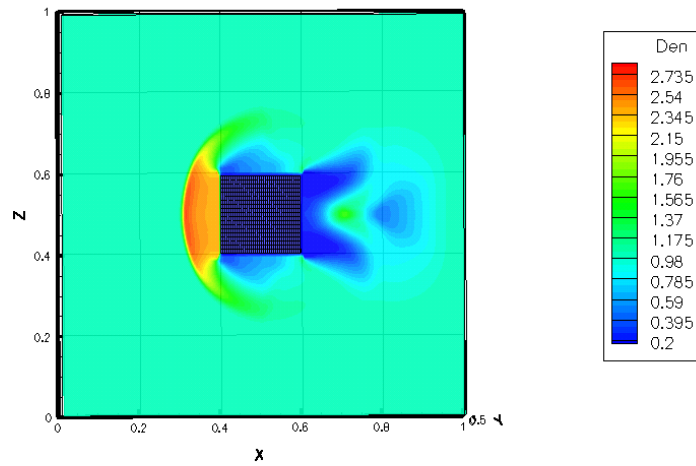
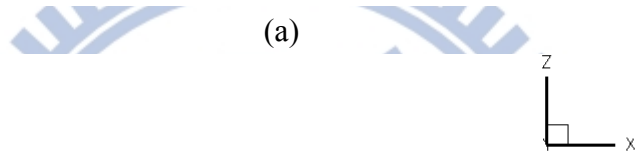
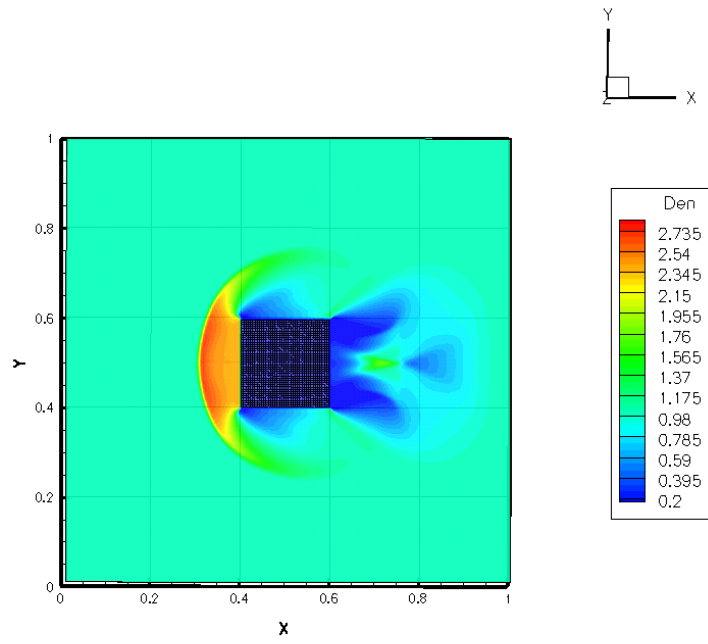


Figure 3-28. The three-dimensional geometry of the Mach 2 flow over a square block.



(b)

Figure 3-29. The Density contour of the Mach 2 flow over a square block obtained using the second-order QDS- N^2 method with $200 \times 200 \times 100$ cells (a) in x-y surface; (b) in x-z surface. The CFL factor is 0.5 using MINMOD limiter.

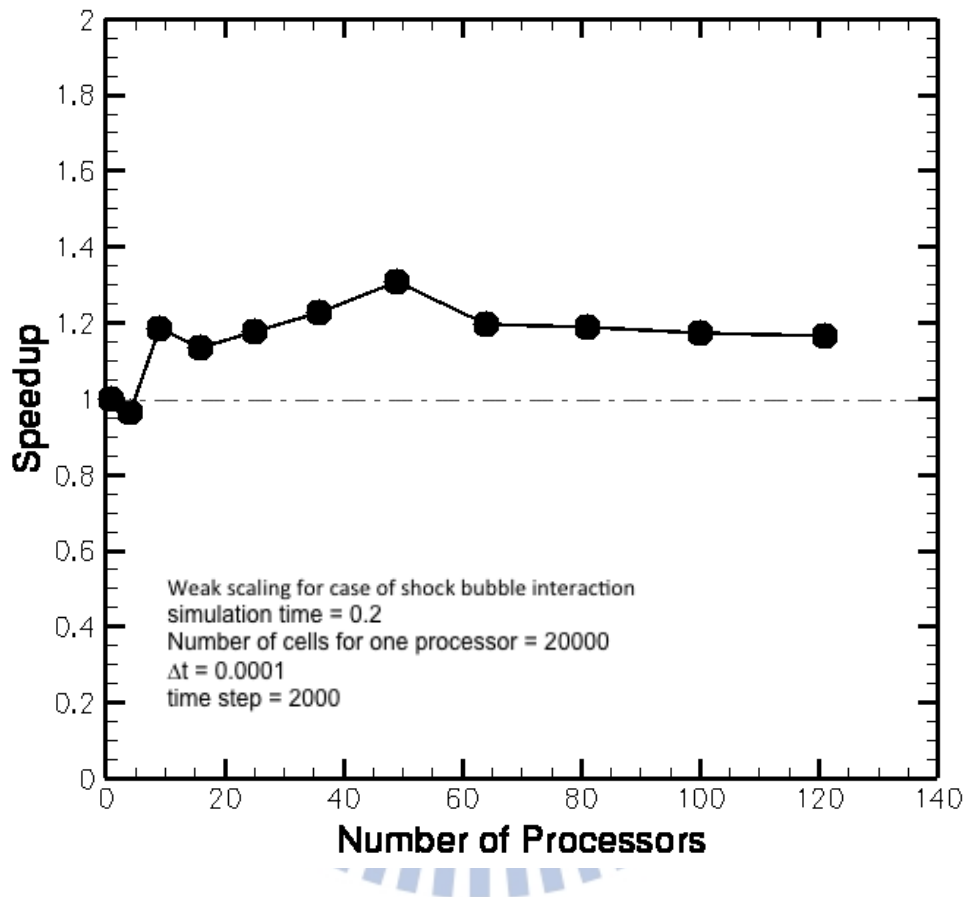


Figure 3-30. Parallel Performance of a 2D shock-bubble interaction with 2.4 million computational Cells.

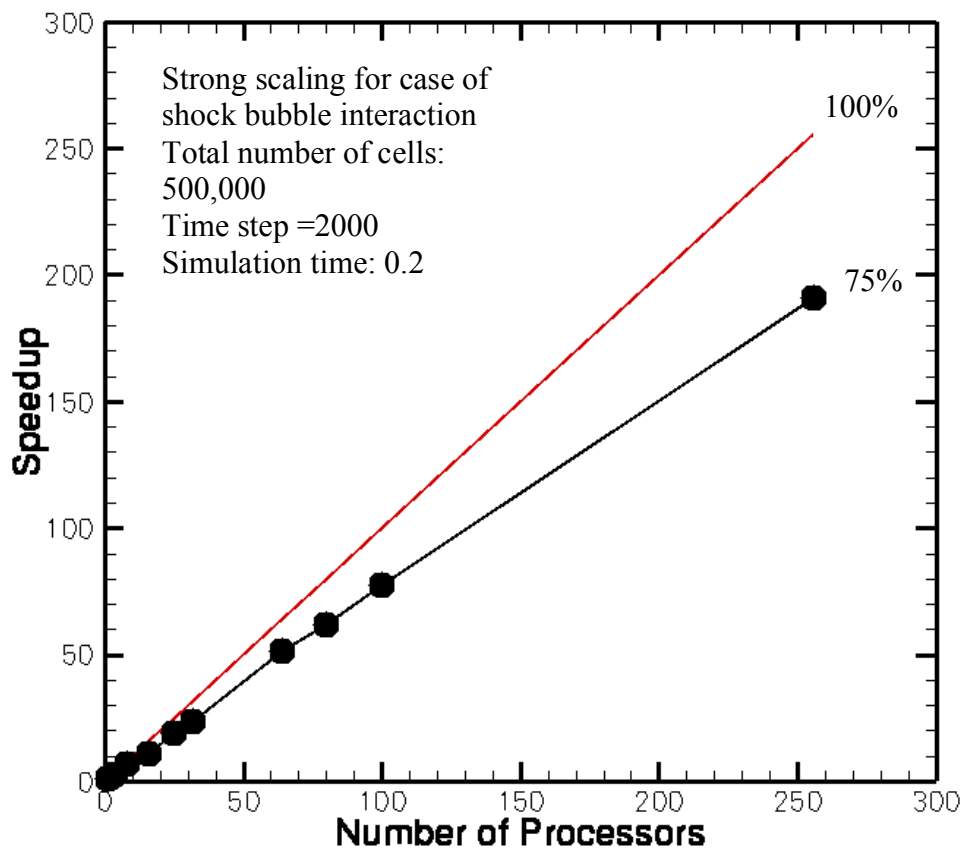


Figure 3-31. Strong scaling performance in the QDS- N^2 method with 500,000 cells on various massively parallel systems.

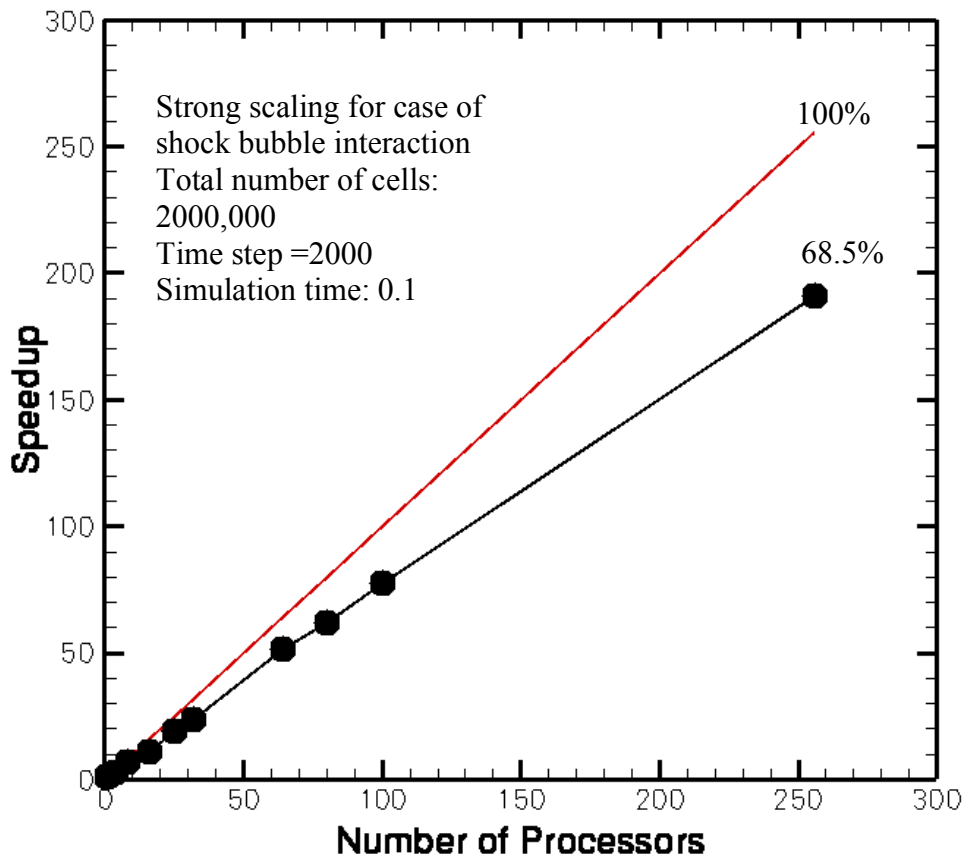


Figure 3-32. Strong scaling performance in the QDS- N^2 method with 2 million cells on various massively parallel systems.

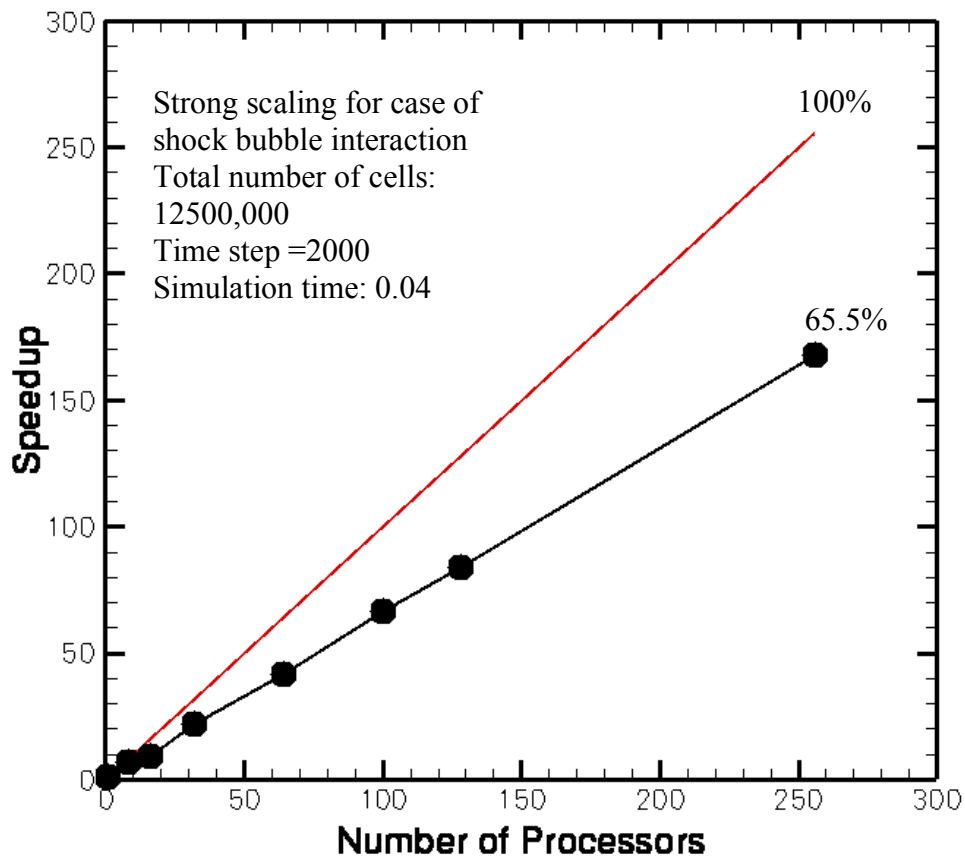


Figure 3-33. Strong scaling performance in the QDS- N^2 method with 12.5 million cells on various massively parallel systems.

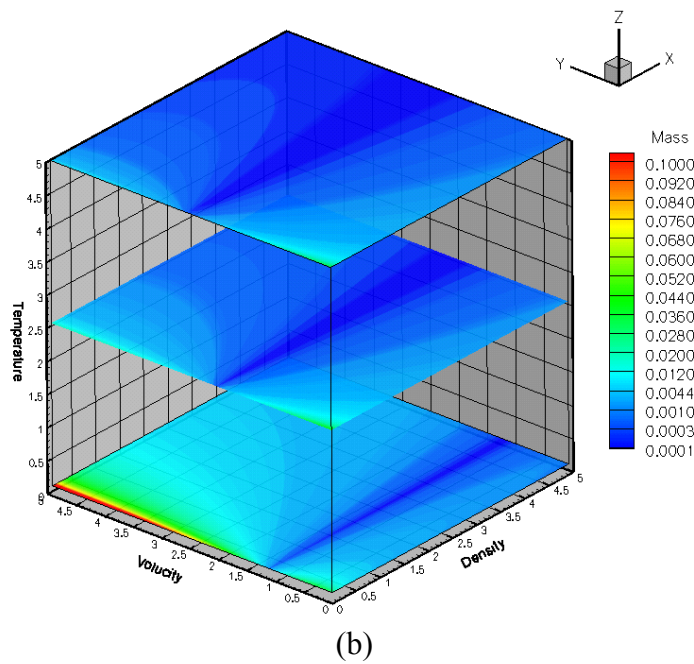
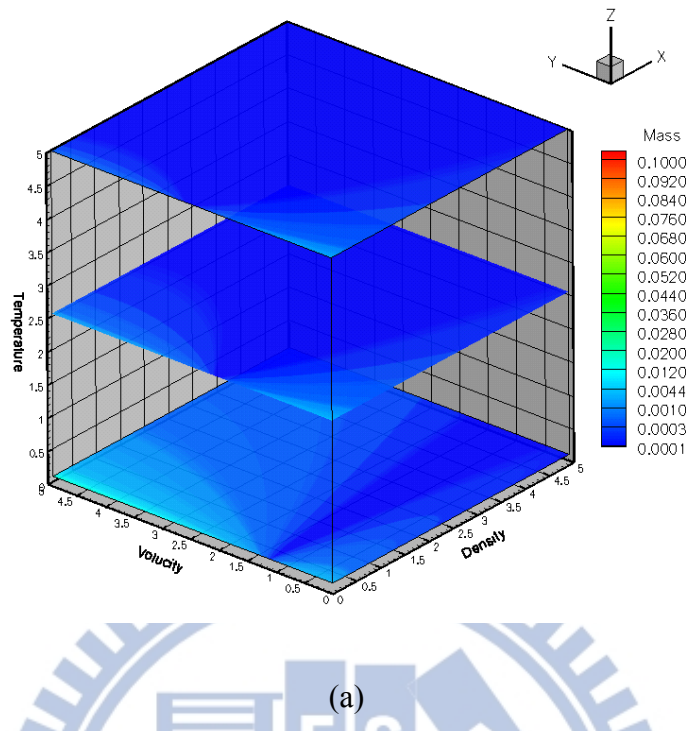
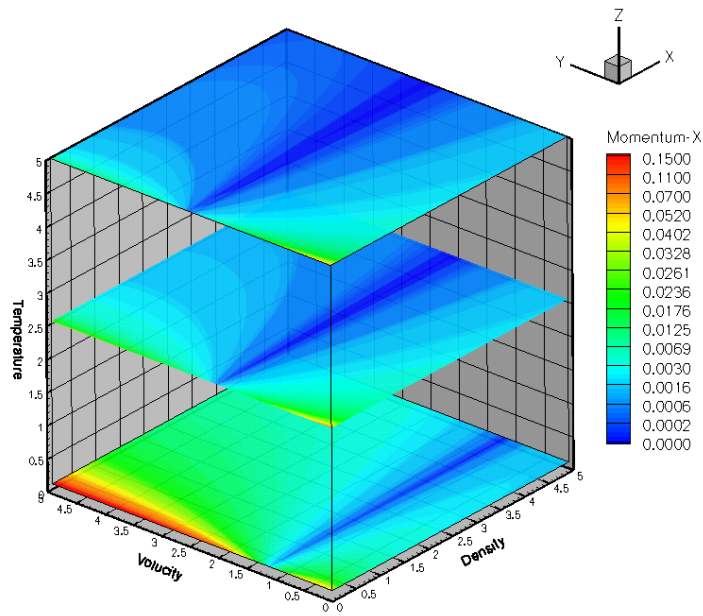
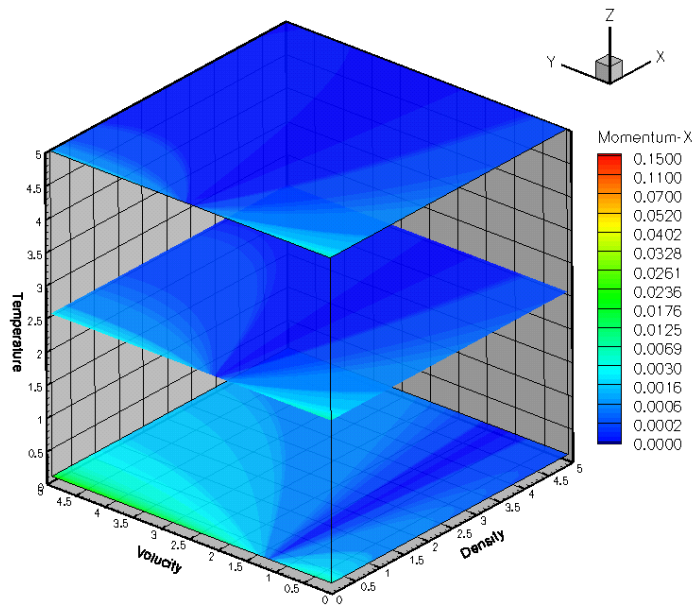


Figure 4-1 The value of mass flux for the difference of 2N and N² method. (a) The case

1 with the gradient $1.0e^{-5}$; (b) case 2 with the gradient $1.0e^{-6}$.

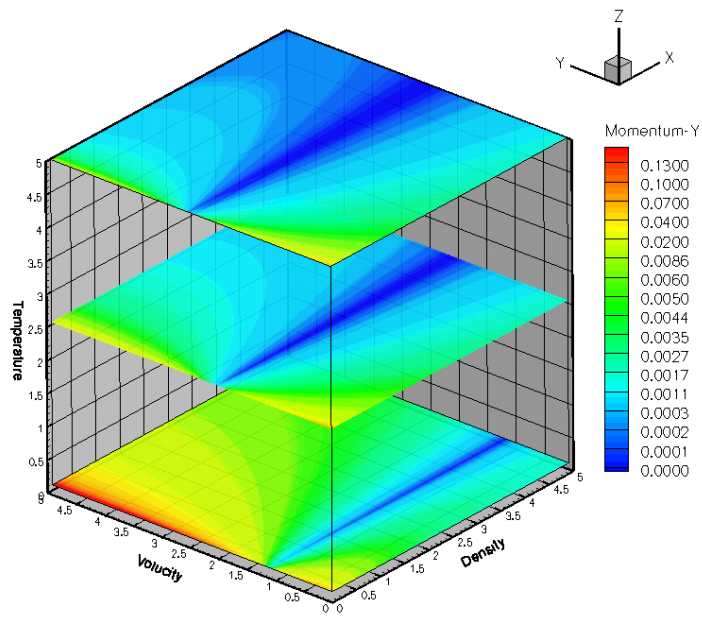


(a)

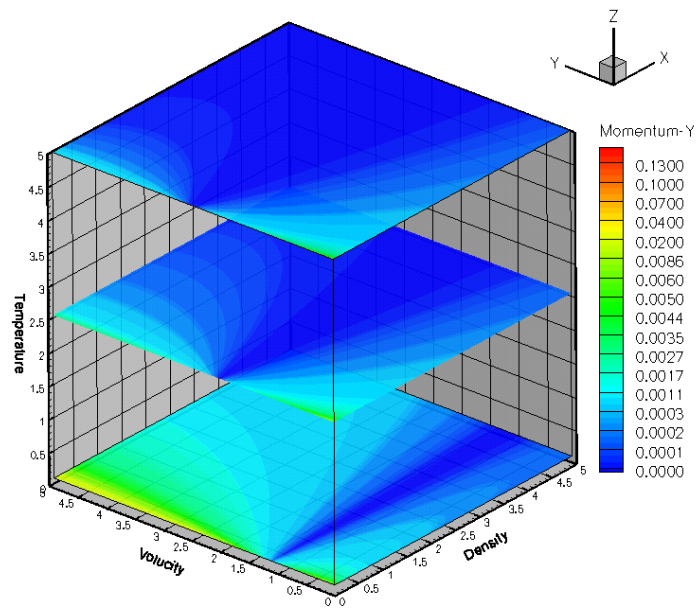


(b)

Figure 4-2. The value of momentum flux in x-direction for the difference of $2N$ and N^2 method. (a) The case 1 with the gradient $1.0e^{-5}$; (b) case 2 with the gradient $1.0e^{-6}$.

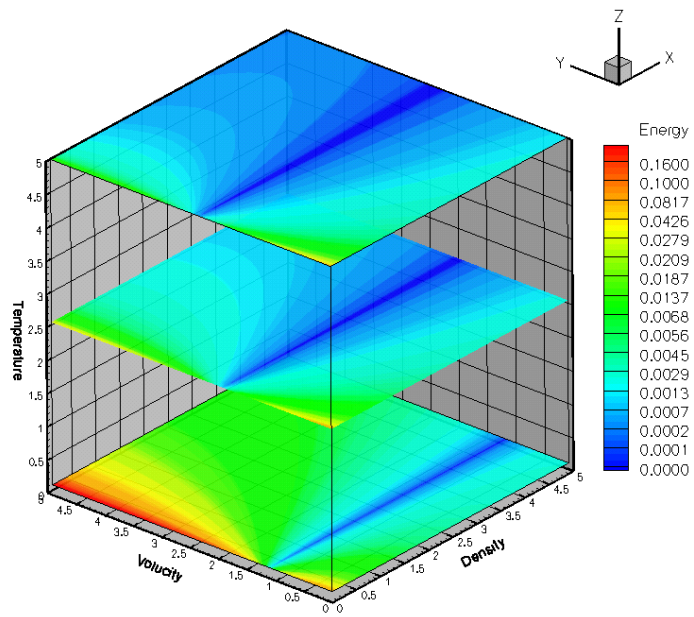


(a)

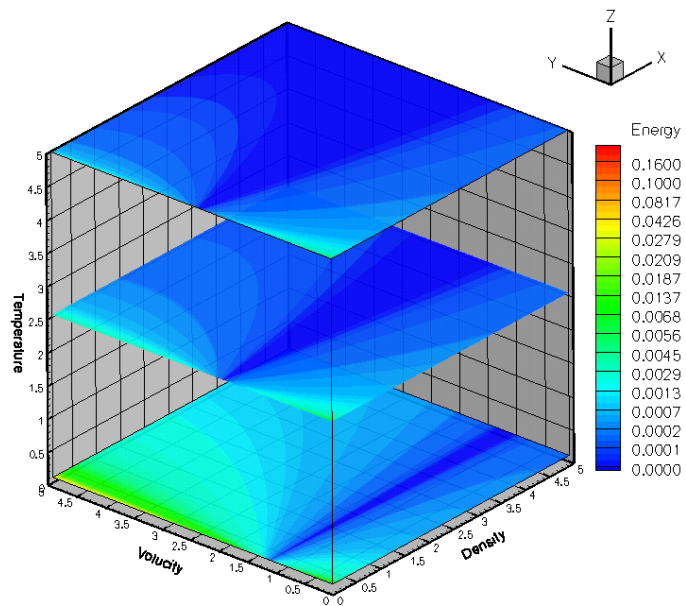


(b)

Figure 4-3. The value of momentum flux in y-direction for the difference of $2N$ and N^2 method. (a) The case 1 with the gradient $1.0e^{-5}$; (b) case 2 with the gradient $1.0e^{-6}$.

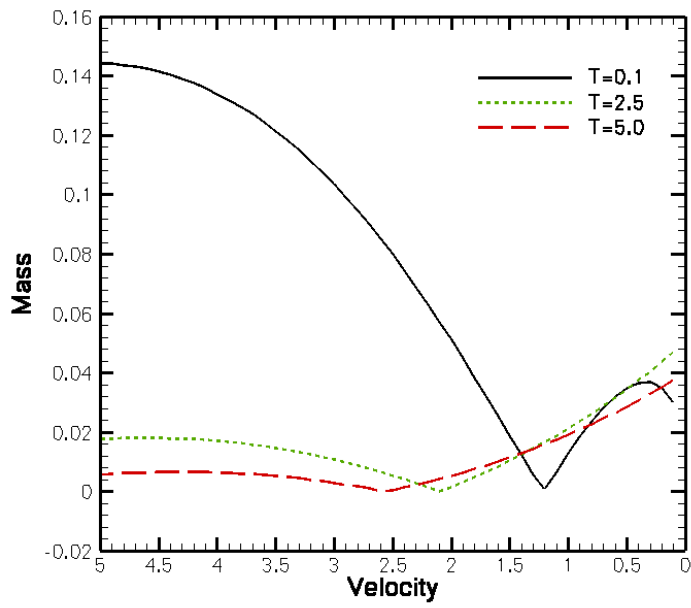


(a)

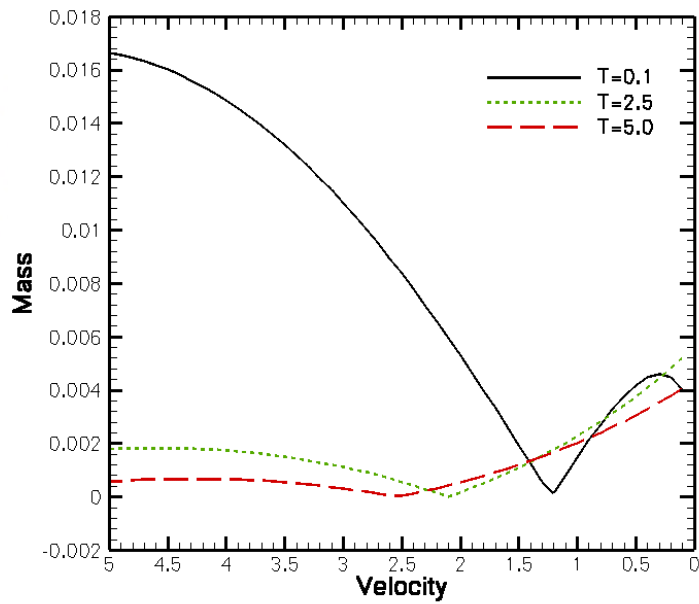


(b)

Figure 4-4. The value of energy flux for the difference of $2N$ and N^2 method. (a) The case 1 with the gradient $1.0e^{-5}$; (b) case 2 with the gradient $1.0e^{-6}$.



(a)



(b)

Figure 4-5. The value of energy flux for the difference of 2N and N² method at the low density range. (a) The case 1 with the gradient $1.0e^{-5}$; (b) case 2 with the gradient $1.0e^{-6}$.

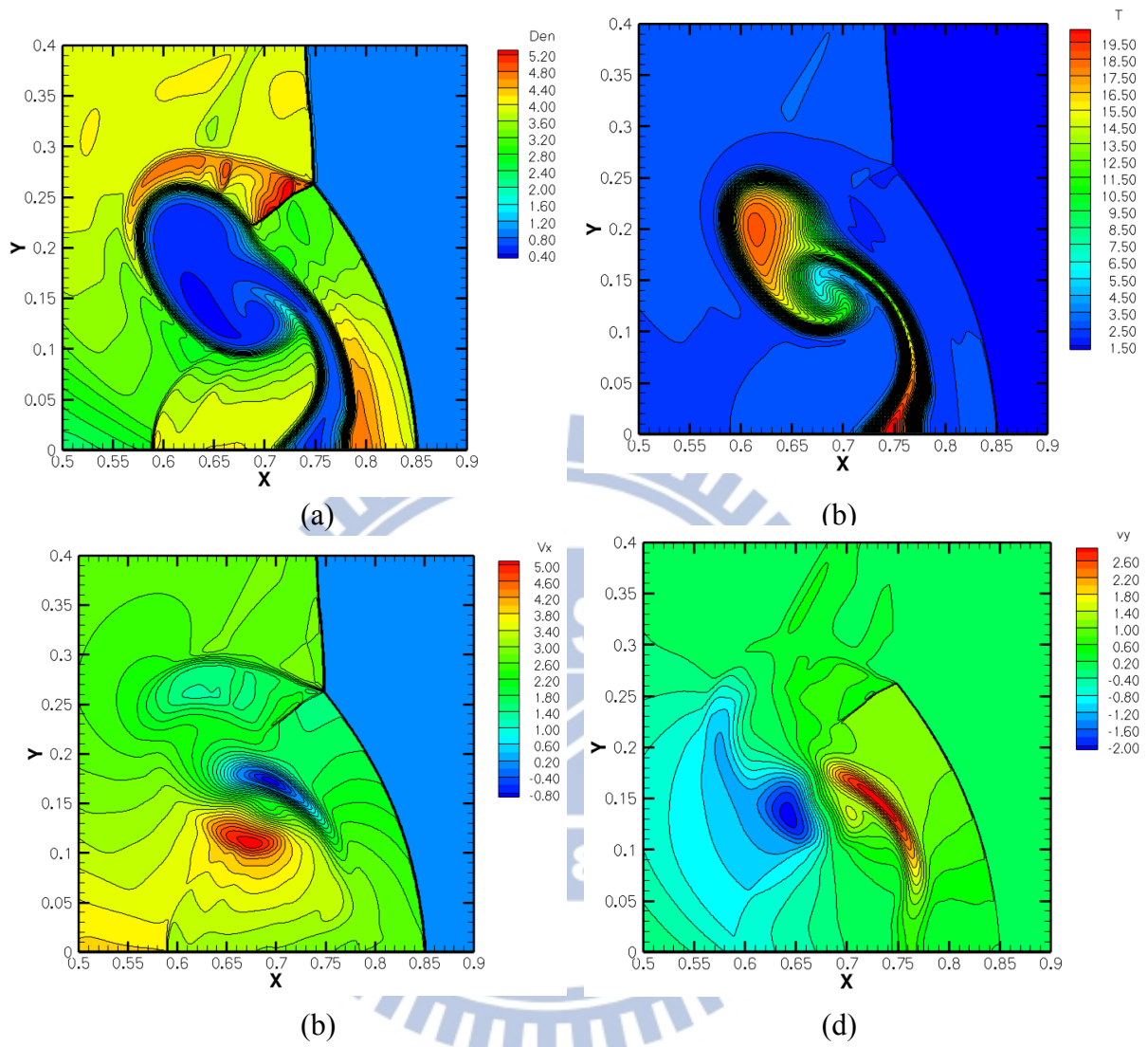
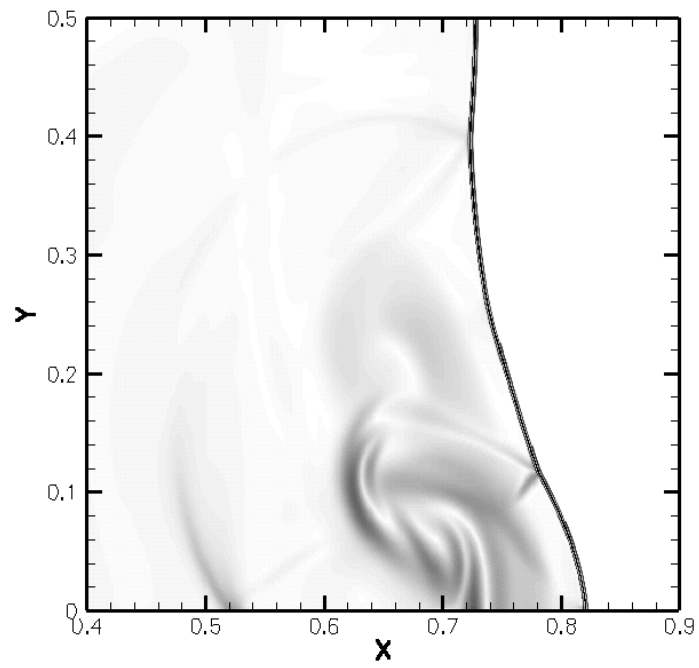
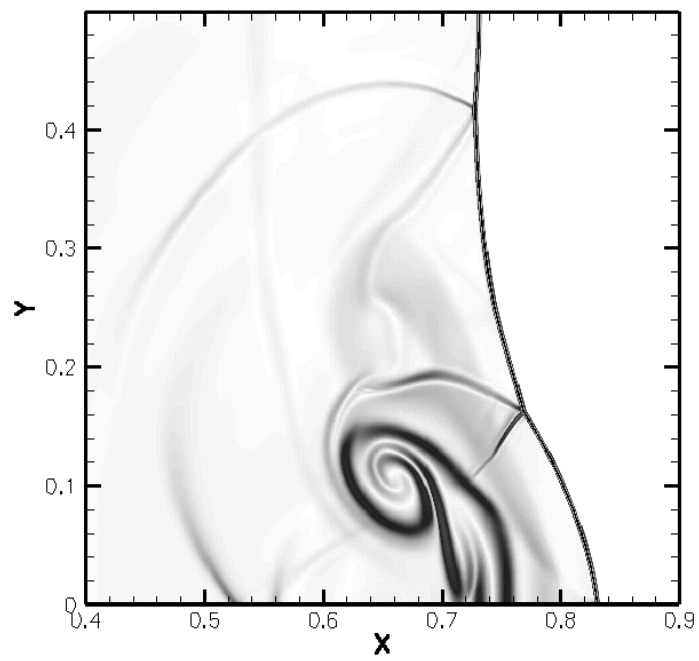


Figure 4-6. Contour profile of Shock-bubble interaction. QDS-N² 2nd order method using 1700×500 cells with MC limiter at time of 0.2. (a) Density, (b) temperature, (c) velocity in x-direction and (d) velocity in y-direction.

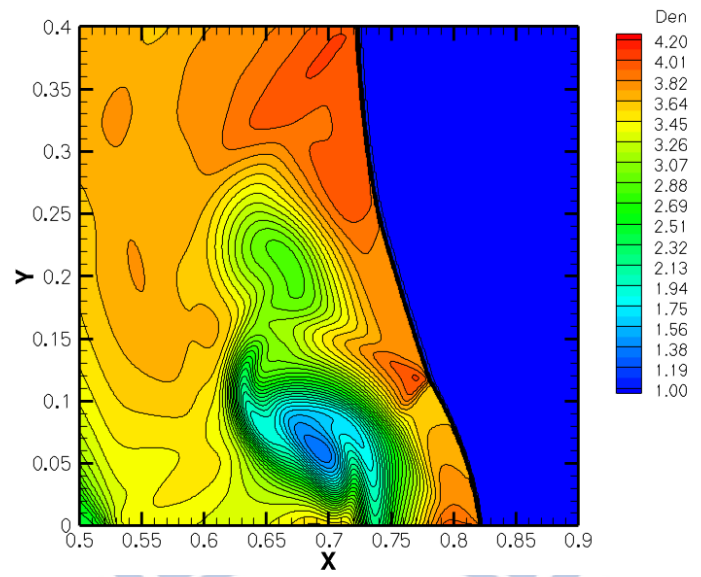


(a)

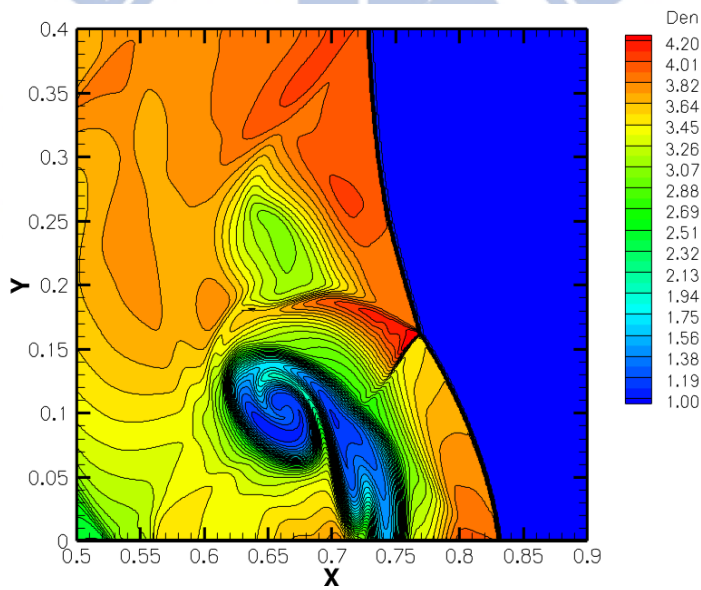


(b)

Figure 4-7 Shock-bubble Schlieren image with 1700×500 cells at time of 0.2. QDS 2nd order (a) 2N scheme with van Leer's limiter, (b) N^2 scheme.



(a)



(b)

Figure 4-8. The density contour obtained using (a) the 2N method; (b) the N^2 method with MC limiter, CFL=0.5, 1700×500 cells.

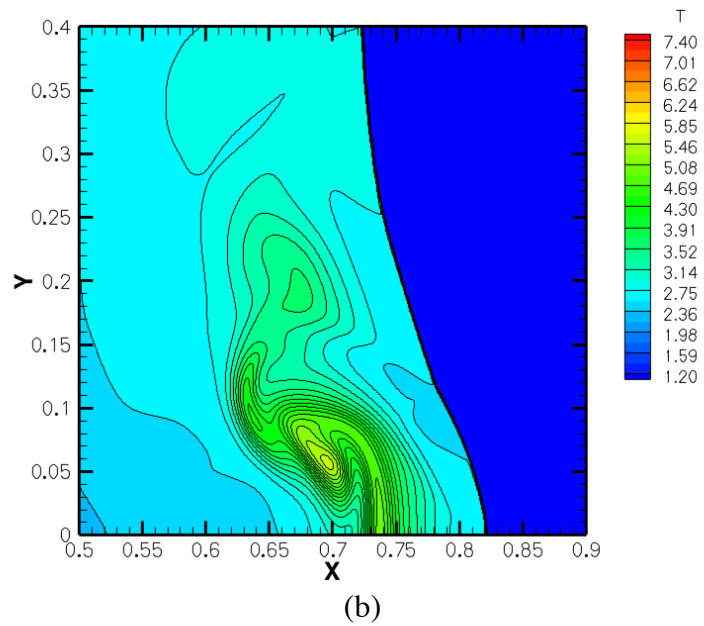
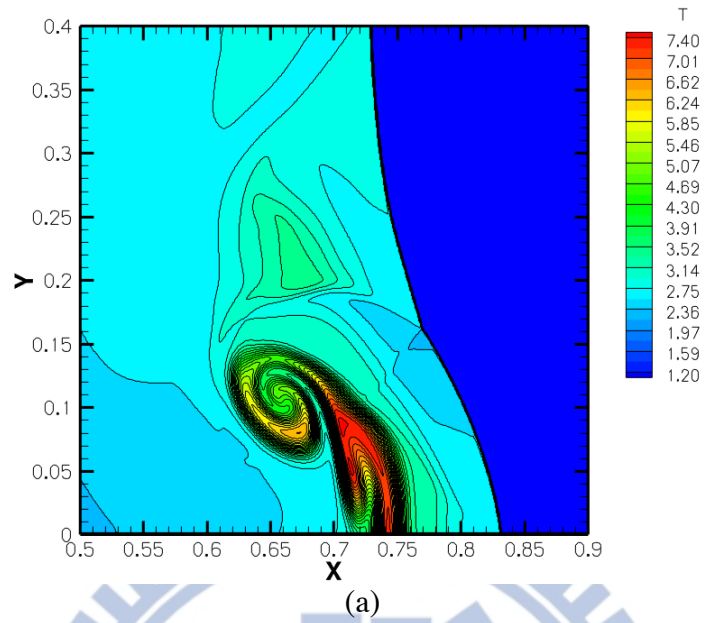


Figure 4-9. The temperature contour obtained using (a) the 2N method; (b) the N^2 method with MC limiter, CFL=0.5, 1700×500 cells.

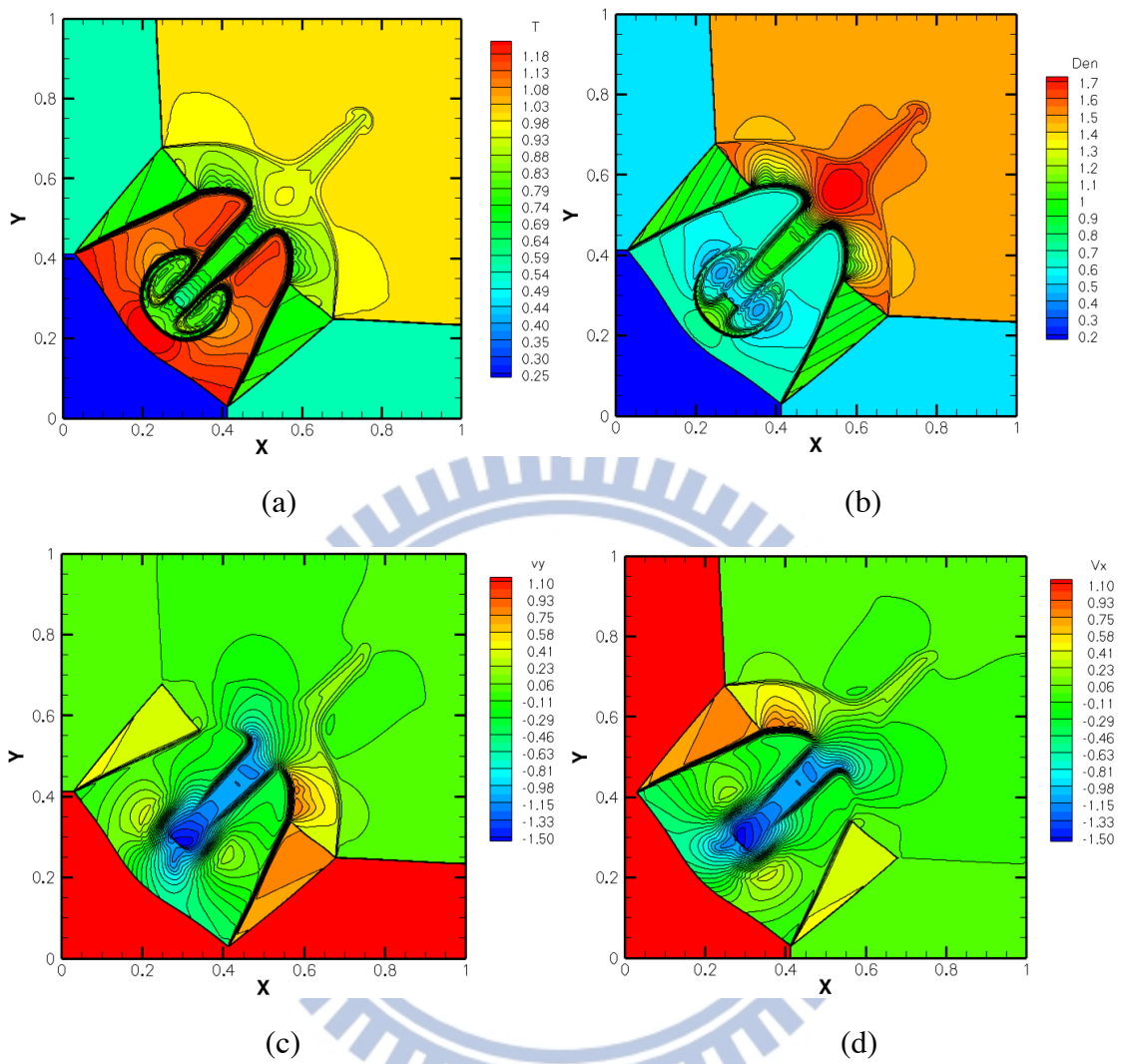


Figure 4-10. contour profile of N^2 method. (a)Density, (b) temperature, (c) velocity in x-direction and (d) velocity in y-direction.

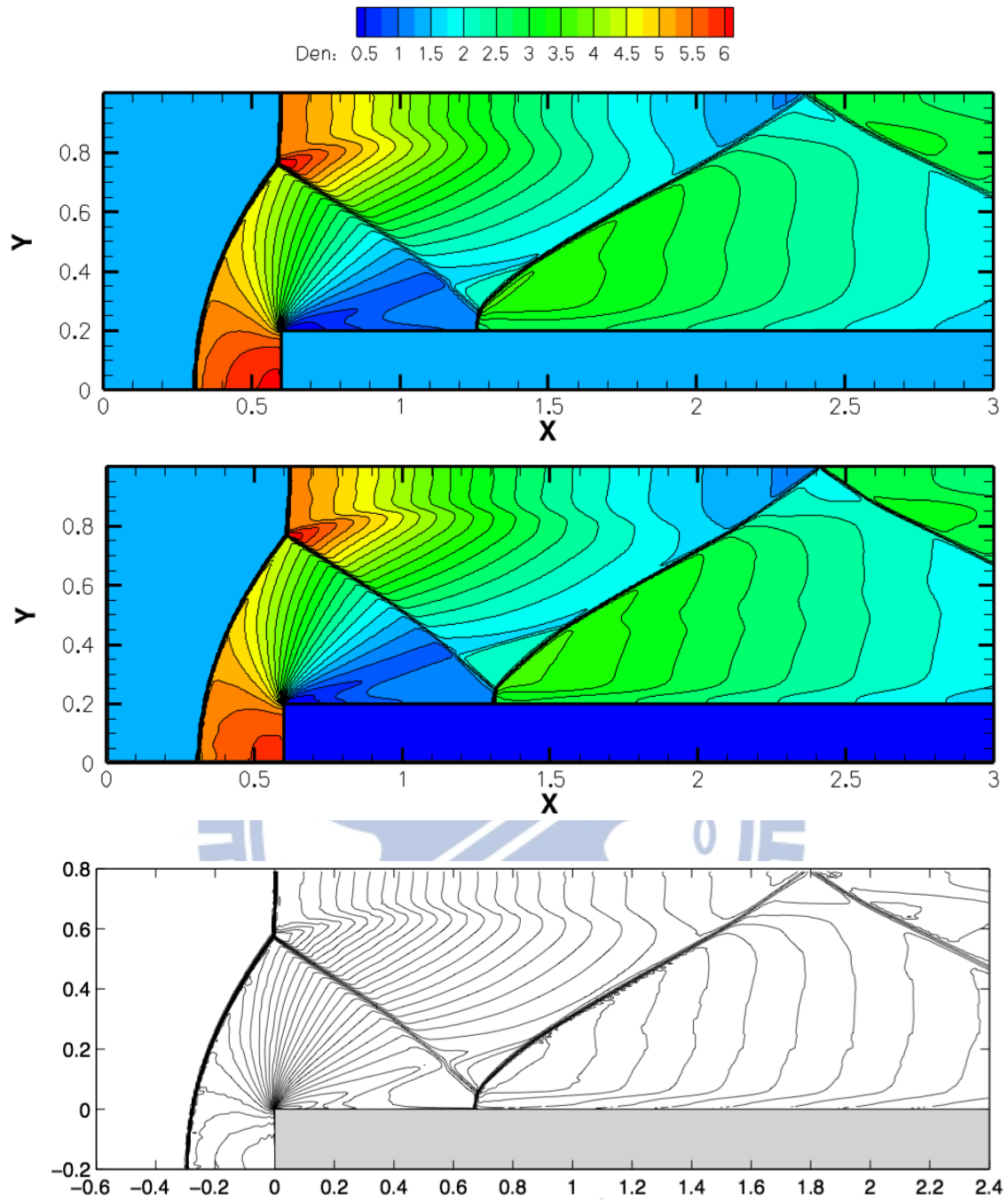


Figure 4-11. Contour of density at 4.0s for Mach 3 flow over a foeward facing step in a wind tunnel. Compare the 2nd order QDS-2N method (top) and QDS-N² method (middle) for 600×200 grids. (bottom) The result of Keats and Lien [Keats *et al.*, 2004]

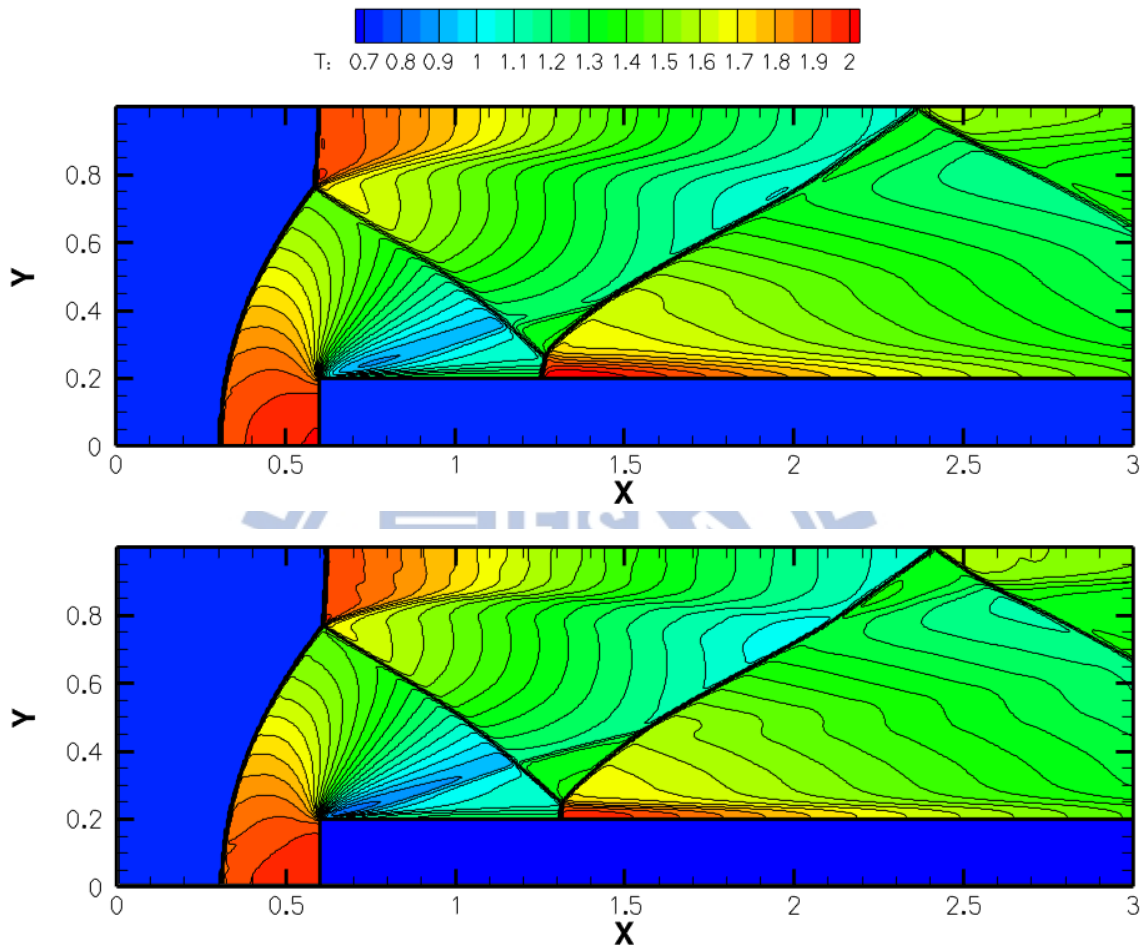


Figure 4-12. Contour of temperature obtained using second-order QDS-2N (top) and QDS-N² method using 4 simulation particles for Mach 3 flow over a forward facing step in a wind tunnel.

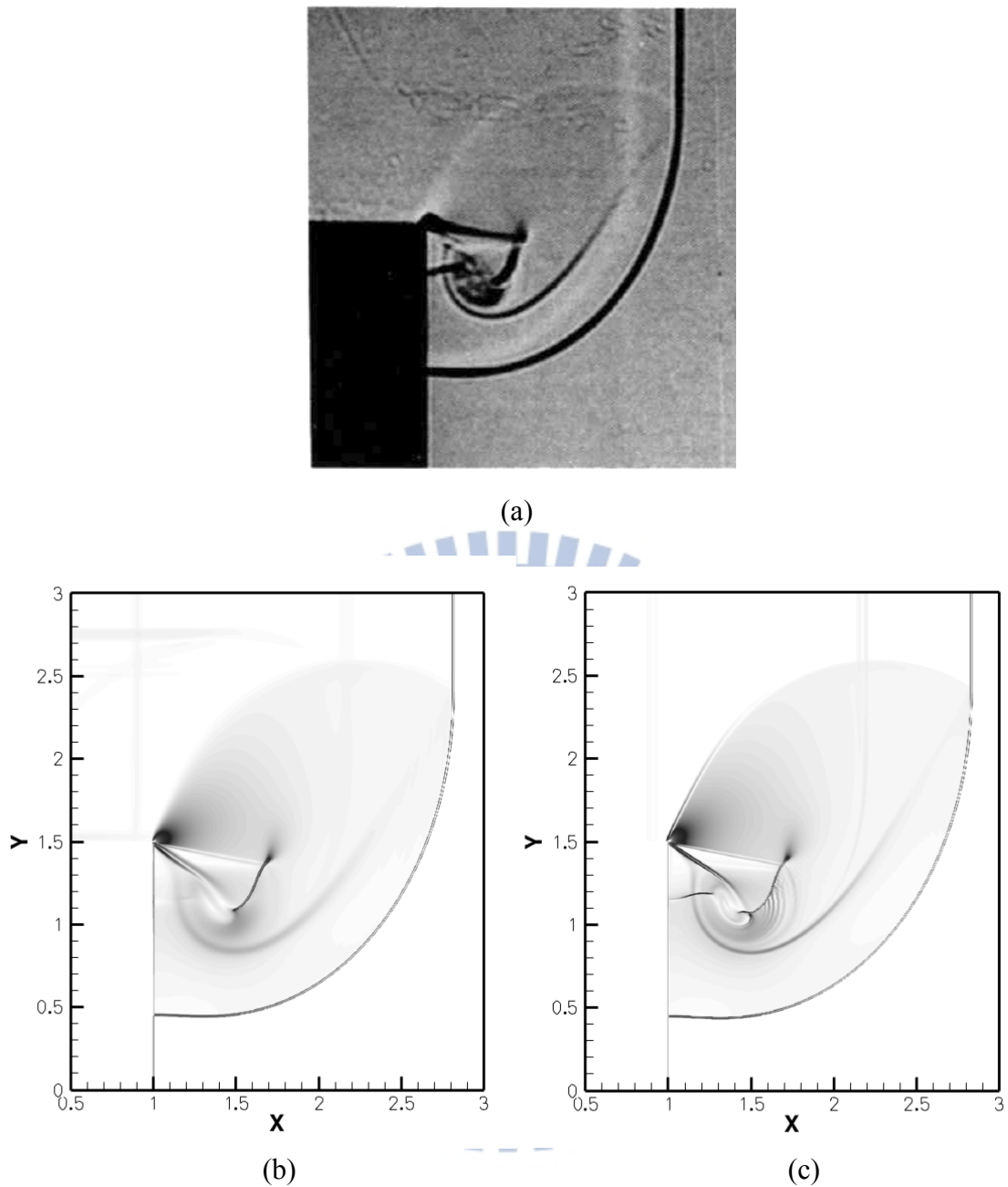


Figure 4-13. Schlieren image of the shock wave diffracting over a 90 degree sharp corner, $M_s=2.4$. (a) The experimental result made form Ritzerfeld *et al.* [Dyke, 1997]. (b) the second-order QDS-2N method, and (c) QDS-N2 method with 1000×1000 cells, MC limiter, CFL=0.2.

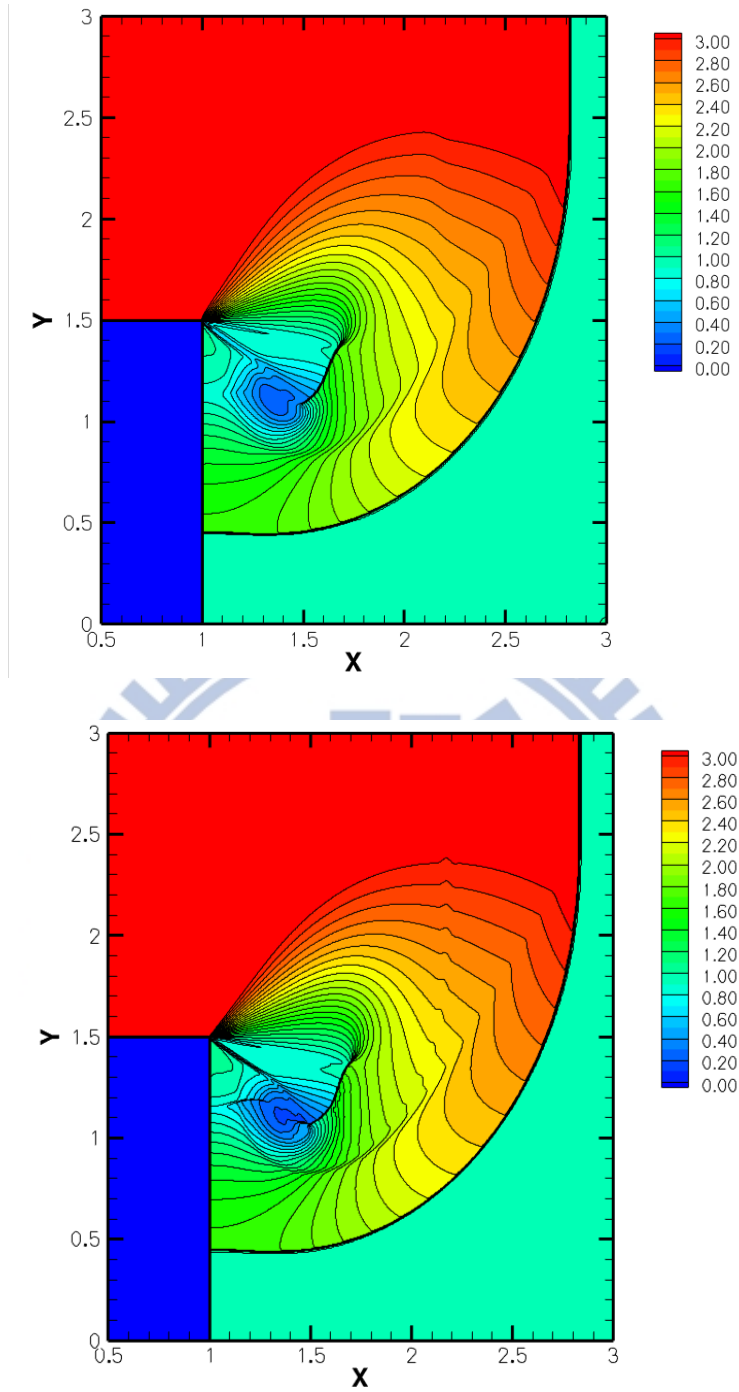


Figure 4-14. Density contours of Mach 2.4 shock diffraction using the second-order 2N method (top) and the N^2 method with 1000×1000 uniform grids. The CFL number uses 0.2 with MC limiter.

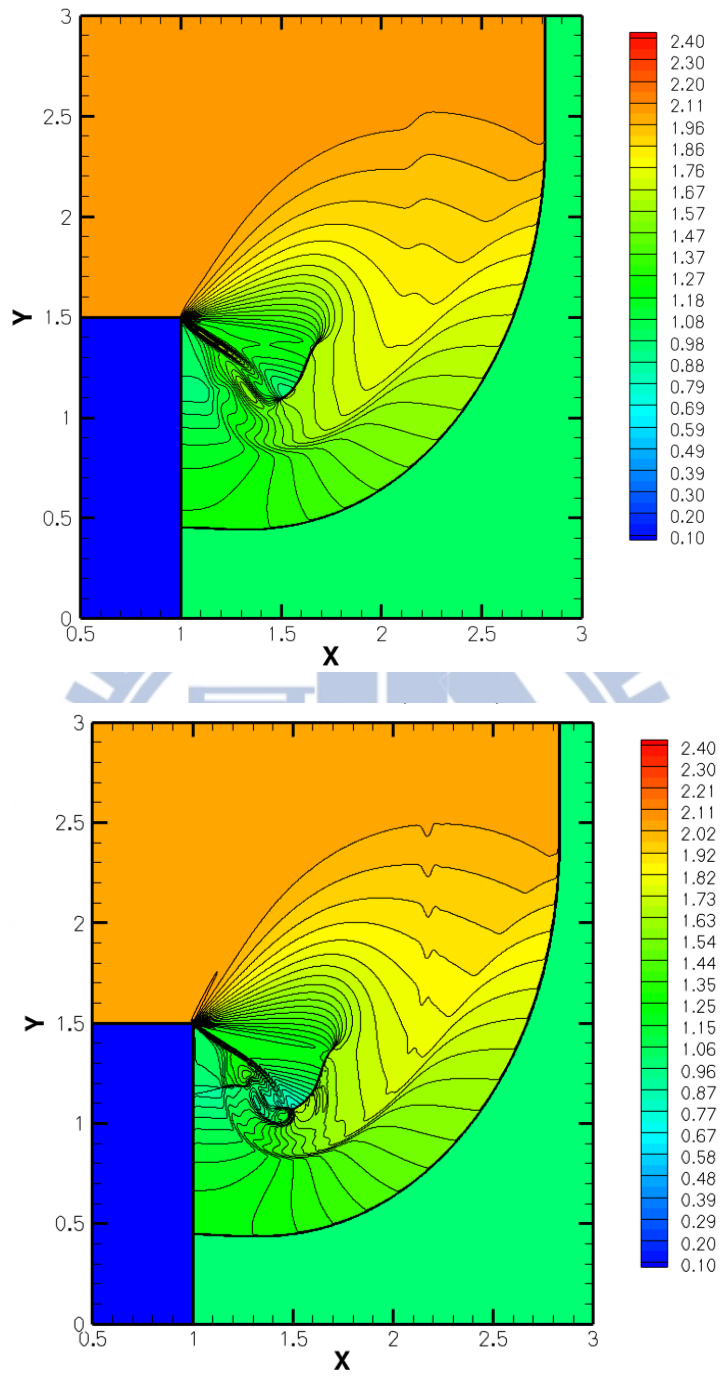


Figure 4-15. Temperature contours of Mach 2.4 shock diffraction using the second-order 2N method (top) and the N^2 method with 1000×1000 uniform grids. The CFL number uses 0.2 with MC limiter.

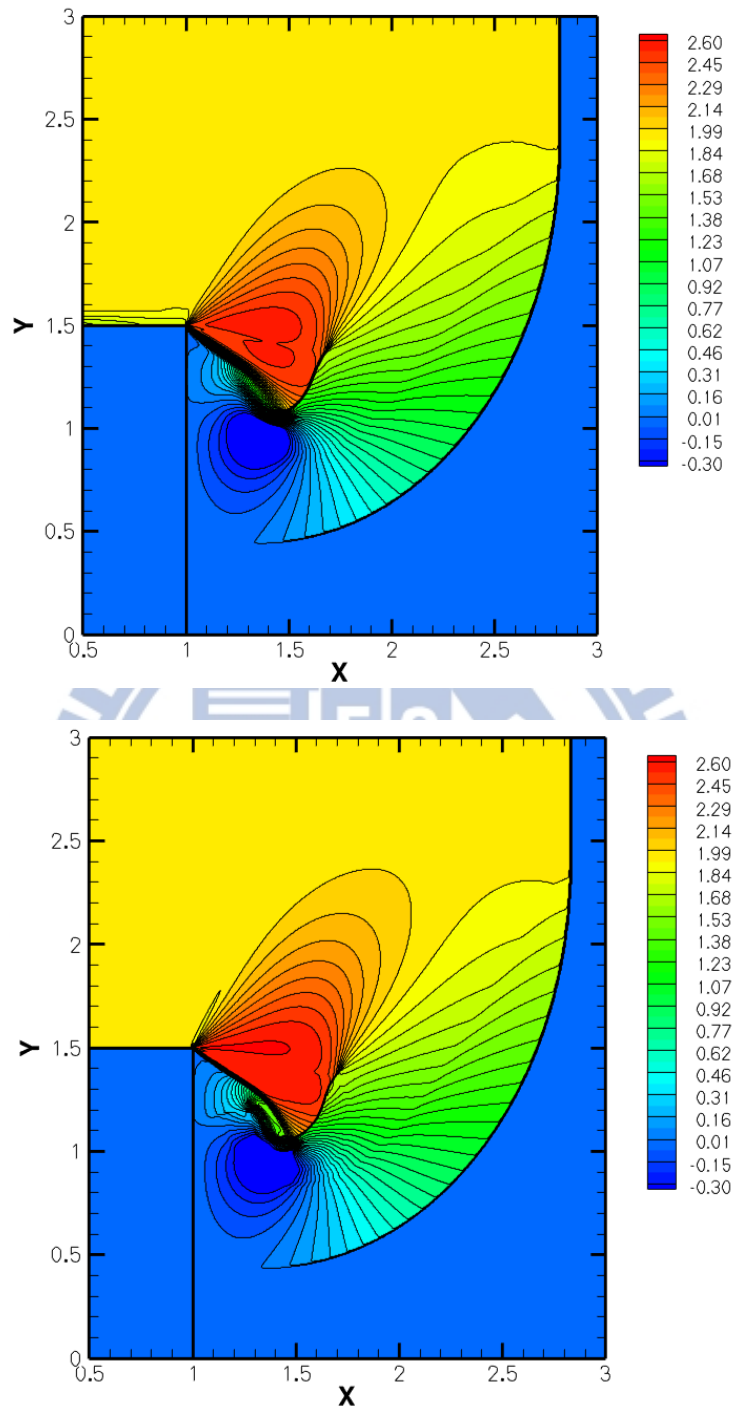


Figure 4-16. Velocity contours of Mach 2.4 shock diffraction using the second-order 2N method (top) and the N^2 method with 1000×1000 uniform grids in x-direction. The CFL number uses 0.2 with MC limiter.

List of Publications

Journals: (* corresponding author)

1. **Y.-J. Lin**, M. R. Smith, F.-A. Kuo, H. M. Cave, M. C. Jermy and **J.-S. Wu***, “A True-direction Reconstruction to the Multi-dimensional Quiet Direct Simulation Method,” Computer Physics Communications, 2013 (in press).
<http://dx.doi.org/10.1016/j.cpc.2013.05.007>
2. **Y.-J. Lin**, M. R. Smith and **J.-S. Wu***, “Theoretical Analysis of Flux Deviation of Quiet Direct Simulation Method: $2N$ vs. N^2 ,” Computer Physics Communications, 2013 (**under preparation**).
3. **Y.-J. Lin**, M. R. Smith and **J.-S. Wu***, “Parallel Implementation of Quiet Direct Simulation Monte Carlo Method,” Computers and Fluids, 2013 (**under preparation**).

International Conference Papers: (* corresponding author)

1. **Y.-J. Lin**, M. Smith, Fang-An Kuo, H. Cave and **J.-S. Wu***, “Two-dimensional quiet direct simulation (QDS) using GPUs,” Conference on Computational Physics, Kaohsiung, Taiwan, December 15-19, 2009.
2. **Y.-J. Lin**, M. R. Smith, H. M. Cave, J.-C. Huang and **J.-S. Wu***, “General Higher Order Extension to the Quiet Direct Simulation Method,” The 27th International Symposium on Rarefied Gas Dynamics, California, July 10-15, 2010.
3. H.M. Cave, C.-W. Lim, M.C. Jermy, S.P. Krumdieck, M.R. Smith, **Y.-J. Lin** and **J.-S. Wu***, “Multi-Species Fluxes for the Parallel Quiet Direct Simulation (QDS) Method,” The 27th International Symposium on Rarefied Gas Dynamics,

California, July 10-15, 2010.

4. H.M. Cave, M.R. Smith, **Y.-J. Lin**, F.-A. Kuo, **J.-S. Wu***, M.C. Jermy, and C.-W. Lim, “Overview of the Kinetic-based Quiet Direct Simulation (QDS) Method for Gas Flow Computation,” The 8th Asian Computational Fluid Dynamics Conference, Hong Kong, 10-14 January 2010.
5. H.M. Cave, M. R. Smith, **J.-S. Wu***, M. C. J ermy, **Y.-J. Lin**, C.- W. Lim , S.P. K rumdieck, “Multispecies Fluxes for the Parallel Quiet Direct (QDS) Method,” The 22nd International Conference on Parallel Computational Fluid Dynamics, Kaohsiung, Taiwan, May 17-21, 2010.
6. **Ya-Ju Lin**, M. R. Smith, and **J.-S. Wu***, “A True-Direction Flux Reconstruction Scheme to Quiet Direct Simulation Method for Inviscid Gas Flows” 9th International Conference on Fluid Dynamics, Sendia, Japan, September 19-21, 2012.
7. **Ya-Ju Lin**, M. R. Smith, and **J.-S. Wu***, “A True-Direction Quiet Direct Simulation Method for Inviscid Gas Flows” 9th International Conference for Mesoscopic Methods in Engineering and Science, Taipei, Taiwan, July 23-27, 2012.
8. **Ya-Ju Lin**, M. R. Smith, and **J.-S. Wu***, “A True-direction Reconstruction of the Quiet Direct Simulation Method for Inviscid Gas Flows” 51st Aerospace Sciences Meeting Conference, Dallas, TX, USA, January 5-9, 2012.

Domestic Conference Papers: (* corresponding author)

1. Hadley M. Cave, Chin-Wai Lim, **Y.-J. Lin**, Mark C. Jermy, Susan P. Krumdieck and **J.-S. Wu***, “Inviscid Flow Modeling using the Quiet Direct Simulation (QDS) Method,” The 16th National Computational Fluid Dynamics,

- YiLan, July 30-August 1, 2009.
2. **Y.-J. Lin**, M.R. Smith, M. Jermy, J.-C. Huang and **J.-S. Wu***, “Higher-order Extension of Quiet Direction Simulation (QDS) Method for Inviscid Flow Computation,” The 17th National Computational Fluid Dynamics, Chungli, Taiwan, July 29-July 31, 2010.
 3. **Y.-J. Lin**, M. R. Smith, H. M. Cave, **J.-S. Wu*** and M. C. Jermy, “A True-direction Reconstruction to the Multi-dimensional Quiet Direct Simulation Method,” 18th Computational Fluid Dynamics Conference in Taiwan, Yilan, Taiwan, August 3-5, 2011.
 4. **Y.-J. Lin**, M. R. Smith and **J.-S. Wu***, “A True-Direction Flux Reconstruction Scheme to the Second-Order Quiet Direct Simulation Method for Inviscid Gas Flows”19th Computational Fluid Dynamics Conference, Penghu, Taiwan, August 16-18, 2012.
 5. **Y.-J. Lin**, M.R. Smith and **J.-S. Wu***, “Quiet Direct Simulation Method for Euler Equation using True-direction Reconstruction Flux,” 20th Computational Fluid Dynamics Conference, Nantou, Taiwan, August 21-23, 2013 (summitted).